

**Lehrstuhl für Statik
der Technischen Universität München**

Optimal Shape Design of Shell Structures

Matthias Firl

Vollständiger Abdruck der von der Fakultät für Bauingenieur- und Vermessungswesen der Technischen Universität München zur Erlangung des akademischen Grades eines

Doktor-Ingenieurs

genehmigten Dissertation.

Vorsitzender:

Univ.-Prof. Dr.-Ing. habil. Gerhard H. Müller

Prüfer der Dissertation:

1. Univ.-Prof. Dr.-Ing. Kai-Uwe Bletzinger

2. Prof. Erik Lund Ph.D., Aalborg University, Dänemark

Die Dissertation wurde am 28.06.2010 bei der Technischen Universität München eingereicht und durch die Fakultät für Bauingenieur- und Vermessungswesen am 16.11.2010 angenommen.

Schriftenreihe des Lehrstuhls für Statik
der Technischen Universität München

Band 15

Matthias Firl

Optimal Shape Design of Shell Structures

Optimal Shape Design of Shell Structures

Abstract

Numerical shape optimization is a general and highly efficient tool to improve mechanical properties of structural designs. Especially shell structures seriously profit by geometries which allow for load carrying by membrane action instead of bending. The most important modeling step of shape optimization problems is the correct shape parametrization. It is well known that classical parametrization techniques like CAGD and Morphing require time consuming remodeling steps. This thesis shows that FE-based parametrization is well suited to define large and flexible design spaces with a minimal modeling effort. The resulting optimization problems are characterized by a large number of design variables which requires a solution by gradient based optimization strategies. Adjoint sensitivity formulations are applied to reduce the numerical effort of sensitivity analysis. Derivatives of FE-quantities like stiffness matrices or load vectors are computed by semi-analytic derivatives supplemented by correction factors based on dyadic product spaces of rigid body rotation vectors. Besides the efficient sensitivity analysis the large number of design variables also require regularization methods to control curvature of the optimal geometry and mesh quality. The maximum curvature is determined by filter methods based on convolution integrals whereas the mesh quality is improved by geometrical and mechanical mesh optimization methods. Simulation and shape optimization of thin and long span shell structures require consideration of nonlinear kinematics. It is shown by theoretical investigations and illustrative examples that geometrically nonlinear shape optimization yields to much more efficient designs than the classical linear approaches. The presented optimization strategy combines nonlinear path following methods with the design changes during the optimization procedure. This extended approach permits efficient solution of geometrically nonlinear structural optimization problems. Several real life examples from civil engineering and automotive industry prove efficiency and accuracy of the presented shape optimization strategy. They motivate frequent applications of shape optimization utilizing FE-based parametrization in order to improve efficiency, quality and environmental compatibility of current technical designs.

Optimale Formgebung von Schalenstrukturen

Zusammenfassung

Numerische Formoptimierung ist ein allgemeines und hocheffizientes Werkzeug, um mechanische Eigenschaften von Strukturentwürfen zu verbessern. Besonders Schalenstrukturen profitieren erheblich von Geometrien, welche einen Lastabtrag über Membrankräfte anstatt Biegemomenten ermöglichen. Der wichtigste Modellierungsschritt eines Formoptimierungsproblems ist die richtige Formparametrisierung. Es ist bekannt, dass hier klassische CAGD bzw. Morphingtechniken aufwändiger Remodellierungsschritte bedürfen. Diese Arbeit zeigt, dass die FE-Netz basierte Formparametrisierung sehr gut geeignet ist, um große und flexible Entwurfsräume mit einem minimalen Modellierungsaufwand zu definieren. Die daraus resultierenden Optimierungsprobleme weisen eine große Anzahl von Designvariablen auf, wodurch deren Lösung mit gradientenbasierten Optimierungsstrategien notwendig ist. Die adjungierte Sensitivitätsanalyse wird angewendet, um den numerischen Aufwand der Gradientenberechnung zu reduzieren. Die Ableitungen der FE-Parameter werden durch semi-analytische Formulierungen berechnet, die durch Korrekturfaktoren, basierend auf den dyadischen Produkträumen der Starrkörperrotationsvektoren, ergänzt werden. Neben einer effizienten Sensitivitätsanalyse verlangt die große Anzahl der Optimierungsvariablen auch Regularisierungstechniken, um die Krümmung und die Netzqualität der optimalen Lösung zu kontrollieren. Hierbei wird die maximale Krümmung über ein auf der Theorie der Faltungsintegrale beruhendes Filterverfahren bestimmt, während die Netzqualität durch geometrische bzw. mechanische Netzregularisierungsverfahren sichergestellt ist. Simulation und Formoptimierung von dünnen, weitgespannten Schalenstrukturen erfordert die Berücksichtigung nichtlinearer Kinematik. Durch theoretische Betrachtungen und entsprechende Beispiele wird gezeigt, dass die Berücksichtigung nichtlinearer Kinematik zu deutlich effizienteren Entwürfen führt. Die vorgestellte Optimierungsstrategie verbindet nichtlineare Pfadverfolgungsmethoden mit der Geometrieänderung während des Optimierungsprozesses. Dieser erweiterte Ansatz erlaubt eine effiziente Lösung geometrisch nichtlinearer Optimierungsprobleme. Einige Beispiele aus dem Bauingenieurwesen und dem Automobilbau zeigen das Potential und die Genauigkeit der vorgestellten Optimierungsstrategie. Sie motivieren eine häufige Anwendung der Formoptimierung mit FE-Netz basierter Parametrisierung um die Effizienz und die Umweltverträglichkeit der heutigen technischen Entwürfe zu verbessern.

Vorwort

Die vorliegende Arbeit entstand während meiner Arbeit als wissenschaftlicher Mitarbeiter am Lehrstuhl für Statik der Technischen Universität München.

Mein besonderer Dank gilt Herrn Prof. Dr.-Ing. Kai-Uwe Bletzinger, der an seinem Lehrstuhl ein sehr kreatives Arbeitsklima geschaffen hat. Durch die hervorragende Betreuung seinerseits sowie durch die optimale Zusammenarbeit mit den Kollegen am Lehrstuhl wurde diese Arbeit überhaupt erst möglich.

Herrn Prof. Erik Lund Ph.D. danke ich herzlich für das Interesse an meiner Arbeit sowie die Übernahme des Mitberichts.

Meinen Kollegen am Lehrstuhl möchte ich für die freundschaftliche Arbeitsumgebung, die Hilfsbereitschaft sowie die vielen wissenschaftlichen Diskussionen danken. Für die angenehme und lustige Zeit danke ich im Besonderen meinen Bürokollegen Bernd Thomée und André Lähr. Bei Michael Fischer möchte ich mich zudem für die interessante und lehrreiche Zeit während der gemeinsamen Carat++ Entwicklung und den damit einhergehenden leidenschaftlichen Diskussionen bedanken.

Für die umfassende Unterstützung während meiner Studienzeit danke ich besonders herzlich meinen Eltern. Auch während der Promotionszeit waren Sie eine unverzichtbare Stütze. Besonders möchte ich mich bei meiner Freundin Antje bedanken die mich immer vorbehaltlos unterstützt und sich sehr liebevoll um unseren Sohn Moritz gekümmert hat.

Danke an euch alle. Ich hoffe in der Zukunft etwas von dem zurückgeben zu können, das ich von euch erhalten habe.

München, im Juli 2010

Matthias Firl

Contents

1	Introduction	1
1.1	Motivation	1
1.2	Objectives	3
2	Continuum Mechanics	6
2.1	Differential Geometry	6
2.2	Kinematics	8
2.3	Material Law	10
2.4	Equilibrium Equations	10
2.5	Weak Form	11
2.6	Finite Element Discretization	12
3	The Basic Optimization Problem	13
3.1	Standard Formulation of Structural Optimization Problems .	14
3.1.1	Lagrangian Function	15
3.1.2	Karush-Kuhn-Tucker Conditions	15
3.1.3	Dual Function	17
3.2	Optimization Strategies	18
3.2.1	Zero Order Optimization Strategies	18
3.2.2	Gradient Based Optimization Methods	20
3.3	Design Variables	23
3.3.1	Material Optimization	24
3.3.2	Sizing Optimization	25
3.3.3	Shape Optimization	26

3.3.4	Topology Optimization	27
3.4	Response Functions	28
3.4.1	Mass	29
3.4.2	Stress	30
3.4.3	Linear Buckling	32
3.4.4	Eigenfrequency	34
3.4.5	Linear Compliance	35
3.4.6	Nonlinear Compliance	37
3.5	State Derivative	39
3.5.1	Linear State Derivative	39
3.5.2	Nonlinear State Derivative	39
3.6	Optimality Criteria	40
4	Gradient Based Shape Optimization	42
4.1	Convexity and Uniqueness	42
4.2	Shape Parametrization	44
4.2.1	CAD	44
4.2.2	Shape Basis Vectors	45
4.2.3	Morphing	45
4.2.4	Topography	45
4.2.5	FE-based	46
4.3	Sensitivity Analysis	48
4.3.1	Global Finite Difference	49
4.3.2	Variational vs. Discrete	49
4.3.3	Direct Sensitivity Analysis	50
4.3.4	Adjoint Sensitivity Analysis	50
4.3.5	Analytical Sensitivity Analysis	52
4.3.6	Semi-Analytical Sensitivity Analysis	53
4.4	Side Constraints	54
4.5	Size Effects in Response Gradients	56
4.6	Unconstrained Optimization Algorithms	61
4.6.1	Method of Steepest Descent	62

4.6.2	Method of Conjugate Gradients	62
4.7	Constrained Optimization Strategies	64
4.7.1	Method of Feasible Directions	64
4.7.2	Augmented Lagrange Multiplier Method	67
4.8	Line Search	71
5	Exact Semi-Analytical Sensitivity Analysis	73
5.1	Motivation	73
5.2	Problem Description	75
5.2.1	Model Problem I	79
5.2.2	Model Problem II	80
5.3	Exact Semi-Analytical Sensitivities	82
5.3.1	Orthogonalization of Rotation Vectors	84
5.4	Application to 3-d Model Problems	85
5.4.1	Sensitivity Analysis	87
5.4.2	Model Problem III	88
5.4.3	Model Problem IV	90
5.5	Summary	92
6	Regularization of Shape Optimization Problems	94
6.1	Motivation	94
6.2	Projection of Sensitivities	97
6.2.1	Theory of Convolution Integrals	98
6.2.2	Application as Filter Function	100
6.3	Mesh Regularization	105
6.3.1	Motivation	106
6.3.2	Geometrical Methods	107
6.3.3	Mechanical Methods	109
6.3.4	Minimal Surface Regularization	110
6.4	Model Problem V	116
6.5	Model Problem VIa	118
6.6	Model Problem VIb	120

6.7	Summary	122
7	Shape Optimization of Geometrically Nonlinear Problems	123
7.1	General Optimization Goals	124
7.2	Response Functions for Structural Stiffness	125
7.3	Sensitivity Analysis	127
7.4	Structural Imperfections	127
7.5	Simultaneous Analysis and Optimization	128
7.6	Model Problem VII	131
7.7	Summary	134
8	Examples	136
8.1	L-shaped Cowling	136
8.1.1	Filter Radius as Design Tool	137
8.1.2	Mesh and Parametrization Independency	139
8.2	Kresge Auditorium	140
8.3	Car Hat Shelf	144
8.4	Luggage Trunk Ground Plate	149
9	Summary	154
9.1	Modeling Effort	154
9.2	Numerical Effort	155
9.3	Parallelization	155
9.4	Applicability to Industrial Problems	156
9.5	Outlook	156
	Bibliography	163

Chapter 1

Introduction

1.1 Motivation

Structural optimization is a discipline that combines mathematics and mechanics in order to find optimal designs. But what does the term "optimal" mean? Generally, the optimum describes the best possible solution in the relation between parameters and properties. The optimal state denotes a combination of parameters that does not allow for further improvement of properties. Thus, it is the final state where no evolution takes place anymore. For engineers it is an awesome imagination to reach such a point because it means that all progress has come to an end. Will all engineers be unemployed in the future?

A detailed look at natural designs shows that all of them fit into their respective environments in a fascinating way but none of them is optimal. In nature optimal designs can not exist because evolution never ends but a stop of evolution is the necessary condition for an optimal point. In general, each natural design is subjected to permanent evolution which is mainly driven by changing environments. But also in scenarios where environmental conditions are constant continuous evolution takes place. Thus, natural designs are not optimal but usually very close to optimality for the current environment. Otherwise they would have been eliminated due to the evolutionary process.

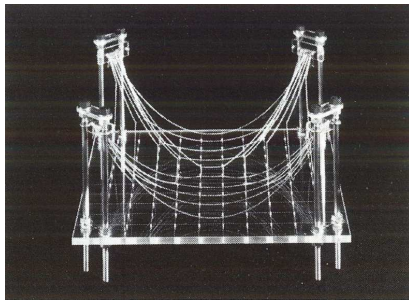
Another important property, one could say the most important property, of natural designs is their efficiency. It is a fact, that more efficient designs have a larger probability to survive in the evolutionary process. Since this process lasts for millions of years the actual designs are very efficient. Thus, the natural evolution process can be formulated as permanent improvement of efficiency which directly yields to optimality.

Similar to natural designs the improvement of structural efficiency is a

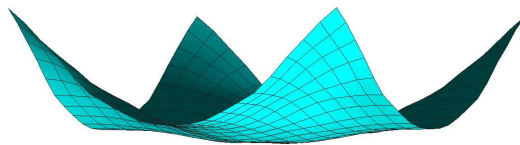
proper way to solve technical optimization problems. Efficiency of technical designs is usually formulated via structural properties like geometry, weight, stiffness, stress distribution, frequency behavior, deformation, etc. The basic goal of structural optimization is to formulate an evolution process that improves specific structural properties. Usually, this evolution process is constrained by other structural properties where the combination of design goal and constraints can be viewed as mathematical description of structural efficiency.

Improvement of structural properties requires their description in a flexible and robust way. The Finite Element Method (FEM) provides a general framework to solve the governing differential equations efficiently and with sufficient accuracy. For this reason numerical structural optimization strategies are closely related to Finite Elements.

It was mentioned that the natural evolution process provides the basis for mathematical optimization strategies. But the actual existing, nearly optimal designs can additionally serve as reference solution for the developed methods. The example depicted in figure 1.1 shows an experimental hanging model developed by Heinz Isler and a respective numerical optimization result. Hanging models allow for an experimental form finding of free form shells. These shell geometries work mainly in membrane action which ensures highly efficient load carrying behavior. Hanging models are



(a) Experimental hanging form [SB03]



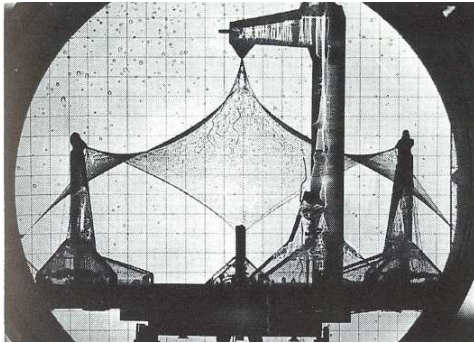
(b) Numerical hanging form

Figure 1.1: Hanging forms

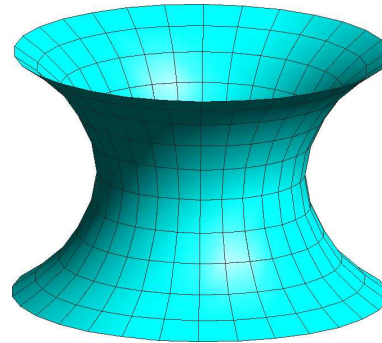
applied by Heinz Isler, Antoni Gaudi, Frei Otto [OT62], [OS66], Felix Candela and many others in order to develop efficient shell geometries.

Another class of natural optimal designs are soap films which form a minimal surface with zero mean curvature that connects the given boundaries. A soap bubble, which has no boundary, is also a minimal surface because its spherical form encloses the internal volume by a minimal surface content.

Soap films find their shape by surface tension which allows for a transfer of this load carrying mechanism to membrane structures made of fabric material, c.f. [BR99], [BFLW08]. In general, the shape of these membranes is determined by the boundaries and if the prestress is isotropic and the boundary is fixed, the resulting membrane structures are also minimal surfaces with zero mean curvature.



(a) Experimental soap film [SB03]



(b) Numerical minimal surface

Figure 1.2: Membrane design by soap film analogy

It is a matter of fact that the shape variety developable by physical experiments is limited. But numerical optimization strategies formulated in an abstract framework do not know about such limits. They can be applied to all types of technical designs in order to improve structural efficiency. Only such highly efficient designs allow for further ecological development of technology because they require only a minimal amount of material and energy during their life cycle. Structural optimization is a flexible, accurate and highly efficient tool to develop structural designs which derogate the environment as few as possible.

1.2 Objectives

The main objective of the present work is the development of fully regularized shape optimization techniques using Finite Element (FE) based parametrization for geometrically linear and nonlinear mechanical problems. The resulting optimization problems have to be solved with gradient based optimization strategies utilizing efficient adjoint sensitivity analysis and exact semi-analytical derivatives.

Chapter 2 presents a short introduction to differential geometry and non-

linear continuum mechanics. This is necessary for the presented mesh regularization methods (chapter 6) and the optimization of geometrically nonlinear problems (chapter 7). The derivations are compact and by far not complete. More information is presented in the referenced literature.

Shape parametrization is one of the most important modeling steps during specification of shape optimization problems. The huge modeling effort of CAGD, Morphing and Shape Basis Vector methods is a serious drawback. FE-based shape parametrization is a general approach that requires only a minimal modeling effort. By using this method the optimization problem is defined on a large design space that does not implicitly restrict the optimal design. Optimization problems with a large amount of design variables require efficient gradient based solution strategies. First order optimization algorithms using adjoint sensitivity analysis are well suited to solve this type of optimization problems, c.f. chapters 3 and 4.

Gradient based optimization strategies require differentiation of FE-data like stiffness and mass matrices, force vectors, etc. Application of analytical derivatives yields to complex and inefficient formulations especially for sophisticated elements like nonlinear shells with EAS, ANS, or DSG enhancements. Semi-analytical sensitivity analysis approximates analytical derivatives by finite differences. It is well known, that this approach results in approximation errors which significantly disturb the accuracy of the gradients. Chapter 5 presents a simple, efficient and robust strategy to prevent this error propagation. The method utilizes correction factors based on dyadic product spaces of rigid body rotation vectors. Several benchmark problems show the accuracy of the corrected gradients and the element insensitive formulation.

Regularization techniques are an essential part of structural optimization methods formulated by FE-based parametrization. Topology, sizing and shape optimization methods depend on effective and robust regularization techniques in order to stabilize the solution process and to prevent mesh dependent results. Application of filter methods for smoothing of gradient data is a well known technique in topology optimization. Chapter 6 presents a filter method based on convolution integrals and its application to shape optimization problems. Type and radius of the utilized filter function are simple and robust parameters which control the curvature of the optimal design. Accurate sensitivity analysis with respect to design variables defined by FE-based parametrization requires an optimal shape of the elements. This is ensured by mesh regularization methods also presented in chapter 6. Geometrically and mechanically based strategies are

introduced and their application to shape optimization of shell structures is shown.

The predominant number of existing optimization strategies is limited to linear mechanical models. But there exists a large number of mechanical problems that cannot be described by linear theories. Chapter 7 presents an approach that combines nonlinear path following strategies and gradient based shape optimization. The introduced algorithm restricts the number of necessary function evaluations to a minimum which is essential for a reasonable solution time. It is shown that application of a geometrically nonlinear objective function and consistent differentiation yields to more efficient design updates and therefore to more efficient optimal designs. Especially in scenarios where shell structures work in membrane action nonlinear kinematics allow for much more reliable optimal results.

The difference between geometrically linear and nonlinear shape optimization is also investigated by the first example of chapter 8. Here the geometry of the well known Kresge Auditorium is optimized in order to show the potential that is hidden in most of the existing buildings. Additionally, the suitability of the developed methods to real life civil engineering optimization problems is shown. Aerospace and automotive industry are also promising application fields for shape optimization strategies utilizing FE-based parametrization. Two examples provided by the Adam Opel GmbH show the application in the field of bead optimization. Improving mechanical properties of thin metal sheets by draw beads is a well known and highly efficient strategy. The crucial and nontrivial problem is the optimal shape of the bead structure. The results of the presented examples prove that shape optimization based on FE-based parametrization is well suited to develop highly efficient, robust and mesh independent bead structures with a minimal modeling effort.

This thesis finishes with some remarks about modeling and numerical effort, parallelization and application to industrial problems. Numerical efficiency and the easy parallelization of the presented algorithms allows their application to huge shape optimization problems with 10^6 or even more design variables. This allows for the solution of large scale industrial optimization problems in a reasonable time.

Chapter 2

Continuum Mechanics

This chapter presents the basic formulations of differential geometry and continuum mechanics of solids. The derivations are restricted to mechanical problems showing large translations and rotations but small strains. All formulations and the examples of the following chapters are also restricted to elastic material behavior formulated by the St.Venant-Kirchhoff material model. The presented relations focus on 3-d free form surfaces with their descriptions of geometry and kinematics.

As a matter of course this chapter provides only a small part of continuum mechanics and differential geometry. Much more detailed introductions to continuum mechanics can be found in [Hol00], [Hau02] and [BW08]. More information about differential geometry is presented in [Car76] and [Hsi81].

2.1 Differential Geometry

Differential geometry is a tool to describe the geometry of complex three dimensional bodies. Geometrically nonlinear mechanics require the formulation of the initial geometry and the deformed geometry denoted by reference configuration and actual configuration respectively. To avoid confusion in defined quantities the reference configuration is described by capital letters. Lower case letters are used for the actual configuration.

Bodies with curved boundaries are conveniently described via curvilinear coordinates θ . In the following chapters this coordinate definition is used for the applied shell and membrane elements as well as for specified nodal design variables. The reference configuration describes the undeformed state by reference coordinates \mathbf{X} . The base vectors in this configuration are denoted by \mathbf{G}_i . They are defined as partial derivatives of the reference position vector \mathbf{X} with respect to the curvilinear coordinates θ^i . The index i is

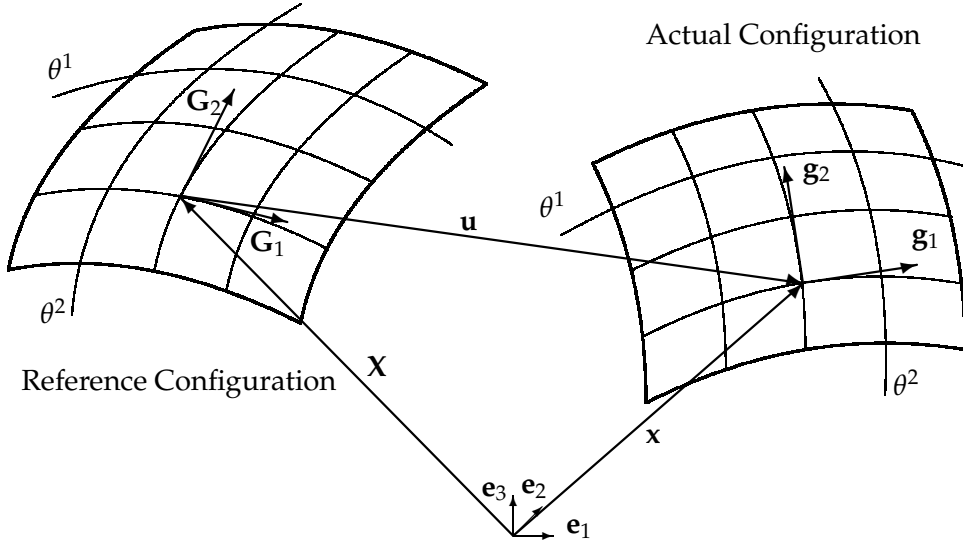


Figure 2.1: Geometry and kinematics of curved 2-d bodies

defined as $i \in \{1,2\}$ for two dimensional structures like shells and membranes and $i \in \{1,2,3\}$ for three dimensional structures like solids.

$$\mathbf{G}_i = \frac{\partial \mathbf{X}}{\partial \theta^i} = \mathbf{X}_{,i}. \quad (2.1)$$

The actual configuration describes the deformed geometry based on the reference coordinates \mathbf{X} and the displacement field \mathbf{u} via

$$\mathbf{x} = \mathbf{X} + \mathbf{u}. \quad (2.2)$$

The base vectors of the actual configuration \mathbf{g}_i are defined as the partial derivative of the actual coordinates \mathbf{x} with respect to θ^i .

$$\mathbf{g}_i = \frac{\partial \mathbf{x}}{\partial \theta^i} = \mathbf{x}_{,i}. \quad (2.3)$$

Definition of base vectors in reference and actual configuration allows computation of covariant metric coefficients in reference configuration and actual configuration by

$$G_{ij} = \mathbf{G}_i \cdot \mathbf{G}_j \quad \text{and} \quad g_{ij} = \mathbf{g}_i \cdot \mathbf{g}_j \quad (2.4)$$

respectively. The contravariant metric coefficients follow from simple matrix inversion of the covariant metric coefficients by

$$G^{ij} = \{G_{ij}\}^{-1} \quad \text{and} \quad g^{ij} = \{g_{ij}\}^{-1}. \quad (2.5)$$

Covariant and contravariant base vectors are related by the well known Kronecker delta. This relation holds in the reference as well as in the actual configuration. It is formulated by

$$\mathbf{G}_i \cdot \mathbf{G}^j = \mathbf{g}_i \cdot \mathbf{g}^j = \delta_i^j \quad \text{with} \quad \delta_i^j = 0 \quad \forall i \neq j, \quad \delta_i^j = 1 \quad \forall i = j. \quad (2.6)$$

Specification of contravariant metric coefficients permits a straight forward computation of the contravariant basis vectors in reference configuration

$$\mathbf{G}^i = G^{ij} \mathbf{G}_j \quad (2.7)$$

and actual configuration

$$\mathbf{g}^i = g^{ij} \mathbf{g}_j. \quad (2.8)$$

Based on metric coefficients and base vectors the metric tensor (unit tensor) is defined by

$$\mathbf{G} = G_{ij} \mathbf{G}^i \otimes \mathbf{G}^j = G^{ij} \mathbf{G}_i \otimes \mathbf{G}_j. \quad (2.9)$$

The metric tensor substitutes the usual unit tensor $\mathbf{I} = \mathbf{e}_i \otimes \mathbf{e}_j$ which is not applicable to geometry representation in curvilinear coordinates.

Shell and membrane formulations often require the definition of the surface normal in reference and actual configuration denoted by \mathbf{G}_3 and \mathbf{g}_3 respectively. The surface normal coordinates are not separated in covariant and contravariant descriptions. Usually the vectors \mathbf{G}_3 and \mathbf{g}_3 are L_2 normalized. In the reference configuration they follow from the cross product of the reference basis vectors by

$$\mathbf{G}_3 = \frac{\mathbf{G}_1 \times \mathbf{G}_2}{|\mathbf{G}_1 \times \mathbf{G}_2|} = \mathbf{G}^3 = \frac{\mathbf{G}^1 \times \mathbf{G}^2}{|\mathbf{G}^1 \times \mathbf{G}^2|}. \quad (2.10)$$

The computation of the actual surface normal vector reads as

$$\mathbf{g}_3 = \frac{\mathbf{g}_1 \times \mathbf{g}_2}{|\mathbf{g}_1 \times \mathbf{g}_2|} = \mathbf{g}^3 = \frac{\mathbf{g}^1 \times \mathbf{g}^2}{|\mathbf{g}^1 \times \mathbf{g}^2|}. \quad (2.11)$$

More detailed information about geometry description in curvilinear coordinates and computation of curvatures can be found in [Wüc07] and the references therein.

2.2 Kinematics

Kinematic equations relate displacements and rotations of a structure with the shape modification of a material point. The kinematic equations are

formulated with respect to the reference configuration which is common practice in solid mechanics.

The displacement field \mathbf{u} describes the geometry modification from reference to actual configuration by

$$\mathbf{u} = \mathbf{x} - \mathbf{X}. \quad (2.12)$$

Transformations between reference and actual configuration are performed via the deformation gradient \mathbf{F} . This unsymmetric second order tensor is defined as

$$\mathbf{F} = \frac{\partial \mathbf{x}}{\partial \mathbf{X}}. \quad (2.13)$$

Application of chain rule of differentiation to equation (2.3) allows the transformation of the covariant basis vectors from the reference configuration to the actual configuration by

$$\mathbf{g}_i = \frac{\partial \mathbf{x}}{\partial \mathbf{X}} \frac{\partial \mathbf{X}}{\partial \theta^i} = \mathbf{F} \mathbf{G}_i. \quad (2.14)$$

Modification of equation (2.14) permits direct computation of the deformation gradient by the covariant basis vectors of the actual configuration and the contravariant basis vectors of the reference configuration

$$\mathbf{F} = \mathbf{g}_i \otimes \mathbf{G}^i. \quad (2.15)$$

A complete survey of relations between deformation gradient and basis vectors is presented in [Bis99] and [Wüc07].

The definition of the deformation gradient and metric tensor affords the formulation of strain measures usable for geometrically nonlinear problems. In solid mechanics the strains are mostly formulated on the reference configuration by the Green-Lagrange strain tensor \mathbf{E} defined by

$$\mathbf{E} = \frac{1}{2} \left(\mathbf{F}^T \mathbf{F} - \mathbf{G} \right). \quad (2.16)$$

Usually the tensor product $\mathbf{F}^T \mathbf{F}$ is defined as right Cauchy Green deformation tensor by $\mathbf{C} = \mathbf{F}^T \mathbf{F}$. The push forward of the Green-Lagrange strain tensor to the actual configuration is defined as Euler-Almansi strain tensor \mathbf{A} . This operation applies the inverse deformation gradient \mathbf{F}^{-1} and its transposed \mathbf{F}^{-T} by

$$\mathbf{A} = \mathbf{F}^{-T} \mathbf{E} \mathbf{F}^{-1}. \quad (2.17)$$

Green-Lagrange as well as Euler-Almansi strains are not well suited to handle large strain problems. Therefore Hencky or Biot stresses should be used. The mechanical problems discussed in this thesis are restricted to small strains. Thus, the kinematic relations are formulated by Green-Lagrange or Euler-Almansi strains respectively.

2.3 Material Law

The material law establishes the relation between strains and stresses. Stress and strain measures are formulated as energetically conjugate pairs which allows the expression of energy quantities by products between stress and strain. The formulation in curvilinear coordinates additionally require the stress description in covariant basis vectors to eliminate the metric influence in scalar products.

The second Piola-Kirchhoff stress \mathbf{S} and Green-Lagrange strain \mathbf{E} are an energetically conjugated pair related by the fourth order material tensor \mathbf{C} formulated in reference configuration

$$\mathbf{S} = \mathbf{C} \cdot \mathbf{E} \quad \text{with} \quad \mathbf{C} = C^{ijkl} \mathbf{G}_i \otimes \mathbf{G}_j \otimes \mathbf{G}_k \otimes \mathbf{G}_l. \quad (2.18)$$

Linear elastic and isotropic material behavior for geometrically nonlinear problems is expressed by the Saint-Venant-Kirchhoff material model with two Lamé constants λ and μ . They can be expressed by the material parameters Young's modulus E and Poisson's ratio ν with the formulations

$$\lambda = \frac{E \cdot \nu}{(1 + \nu) \cdot (1 - 2\nu)} \quad \text{and} \quad \mu = \frac{E}{2(1 + \nu)}. \quad (2.19)$$

The Lamé constants allow a straight forward formulation of the material tensor components C^{ijkl} by

$$C^{ijkl} = \lambda G^{ij} G^{kl} + \mu (G^{ik} G^{jl} + G^{il} G^{kj}) \quad (2.20)$$

2.4 Equilibrium Equations

The governing equation to describe equilibrium in structural mechanics of closed systems is balance of linear momentum. It enforces that the change of body momentum is equal to the sum of all forces acting on this body. Detailed derivation of balance principles can be found in [Hol00].

The local form of the static momentum balance is defined by

$$\text{div}(\mathbf{FS}) + \rho \mathbf{b} = 0 \quad (2.21)$$

with density ρ , volume forces \mathbf{b} and the divergence with respect to the reference configuration $\text{div}(\cdot)$.

The formulation of equation (2.21) as boundary value problem of structural mechanics requires Dirichlet boundary conditions

$$\mathbf{u} = \hat{\mathbf{u}} \quad \text{on} \quad \Gamma_u \quad (2.22)$$

and Neumann boundary conditions

$$\mathbf{t} = \hat{\mathbf{t}} \quad \text{on} \quad \Gamma_t \quad (2.23)$$

with $\Gamma_u \cap \Gamma_t = 0$.

The set of balance equation, kinematic relation, constitutive relation and boundary conditions completely describes structural models. But the direct solution for the unknown displacement field \mathbf{u} is only possible for specific geometries and boundary conditions. The reformulation of the boundary value problem in a weak form provides the basis for a spatial discretization of the problem by finite elements. The discretized form of the boundary value problem can be solved for arbitrary geometries and boundary conditions.

2.5 Weak Form

The balance equation (2.21) and the Neumann boundary conditions (2.23) are reformulated to an integral expression. It is enforced that the residuum of this relation weighted with test functions vanishes in an integral sense.

$$\int_{V_X} (-\text{div}(\mathbf{FS}) - \rho\mathbf{b}) \mathbf{w} d\Omega_X + \int_{\partial V_X} (\mathbf{t} - \hat{\mathbf{t}}) \mathbf{w} d\Gamma_t = 0 \quad (2.24)$$

with $V_X \subset \Omega_X$ and $\Gamma_t \subset \partial\Omega_X$. By definition the test functions \mathbf{w} have to fulfill the Dirichlet boundary conditions on Γ_u . Ω_X and $\partial\Omega_X$ describe the reference domain and the boundary of the reference domain respectively. After application of Cauchy's theorem and the Gaussian integral theorem [Hol00] equation (2.24) is reformulated to

$$\int_{V_X} (\mathbf{S}\mathbf{F}^T \cdot \text{grad}(\mathbf{w})) d\Omega_X = \int_{V_X} \rho\mathbf{b}\mathbf{w} d\Omega_X + \int_{\partial V_X} \hat{\mathbf{t}}\mathbf{w} d\Gamma_t \quad (2.25)$$

where $\text{grad}(\cdot)$ denotes the gradient with respect to the reference configuration. The term $\mathbf{F}^T \text{grad}(\mathbf{w})$ is defined as virtual Green strain

$$\mathbf{S} \cdot (\mathbf{F}^T \text{grad}(\mathbf{w})) = \mathbf{S} \cdot \frac{1}{2} (\mathbf{F}^T \text{grad}(\mathbf{w}) + (\text{grad}(\mathbf{w}))^T \mathbf{F}) = \mathbf{S} \cdot \delta\mathbf{E} \quad (2.26)$$

where the virtual Green strain is the Gateaux differential of the Green Lagrange strain tensor in the direction of \mathbf{w} .

The weak formulation of the boundary value problem of structural mechanics is defined as:

Find $\mathbf{u} \in \mathcal{V}_{\hat{\mathbf{u}}}$ such that $\forall \mathbf{w} \in \mathcal{V}$

$$\int_{V_X} \mathbf{S} \cdot \delta \mathbf{E} d\Omega_X - \int_{V_X} \rho \mathbf{b} \mathbf{w} d\Omega_X - \int_{\partial V_X} \hat{\mathbf{t}} \mathbf{w} d\Gamma_t = 0. \quad (2.27)$$

$\mathcal{V}_{\hat{\mathbf{u}}}$ and \mathcal{V} describe the spaces for the test functions. They are defined by

$$\mathcal{V}_{\hat{\mathbf{u}}} = \{\mathbf{u} \in \mathbf{H}^1(\Omega_X) : \mathbf{u} = \hat{\mathbf{u}} \text{ on } \Gamma_u\} \quad \text{and} \quad (2.28)$$

$$\mathcal{V} = \{\mathbf{u} \in \mathbf{H}^1(\Omega_X) : \mathbf{u} = \mathbf{0} \text{ on } \Gamma_u\}. \quad (2.29)$$

The space $\mathbf{H}^1(\Omega_X)$ defines the Sobolev space of function with square integrable values and first derivatives in Ω_X . From equation 2.28 follows that applied Dirichlet boundary conditions must be compatible with the test functions. More information about Sobolev spaces which defines the mathematical basis of the Finite Element discretization method can be found in [BS94]. The mechanical interpretation of equation 2.27 is that a the energy of a system in equilibrium does not change by the variation $\delta \mathbf{E}$, which holds at all extremum points of (2.27).

2.6 Finite Element Discretization

Equation (2.27) formulates the weak form of the nonlinear boundary value problem continuously. Due to discretization by finite elements the continuous problem is approximated by a discrete problem where distributed quantities are expressed by discrete nodal values and shape functions. Free form surfaces are usually discretized by quadrilateral or triangle elements. The basic element properties follow from the implemented kinematic assumptions, e.g. Kirchhoff hypothesis or Reissner-Mindlin hypothesis for shell elements. The applicability of the elements for certain mechanical problems and their locking behavior strongly depends on the kinematic assumptions and the internal degrees of freedom. For detailed formulations of the applied membrane and shell elements is referred to [Wüc07] and [Bis99] respectively.

The resulting nonlinear set of algebraic equations has to be linearized, e.g. by a linear Taylor series expansion which allows the solution by an iterative Newton-Raphson procedure until the computed displacement field fulfills the equilibrium condition with sufficient accuracy. This procedure is elaborated frequently in standard textbooks ([ZTZ00], [BLM00], [Bat95], etc.) and should not be repeated here.

Chapter 3

The Basic Optimization Problem

The formulation of complex mechanical processes in abstract, complete and reasonable optimization models is the most important step of structural optimization. Usually, an optimization problem is characterized by an objective function and several constraints. In many cases even the formulation of these functions requires a deep knowledge of the optimization strategy that should be applied. Another crucial point is the specification of the design variables. Based on this choice special optimization strategies like sizing, shape or topology optimization have to be applied. The type of applicable mathematical optimization algorithms is determined not by the type but by the number of design variables and by the differentiability of the response functions. Usually, gradient based strategies are better suited for a large number of design variables, whereas zero order methods are applicable to problems where gradients cannot be computed. Several successful optimization strategies are based on optimality criteria which usually yield to very fast and robust solution procedures.

This chapter is intended to introduce the most basic components of structural optimization problems like optimization strategies, optimization algorithms, response functions, sensitivity analysis and state derivatives. This allows precise and clear presentations of more detailed topics of structural optimization in the following chapters. Additional information to the short introductions presented here can be found in the classical textbooks of shape optimization, e.g. [HG92], [Aro04], [Kir92] and [Van84].

3.1 Standard Formulation of Structural Optimization Problems

Each mechanical optimization problem can be formulated in the standard form

$$\begin{aligned}
 &\text{Minimize} && f(\mathbf{s}, \mathbf{u}), && \mathbf{s} \in \mathbf{R}^n && (3.1) \\
 &\text{such that} && g_i(\mathbf{s}, \mathbf{u}) \leq 0, && i = \{1, \dots, n^g\} \\
 &&& h_j(\mathbf{s}, \mathbf{u}) = 0, && j = \{1, \dots, n^h\} \\
 &&& \mathbf{s}_l \leq \mathbf{s} \leq \mathbf{s}_u
 \end{aligned}$$

with the design variable vector \mathbf{s} , the state variables (e.g. displacements) \mathbf{u} , objective function f , inequality constraints g , equality constraints h and the lower and upper side constraints to the design variables \mathbf{s}_l and \mathbf{s}_u respectively.

The design variable type characterizes the basic properties of a structural optimization problem. Basic types of variables are material parameters, cross section parameters, geometrical parameters and density distribution in the domain. The choice of parameter type yields to different optimization strategies introduced in section 3.3. The size n of the design space \mathbf{R}^n specifies the number of independent variables. They determine the applicable optimization algorithms as well as the numerical effort, c.f. section 3.2.

The objective function or cost function is the measure to judge the quality of the current design. Objectives can be formulated by several sub-functions which yields to multi-objective optimization problems. In general these type of optimization problems need the definition of an additional rule to select the best solution from all solutions on the Pareto front [EKO90]. All the following derivations and examples are based on a single objective function.

The inequality constraints g_i and the equality constraints h_j specify the feasible domain, where the number of applied inequality constraints and equality constraints are denoted by n^g and n^h , respectively. During the optimization process an inequality constraint may become active, inactive or redundant. Equality constraints are only active or redundant. A basic property of the optimization problem is that the number of active constraints must be smaller or equal to the number of design variables.

Subsequently, objective function and constraint equations are often denoted as response functions because of their basic property: the description

of a structural response. Common response functions in structural optimization problems are compliance, mass, stress, eigenfrequency, buckling load and more. A detailed description of several, frequently used response functions is presented in section 3.4.

3.1.1 Lagrangian Function

The reformulation of the set of equations in (3.1) to a single function is denoted as Lagrangian function. The Lagrangian function is formulated in the primal variables \mathbf{s} and the dual variables $\boldsymbol{\lambda}$ and $\boldsymbol{\mu}$. The minimization of (3.1) yields to a saddle point with the same function value as the original objective but without specification of external constraint equations. The general formulation of the Lagrangian function reads as

$$L(\mathbf{s}, \mathbf{u}, \boldsymbol{\lambda}, \boldsymbol{\mu}) = f(\mathbf{s}, \mathbf{u}) + \sum_{i=1}^{n^g} \lambda_i \cdot g_i(\mathbf{s}, \mathbf{u}) + \sum_{j=1}^{n^h} \mu_j \cdot h_j(\mathbf{s}, \mathbf{u}); \quad \lambda_i > 0, \mu_j \neq 0. \quad (3.2)$$

Active constraints defined in (3.1) are zero by definition whereby the Lagrangian function merges to the objective for arbitrary Lagrange multipliers $\boldsymbol{\lambda}$ and $\boldsymbol{\mu}$. Equation 3.2 provides the basis for several constraint optimization strategies like Penalty Methods ([HG92]) or Augmented Lagrange Multiplier Methods (c.f. section 4.7.2).

3.1.2 Karush-Kuhn-Tucker Conditions

The Karush-Kuhn-Tucker Conditions (KKTC) define necessary optimality conditions for the stationary point of the Lagrangian function. They are defined as partial derivatives of the Lagrangian function with respect to the design variables \mathbf{s} and the Lagrange multipliers $\boldsymbol{\lambda}$ and $\boldsymbol{\mu}$ respectively.

$$\nabla_{\mathbf{s}} f(\mathbf{s}, \mathbf{u}) + \sum_{i=1}^{n^g} \lambda_i \nabla_{\mathbf{s}} g_i(\mathbf{s}, \mathbf{u}) + \sum_{j=1}^{n^h} \mu_j \nabla_{\mathbf{s}} h_j(\mathbf{s}, \mathbf{u}) = 0 \quad (3.3)$$

$$\lambda_i \nabla_{\lambda_i} L(\mathbf{s}, \mathbf{u}, \boldsymbol{\lambda}, \boldsymbol{\mu}) = \lambda_i g_i(\mathbf{s}, \mathbf{u}) = 0 \quad (3.4)$$

$$\nabla_{\mu_j} L(\mathbf{s}, \mathbf{u}, \boldsymbol{\lambda}, \boldsymbol{\mu}) = h_j(\mathbf{s}, \mathbf{u}) = 0 \quad (3.5)$$

$$\lambda_i \geq 0 \quad (3.6)$$

Equations 3.4, 3.5 and 3.6 enforce that constraints must be active at the optimum. Inequality constraints require the distinction between active and

inactive constraints. Active inequality constraints are characterized by

$$\lambda_i \geq 0 \quad \text{and} \quad g_i(\mathbf{s}, \mathbf{u}) = 0. \quad (3.7)$$

The product of the constraint value g_i and the respective Lagrange multiplier λ_i is always equal to zero. Thus, the value of the Lagrangian function (3.2) is not affected. Inactive inequality constraints are defined by

$$\lambda_i = 0 \quad \text{and} \quad g_i(\mathbf{s}, \mathbf{u}) < 0. \quad (3.8)$$

Also in this case the product of Lagrange multiplier and constraint value is equal to zero but inactive constraints are not considered in the Lagrangian function. The set of active inequality constraints together with the non-redundant equality constraints is commonly denoted as active set of constraints.

Equation 3.3 formulates an equilibrium between the objective gradient and the scaled constraint gradients. This equilibrium condition is visualized in figure 3.1. The picture shows a two dimensional optimization problem

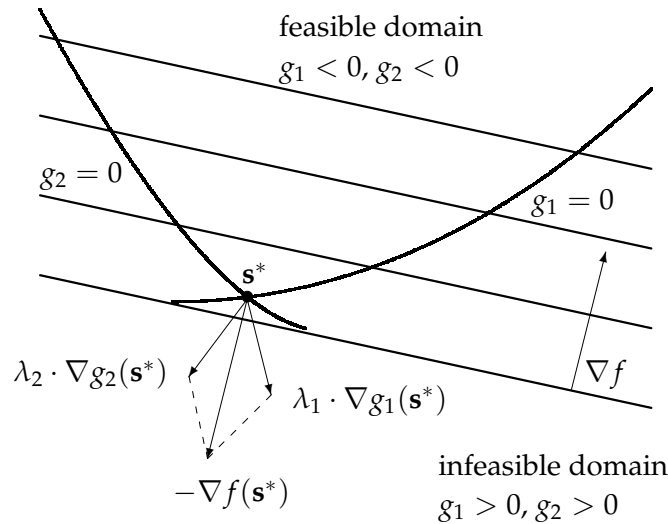


Figure 3.1: Graphical interpretation of KKT conditions at the optimum

with a linear objective f and two convex nonlinear inequality constraints g_1 and g_2 . The optimum at design point \mathbf{s}^* is clearly a constrained optimum defined by $g_1 = g_2 = 0$. In this example equation 3.3 is established by $-\nabla f = \lambda_1 \cdot \nabla g_1 + \lambda_2 \cdot \nabla g_2$.

3.1.3 Dual Function

As introduced in section 3.1.1 the Lagrangian function is defined in primal variables \mathbf{s} and dual variables λ and μ . Provided that primal variables can be expressed via dual variables by

$$\mathbf{s} = \mathbf{s}(\lambda, \mu) \quad (3.9)$$

the Lagrangian function L merges to the dual function D by

$$L(\mathbf{s}(\lambda, \mu), \mathbf{u}, \lambda, \mu) = D(\mathbf{u}, \lambda, \mu) = \min_{\mathbf{s}} L(\mathbf{s}, \mathbf{u}, \lambda, \mu). \quad (3.10)$$

The dual function allows solution of the optimization problem via maximization of D with variables λ and μ .

In general, it is not possible to express the primal variables explicitly in dual variables as denoted in equation (3.9). Whenever response functions can be formulated as separable functions, the primal variables can be expressed in dual variables. Equation 3.11 presents an example for a separable function.

$$f(\mathbf{s}) = f_1(s_1) + f_2(s_2) + f_3(s_3) + \dots + f_n(s_n) \quad (3.11)$$

Global approximation methods like the Method of Moving Asymptotes (MMA) [Sva87], [Sva02] are designed in order to allow a formulation of the dual function. Linear programming (LP) methods approximate the nonlinear optimization problem by linear functions. These methods also allow for a straight forward formulation of the dual function.

Uzawas method [AHU58], [Ble90] is a well known iterative approach that incorporates the dual function in the solution of the constrained optimization problem. Each iteration step of Uzawas method contains two major steps:

1. Compute new design \mathbf{s}^k by minimization of the Lagrangian function (3.2) for fixed Lagrange multipliers
2. compute new Lagrange multipliers by maximization of the dual function (3.10) for the actual design \mathbf{s}^k

The staggered minimization-maximization procedure of Uzawas method directly computes the stationary point of the Lagrangian function.

3.2 Optimization Strategies

There exists a variety of algorithms to solve the problem formulated in equation 3.1. In general, these algorithms can be separated according to the order of information they take into account. Zero order methods solve the optimization problem based on function evaluations of the response functions. First order methods utilize function evaluations and the first order derivatives of the system response with respect to the design variables. Second order methods additionally work with second order derivatives. Usually, the order of information is a measure for efficiency of the optimization strategy.

3.2.1 Zero Order Optimization Strategies

Zero order methods are applied for highly complex optimization problems where mechanical problem and objective cannot be described in a closed form, e.g. process optimization or optimization of car design for crash analysis. Another application field of zero order strategies are problems with discontinuous derivatives, e.g. optimization problems with discrete variables. In both cases it is not possible to compute continuous gradients which prevents application of gradient based strategies. Thus, zero order optimization methods are applied for this type of problems. These methods can be separated in biological methods, e.g. evolutionary strategies or genetic algorithms and stochastic methods.

Evolutionary Strategies

Evolutionary strategies are models of the natural evolution process which is well formulated in the term "Survival of the Fittest" published by Herbert Spencer in 1864. The basic steps in evolutionary optimization algorithms are initialization, mutation and selection. In the initialization process a parent and a descendant are described by a set of genes. The genes of the parent describe the starting design of optimization. In the mutation process the parent produces a new descendant with slightly modified genes where the deviations are independent and to a certain amount random. Due to selection the parent of the next generation is chosen based on capacity of survival. The process of mutation and selection is repeated until convergence of the optimization problem.

Genetic Algorithms

Genetic algorithms are based on evolutionary strategies but with more

complex mutation and selection mechanisms. The general formulation separates the following steps: initialization, selection, recombination and mutation. The initialization defines a set of m individuals. Each individual is represented by its genotype consisting of the genes. For genetic algorithms the genotype is coded in a binary bit string. In the selection phase two parents are chosen from the individuals based on fitness or contribution to the objective. In the recombination step a new generation of m individuals is generated. The genes of the descendants are estimated by crossover of parent genes with random modifications. Due to mutation the bits of the genotype are slightly modified by random processes. The steps selection, recombination and mutation are repeated until convergence of the optimization problem.

The basic drawback of biological optimization strategies is the numerical effort for large optimization problems. This effort is related to the number of individuals and the complexity of fitness evaluation. For acceptable convergence the number of individuals in each generation must be large enough to allow a good measurement of genotype modifications. Hence, fitness evaluation is necessary for many individuals in each optimization step. For structural optimization problems the fitness of an individual is related to the structural properties usually formulated in a system of equations. Thus, the equation system has to be solved for each individual in each optimization step which results in a huge numerical effort. More detailed information about evolutionary strategies and genetic algorithms is presented in [Sch95] and [Aro04].

Stochastic Algorithms

The basic goal of stochastic search algorithms is to find the global minimum of the objective, also for non convex functions, c.f. section 4.1. There exist several stochastic search methods like Monte Carlo Method, Multi-start Method, Clustering Method, Simulated Annealing and many more. Basically all stochastic methods consecutively perform a global search and a local search. The global search localizes possible regions for minima. This allows for global convergence behavior. The local search finds the minimum in a specific region. This improves efficiency of the method due to reduced number of function evaluations. It is referred to [Aro04] for more information about stochastic search algorithms.

In general, stochastic algorithms need a huge number of function evaluations to converge. For large structural optimization problems with many design and state variables this yields to long computation times because

nearly all response function evaluations need the solution of an equation system. This property causes inefficiency of biological and stochastic search methods for the solution of structural optimization problems.

An efficient method to improve the convergence behavior of stochastic search strategies is the construction of response surfaces based on the function evaluations. This allows for consideration of undetermined parameters which are tackled by the so called Robust Design methods, c.f. [Jur07] and the reference therein. The response surfaces can additionally be used to compute gradient information, which reduces the number of necessary function evaluations significantly. Unfortunately this means the loss of global convergence behavior.

3.2.2 Gradient Based Optimization Methods

In the following, gradient based optimization strategies denote methods that utilize derivatives of response functions with respect to the design variables to compute an improved design. Gradient computations on response surfaces computed by global approximation techniques are not discussed here.

The gradients or sensitivities can be computed by several different methods introduced in section 4.3. Based on the gradients of the response functions at a specific design all methods utilize a characteristic method to compute a design update direction. The final design update is then computed by the scaling of the design update direction with the step length factor. In general, this step length factor is determined by a one dimensional line search, c.f. section 4.8. A well known exception of this rule is Newtons method which directly computes a search direction with optimal length. This search direction can be applied directly as design update.

Gradient based optimization strategies can be separated in direct methods and local approximation methods. Direct methods solve the optimization problem established in (3.1) directly. This may result in bad convergence behavior due to ill posed problem formulations. Local approximation methods compute at each step an approximation of the optimization problem in order to ensure proper consideration of constraints or efficient search directions. Reasonable local approximations (e.g. by penalty factors) improve the robustness of the problem seriously and permit efficient solution strategies. A second characterization of gradient based optimization methods offers their applicability to constrained optimization problems. In general, constrained optimization problems are more difficult to solve than

Direct Methods		Local Approximation Methods
Unconstrained	Constrained	Constrained
Steepest Descent	Feasible Directions	Method of Moving Asymptotes
Conjugate Gradients	Gradient Projection	Exterior / Interior Penalty Methods
Variable Metric	Simplex	Augmented Lagrange Multiplier

Table 3.1: Summary of first order methods

unconstrained problems which yields to more complex solution algorithms and slower convergence.

First Order Methods

First order methods apply first order gradients but no second order gradients in the computation of the search direction. The most important first order methods are listed in table 3.1. Famous direct optimization methods for unconstrained problems are the Steepest Descent (SD) and the Conjugate Gradient (CG) Method. In most cases the CG-method yields to faster convergence with a minimal increase in numerical effort compared to steepest descent algorithms. More information about both methods can be found in sections 4.6.1 and 4.6.2. Variable Metric Methods [Van84] or quasi Newton methods are based on approximations of the Hessian or the inverse Hessian. They are usually even more efficient than CG-methods. The most famous update schemes are the Broyden-Fletcher-Goldfarb-Shanno (BFGS) update and the Davidon-Fletcher-Powell (DFP) update. There exist two different derivations for the update schemes which consecutively improve the approximation of the Hessian or the inverse Hessian by first order derivatives [Aro04]. The approximation of the inverse Hessian is numerically more efficient because the evaluation of the search direction reduces to a matrix vector product. Approximating the Hessian itself leads to a system of equations which has to be solved in order to compute the search direction. In contrast to exact Newton methods quasi Newton methods need a line search (c.f. section 4.8) to ensure convergence. Establishing the full Hessian or inverse Hessian requires huge amounts of memory because both matrices are in general dense. Efficient implementations of quasi Newton methods use 'memory less' algorithms which store only the update vectors and not the full matrix. In many algorithms the Hessian or inverse Hessian update starts with the identity matrix. A more efficient

approach for the initialization of the matrix is presented in [Ble90].

The Method of Feasible Directions (MFD) is straight forward extension of the CG algorithm to constrained optimization problems. As soon as a constraint violation is monitored the next design update contains gradient information of the violated constraint which yields to a design update direction pointing back into the feasible domain. This approach permits robust and fast implementations but it never leaves the feasible domain and thus it cannot start at infeasible points. The basic theory of the feasible directions method and a suitable implementation is presented in section 4.7.1. The Augmented Lagrange Multiplier (ALM) method is also a popular constrained optimization algorithm. This method is based on a penalization of the constraint terms in the Lagrangian function. The influence of the penalty term on the overall solution decreases as soon as the algorithm reaches the optimum. It is referred to section 4.7.2 for more information about this method. The Exterior / Interior Penalty Function Methods, the Gradient Projection Method and the Simplex Method are further well known optimization strategies which are not presented in detail here. More information about these methods and possible application fields are shown in [HG92]. The Method of Moving Asymptotes (MMA) approximates the original optimization problem by a convex function which shows an asymptotic behavior close to lower and upper boundaries. This approximation allows for an easy derivation of the dual function and robust solution algorithms. More detailed information about MMA is presented in [Sva87], [Sva02], [Ble90], [Ble93] and [Dao05].

In general, first order methods are convenient for the solution of structural optimization problems. They need a small number of iteration steps and a small number of function evaluations compared to zero order methods. Each iteration step of a first order method usually consists of a first order sensitivity analysis and a few number of system evaluations for the line search. Adjoint formulations of sensitivity analysis allow an efficient gradient computation for many objective functions, c.f. section 4.3.

Second Order Methods

Second order methods utilize first order derivatives and second order derivatives (stored in the Hessian matrix) to compute a design update. In general, evaluation of second order information improves the quality of the search direction but the computation is very time consuming and storage of the Hessian matrix needs much memory. Highly non convex optimization problems also reduce the worthiness of second order gradients. This drawback is circumvented by application of local approximation methods.

The most important second order optimization algorithms are listed in table 3.2.

Unconstrained	Constrained	
Newtons method	Sequential Quadratic Programming (SQP)	Pro-

Table 3.2: Summary of second order methods

Newton methods are based on a second order Taylor series expansion of the stationary condition of the objective at a specific point. This directly results in a linear system of equations which has to be solved for the next design update. Due to the exact linearization of the problem Newtons method does not need a line search. Additionally, it shows quadratic convergence behavior close to the optimum. The basic drawback of this approach is the computation of second order derivatives to establish the symmetric Hessian. In general, it needs computation of $n(n + 1)/2$ second order derivatives where n is the number of design variables. This tremendous numerical effort motivates formulation of quasi Newton methods which are based on approximations of the Hessian or the inverse Hessian by first order derivatives. More detailed information about Newton and quasi Newton methods as well as illustrative examples are presented in [Aro04].

The straight forward extension of Newton methods to constrained optimization problems is the Sequential Quadratic Programming (SQP) method also denoted as Constrained Variable Metric (CVM) or Recursive Quadratic Programming (RQM) methods. SQP methods apply a second order Taylor series expansion of the Lagrangian function (3.2) which yields to a Hessian containing second order objective derivatives and first order constraint derivatives. Thus, the objective is approximated quadratically whereas constraints are approximated only linearly. The BFGS update is also applied for SQP methods to reduce the numerical effort to compute the Hessian with the consequence of a necessary line search. SQP methods are explained in detail in [Ble90], [Dao05], [Aro04] and [HG92].

3.3 Design Variables

The choice of design variables defines basic properties of the optimization problem. Based on the design variables structural optimization problems are separated in material, sizing, shape and topology optimization. The

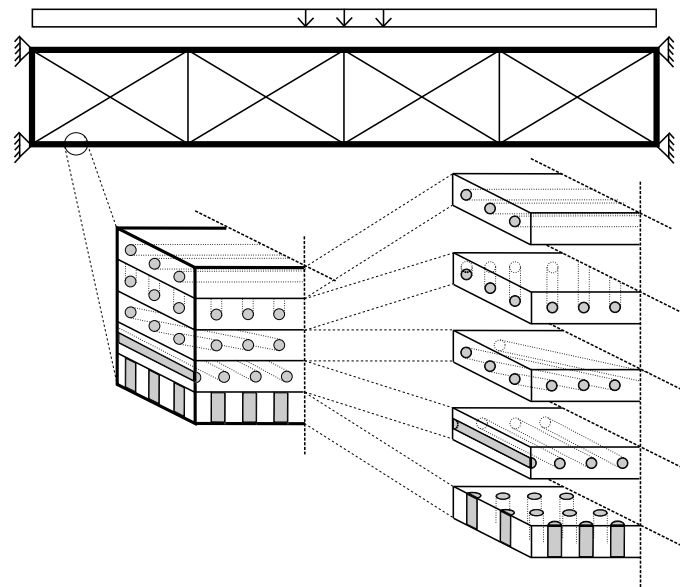


Figure 3.2: Fiber angles and stacking sequence of composite material

numerical effort of the sensitivity analysis as well as the overall robustness of the optimization problem is strongly related to the choice of design variables.

3.3.1 Material Optimization

Material optimization problems utilize material parameters as design variables whereas topology and geometry of the structural model remain constant. Examples for material variables are distribution of concrete reinforcement, direction of fiber angles or layer sequence in composite materials, c.f. figure 3.2. It shows the layer sequence of a composite structure where each layer is characterized by a different fiber angle. The derivatives of the response functions with respect to material variables are related to the material description only which ends up in relatively simple formulations. In several material optimization problems design variables are not continuous parameters, e.g. specified fiber angles or number of plies. Differentiation with respect to such parameters yields to integer programming problems, c.f. [HG92], [Aro04].

A very flexible method of material optimization is the so called Free Material Optimization (FMO) introduced by Bendsøe et. al. in [BGH⁺94]. In [GLS09] this method was also applied to shell structures. In FMO ap-

proaches the components of the elasticity tensor are applied as optimization variables. This usually results in an artificial optimal material tensor. But the transfer of this optimal material to an existing material is a challenging postprocessing step.

3.3.2 Sizing Optimization

Sizing optimization is used to investigate the optimal dimension of cross section parameters, which in detail are related to the applied structural model. The cross section of truss structures is defined by the cross section

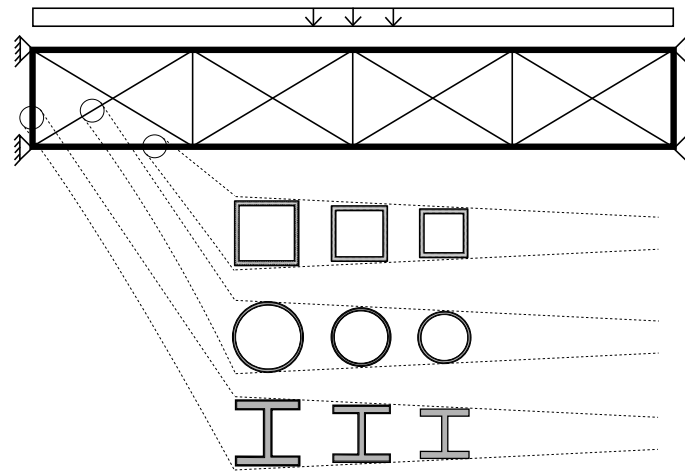


Figure 3.3: Cross section designs of a truss beam structure

area. Beam structures also carry bending loads which requires definition of more complex cross sections, e.g. by width and height or the second moment of inertia. Wall and shell structures usually define their cross section by the thickness. Due to constant model geometry and model topology differentiation of the response function with respect to sizing parameters results in facile and efficient formulations. A simple sizing optimization problem is sketched in figure 3.3. It shows three different cross section types for specific parts of a truss structure with specified geometry and topology. During the sizing optimization process the optimal dimension of each cross section is evaluated. The possible result is a structure with minimal weight that fulfills constraints with respect to maximum displacements and stresses.

3.3.3 Shape Optimization

Shape optimization problems employ the governing geometry variables of a shape parametrization as optimization variables, e.g. nodal coordinates of finite elements, control point coordinates of CAD models or morphing boxes or amplitudes of shape basis vectors. The topology of the structure

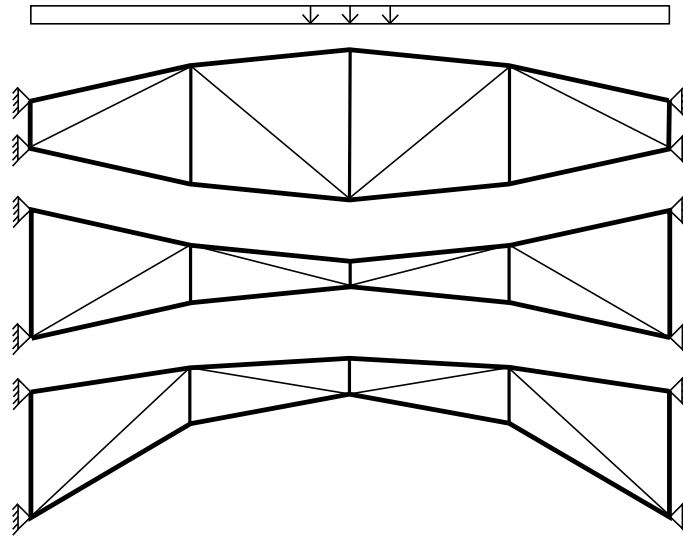


Figure 3.4: Shape designs of a truss beam structure

(connectivity of elements) remains unchanged which prevents the generation of holes. Figure 3.4 motivates a simple shape optimization problem of a truss beam structure. It can be easily observed that the topology (connectivity) of all three designs is equal although the geometry and, therefore, the load carrying behavior changes completely. Formulation of shape derivatives results in complex and time consuming algorithms compared to material or sizing variables whereby algorithmic complexity is strongly related to the applied finite elements. In general, response functions of shape optimization problems are highly non-convex especially for thin and lightweight structures caused by large differences in efficiency of load carrying mechanisms, e.g. load transfer via bending or membrane action. Another source of non-convexity is the interaction of different local design modifications. A famous example are bead optimization problems where a large number of possible bead designs shows nearly equivalent structural properties.

3.3.4 Topology Optimization

The most flexible optimization problem is obtained by application of topology optimization methods. In such problems neither the geometry nor the topology of the structure are predefined. Basic parameters of topology op-

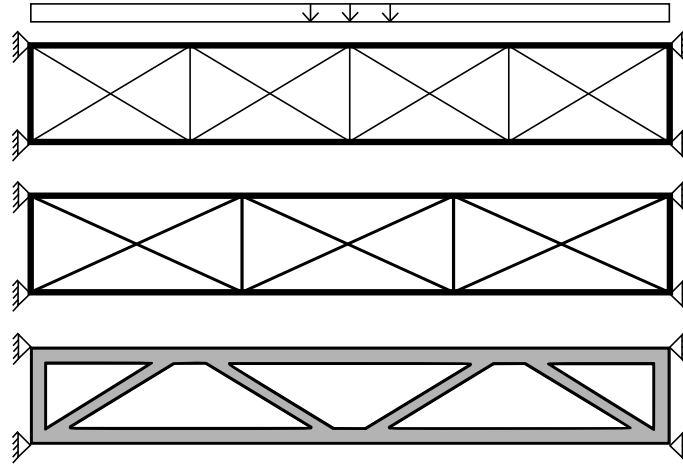


Figure 3.5: Topologies of a truss beam structure

timization problems are the design space and the boundary conditions of the mechanical model. The optimization method computes the most efficient material distribution in the design space. This idea is illustrated by the truss structures in figure 3.5. All three designs are suitable to transfer the load to the supports whereas the material distribution in the design space is totally different.

The most famous topology optimization method is SIMP¹ (c.f. [Ben89]) which establishes a heuristic relation between material properties like Young's modulus and material density. In this approach the density of each single element is specified as independent optimization variable which necessitates application of regularization methods, c.f. chapter 6. Application of SIMP to minimum compliance problems yields to the optimal Michell [Mic04] type structures. The predominant number of applications of topology optimization are related to continuum models discretized by wall or solid elements. An application to shell structures is basically possible, c.f. [Kem04] but these results need serious interpretation.

Many structural optimization problems require a combination of different design variables. Material and sizing parameters are well suited for

¹Solid Isotropic Material with Penalization

a mixed formulation with shape parameters, c.f. [Rei94] whereas combinations with topology optimization methods are much more difficult.

3.4 Response Functions

Objective and constraints specified in equation 3.1 are commonly denoted as response functions. In general, these scalar functions depend on optimization variables \mathbf{s} and state variables \mathbf{u} . Application of gradient based optimization strategies requires differentiability to compute first order and second order gradients, c.f. section 3.2.2. The optimization problems and solution algorithms described here utilize a single objective function only. Optimization problems with several objectives can be solved by multiobjective optimization algorithms, c.f. [EKO90]. Another possibility is a reformulation via summation of the weighted objectives

$$f(\mathbf{s}, \mathbf{u}) = \sum_i^{num_f} w_i \cdot f_i(\mathbf{s}, \mathbf{u}) \quad (3.12)$$

with the single objectives f_i and corresponding weighting factors w_i . It is also possible to reformulate the single functions by the so called Kreisselmeier-Steinhauser (KS) function, c.f. [KS79]

$$f(\mathbf{s}, \mathbf{u}) = -\frac{1}{\rho} \ln \left[\sum_i^{num_f} e^{-\rho \cdot f_i(\mathbf{s}, \mathbf{u})} \right] \quad (3.13)$$

with the parameter ρ controlling the closeness of the KS-function to the smallest objective. The objectives of eigenfrequency or buckling optimization problems are commonly formulated by KS-functions. More detailed information about application of the KS-function is presented in [HG92].

In the following sections several linear and nonlinear response functions and their first order derivatives are described in detail, whereby the terms "linear" and "nonlinear" are related to the underlying mechanical model. Geometrically linear structural mechanics models are used to solve problems with small deformations, which allow to neglect the displacement influence on structural properties like stiffness. Nonlinear models incorporate the nonlinear effect of the displacement field on mechanical properties which allows a more realistic computation of structural response.

3.4.1 Mass

Many structural optimization problems are related to the mass of the structure, either as objective or as constraint. Structural mass m is a function of the design but not a function of the state variables

$$f(\mathbf{s}) = m(\mathbf{s}). \quad (3.14)$$

The first order derivative of the mass with respect to the design variable i can be computed by

$$\frac{df}{ds_i} = \frac{dm}{ds_i}. \quad (3.15)$$

Design variables determining structural mass are usually related to sizing variables, geometry variables and material density. Simple mass optimization problems without further constraints or variable bounds in trivial designs (zero cross section values, zero densities). Application of mass optimization to the shape of a shell or membrane structure with constant thickness permits investigation of the well known minimal surface problems if suitable constraints are defined on the boundaries. Minimal surface problems may also be solved by several other methods:

- Closed analytical formulation which is only possible for specific shapes of the surface boundaries
- Numerical solution applying membrane models [BFLW08], [Wüc07], [Ble90]
- Experimental solution via soap film analogy [OS66]

Figures 3.6 and 3.7 show the initial geometry and the final result of a Scherk like minimal surface. This type of minimal surface was discovered by Heinrich Ferdinand Scherk in 1835. The length, width and height of this special example are all equal. The minimal surface is computed by a mass minimization problem of a shell structure with constant thickness. The optimization converges at the minimal surface without specification of further constraints.

Another famous minimal surface is the catenoid depicted in figure 3.9. The catenoid as minimal surface was discovered by Leonard Euler in 1740. This shape connects two planar circles by the rotation of the catenary curve around the axis specified by the center points of the circles. The initial geometry of the shape optimization problem has a height to radius ratio equal to 1.3158 which is close to the analytical limit of the catenoid surface, c.f. [Lin09].

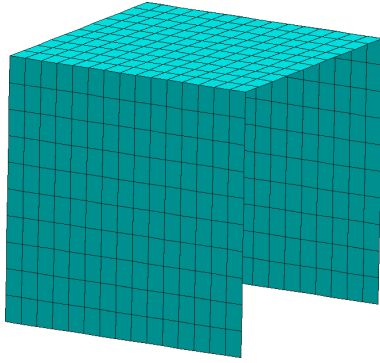


Figure 3.6: Initial Scherk surface

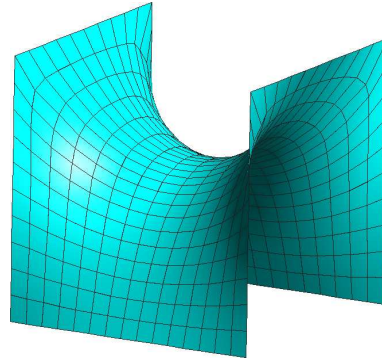


Figure 3.7: Final Scherk surface

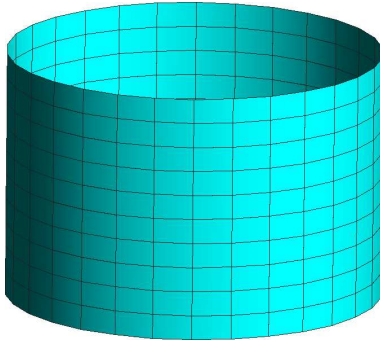


Figure 3.8: Initial catenoid surface

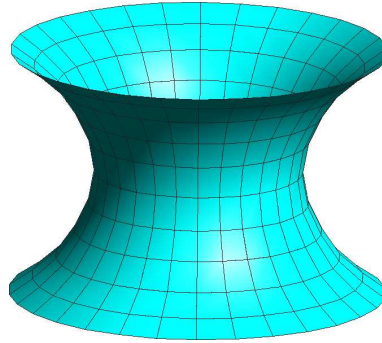


Figure 3.9: Final catenoid surface

3.4.2 Stress

The stress at a specific material point is related to the element strains and the material law according to equation 2.18. In structural optimization the stress is mostly applied as constraint to prevent overstressing of the material at a specific point. Application of stress constraints results in a redistribution of stress peaks to a larger region and therefore to a reduction of maximum stresses.

Often it is necessary to formulate the stress state at a point by a scalar quantity. Therefore equivalence stress hypothesis like the von Mises hypothesis, Tresca hypothesis or Rankine hypothesis are well suited. Subsequently, the von Mises equivalence stress is utilized. It is often applied for ductile materials like steel under static or quasi static loading. The von Mises stress of a three dimensional continuum is specified by

$$\sigma_v = \sqrt{\frac{1}{2} [(\sigma_I - \sigma_{II})^2 + (\sigma_{II} - \sigma_{III})^2 + (\sigma_{III} - \sigma_I)^2]} \quad (3.16)$$

with the principal stresses σ_I , σ_{II} and σ_{III} . It is obvious that a hydrostatic stress state causes a zero von Mises stress whereas deviatoric stress states cause high von Mises stresses.

The stress of a specific material point is a function of design and state variables

$$f(\mathbf{s}, \mathbf{u}) = \sigma_v(\mathbf{s}, \mathbf{u}) \quad (3.17)$$

The stress derivative is formulated by the chain rule

$$\frac{df(\mathbf{s}, \mathbf{u})}{ds_i} = \frac{\partial \sigma_v}{\partial s_i} + \frac{\partial \sigma_v}{\partial \mathbf{u}} \frac{\partial \mathbf{u}}{\partial s_i} \quad (3.18)$$

where $\partial \mathbf{u} / \partial s_i$ denotes the state derivative introduced in section 3.5. From equation 3.18 it follows that the von Mises stress has to be derived with respect to the design variable s_i and the displacement field \mathbf{u} . In the following the derivative of the von Mises stress with respect to the design variable s_i is presented. It applies in the same way to the derivative with respect to the displacements.

$$\begin{aligned} \frac{\partial \sigma_v}{\partial s_i} = & \frac{1}{2\sqrt{\frac{1}{2}[(\sigma_I - \sigma_{II})^2 + (\sigma_{II} - \sigma_{III})^2 + (\sigma_{III} - \sigma_I)^2]}} \\ & \left[2\sigma_I \frac{\partial \sigma_I}{\partial s_i} + 2\sigma_{II} \frac{\partial \sigma_{II}}{\partial s_i} + 2\sigma_{III} \frac{\partial \sigma_{III}}{\partial s_i} - \right. \\ & \left. \sigma_I \left(\frac{\partial \sigma_{II}}{\partial s_i} + \frac{\partial \sigma_{III}}{\partial s_i} \right) - \sigma_{II} \left(\frac{\partial \sigma_I}{\partial s_i} + \frac{\partial \sigma_{III}}{\partial s_i} \right) - \sigma_{III} \left(\frac{\partial \sigma_I}{\partial s_i} + \frac{\partial \sigma_{II}}{\partial s_i} \right) \right] \quad (3.19) \end{aligned}$$

A big challenge in structural optimization problems subjected to stress constraints is the number of active constraints. Usually, more and more stress constraints become active as the design reaches the optimum. Therefore, more and more gradients have to be computed and stored.

One possibility to circumvent this problem is the limitation of the sensitivity analysis to design variables close to the element with an active stress constraint. This idea is motivated by the fact that design modification close to the element with an active stress constraint have a big influence on this stress. Hence, the sensitivity analysis of design variables close to the element results in large gradients compared to design variables far away from this special element. The approximation error of this approach decreases with an increasing number of design variables considered in the sensitivity analysis.

Another possibility to reduce the number of active stress constraints is the formulation of integral stress quantities [Sch05]. In such approaches the

element stresses are integrated over a specific domain. Thus, a single constraint equation controls the stress level of an entire domain. Another benefit of integral stress measures is the improved robustness of the gradients. Stress gradients computed on a single Gauss point are extremely sensitive to design modifications which often cause numerical instabilities. Obviously, an integral stress measure is not as precise as the measurement of the stress at a specific Gauss point. This has to be considered while specification of the limit stress.

3.4.3 Linear Buckling

Linear buckling analysis allows to approximate the failure load of structural systems. The computation of exact critical loads requires a full non-linear analysis which is much more time consuming, c.f. section 3.5.2. The linear pre-buckling analysis provides good failure load approximations for structures with a nearly constant stiffness until failure. In the predominant number of applications the buckling analysis overestimates the real failure load, hence it is in general non-conservative.

The linear pre-buckling problem is based on the solution of the eigenproblem

$$(\mathbf{K} - \lambda \mathbf{K}_g) \boldsymbol{\phi} = \mathbf{0} \quad (3.20)$$

with the linear stiffness \mathbf{K} , the geometric stiffness \mathbf{K}_g , the buckling mode $\boldsymbol{\phi}$ and the inverse of the buckling load multiplier λ . The goal of buckling optimization is mostly the increase of the buckling load $1/\lambda$, which yields to the response function

$$f(\mathbf{s}) = \lambda(\mathbf{s}). \quad (3.21)$$

The computation of the first order derivative of (3.21) is based on a pre-multiplication of equation 3.20 with $\boldsymbol{\phi}^T$. The resulting scalar function f_b

$$f_b(\mathbf{s}, \mathbf{u}, \lambda, \boldsymbol{\phi}) = \boldsymbol{\phi}^T (\mathbf{K} - \lambda \mathbf{K}_g) \boldsymbol{\phi} = 0. \quad (3.22)$$

is used to compute the first order sensitivities. They follow by application of the chain rule of differentiation to

$$\begin{aligned} \frac{df_b}{ds_i} = \boldsymbol{\phi}^T \left(\frac{\partial \mathbf{K}}{\partial s_i} - \lambda \frac{\partial \mathbf{K}_g}{\partial s_i} - \lambda \frac{\partial \mathbf{K}_g}{\partial \mathbf{u}} \frac{\partial \mathbf{u}}{\partial s_i} - \mathbf{K}_g \frac{\partial \lambda}{\partial s_i} \right) \boldsymbol{\phi} + \\ \left(\underbrace{2\boldsymbol{\phi}^T (\mathbf{K} - \lambda \mathbf{K}_g)}_0 \right) \frac{\partial \boldsymbol{\phi}}{\partial s_i} = 0, \quad (3.23) \end{aligned}$$

wherein the displacement derivative of geometric stiffness is often neglected. A normalization of buckling modes such that $\boldsymbol{\phi}_i^T \mathbf{K}_g \boldsymbol{\phi}_i = 1$ allows a reformulation of equation 3.23 to

$$\frac{d\lambda}{ds_i} = \boldsymbol{\phi}^T \left(\frac{\partial \mathbf{K}}{\partial s_i} - \lambda \frac{\partial \mathbf{K}_g}{\partial s_i} \right) \boldsymbol{\phi}, \quad (3.24)$$

which permits a straight forward computation of first order buckling value derivatives. In many buckling optimization problems a whole set of buckling modes has to be optimized. In such cases the objective is formulated by several buckling load factors, e.g. by the Kreisselmeier-Steinhauser function, c.f. page 28. The KS-objective function for a set of i buckling loads is defined by

$$f(\mathbf{s}) = -\frac{1}{\rho} \ln \sum_i e^{-\rho \cdot \lambda_i(\mathbf{s})}. \quad (3.25)$$

The first order derivatives computed by

$$\frac{df}{ds_i} = \frac{1}{\sum_i e^{-\rho \cdot \lambda_i(\mathbf{s})}} \cdot \sum_i \left(e^{-\rho \cdot \lambda_i} \cdot \frac{\partial \lambda_i}{\partial s_i} \right) \quad (3.26)$$

contain the derivatives of the buckling loads computed in (3.24).

Subsequently, a simple buckling optimization example of a quadratic flat plate discretized with shell elements is presented. The boundary conditions are applied according to the well known Euler case 4 where the boundaries perpendicular to the load axis are not supported. The smallest buckling

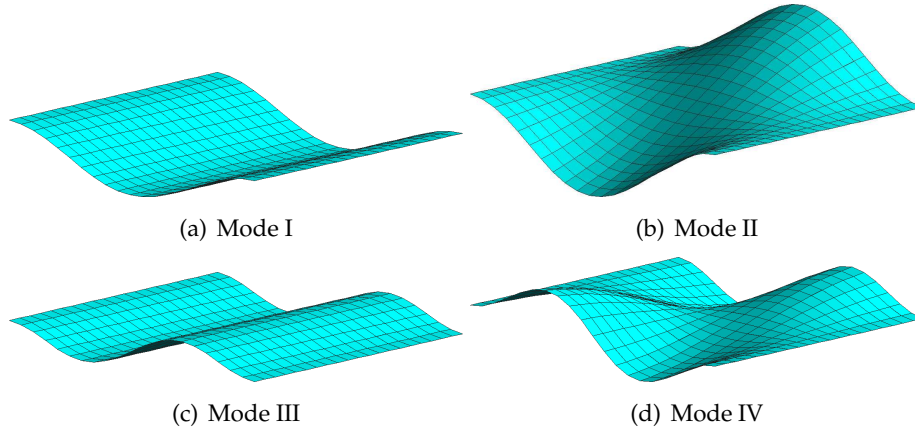


Figure 3.10: Buckling modes of quadratic plate

values of the initial geometry and the corresponding buckling modes are presented in table 3.3 and figure 3.10 respectively. The buckling load factors

are normalized with respect to the value of mode I. It should be noted that the fourth buckling value is 2.66 times larger than the first buckling value.

The goal of the optimization problem is to increase the buckling load, without further constraints. The objective is formulated by a KS-function consisting of the fourth lowest buckling modes. The design variables are the coordinates of the FE-nodes, hence a shape optimization problem is solved. Figure 3.11 shows the optimized geometry after 10 iteration steps of a steepest descent algorithm, c.f. section 4.6.1. It is obvious that this ge-

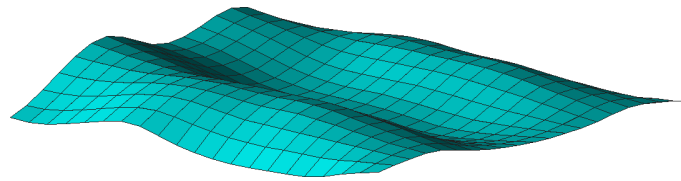


Figure 3.11: Buckling optimized geometry of quadratic plate problem

ometry reacts much stiffer on the modes depicted in figure 3.10. This is substantiated by table 3.3 which compares the initial and the optimized buckling load values. Besides the tremendous increase of buckling loads

Mode numb.	Initial geometry	Optimized geometry
I	1.00	14.84
II	1.58	16.17
III	2.08	17.26
IV	2.66	17.38

Table 3.3: Buckling load factors

the bandwidth of the optimized buckling loads should be mentioned. It is a general property of optimization that the bandwidth of optimized response values is significantly reduced, compared to initial values. Without special care, optimized structures react much more sensitive to imperfections than non-optimized ones.

3.4.4 Eigenfrequency

Eigenfrequency analysis allow to investigate vibration behavior of structures. It is often requested that structural eigenfrequencies do not correspond to loading frequencies, otherwise resonance effects occur. A speci-

fied number of eigenfrequencies are usually computed by solution of the eigenvalue system

$$(\mathbf{K} - \lambda \mathbf{M})\boldsymbol{\phi} = \mathbf{0} \quad (3.27)$$

with the linear stiffness matrix \mathbf{K} the mass matrix \mathbf{M} , the eigenvalues λ and the eigenmodes $\boldsymbol{\phi}$. The eigenvalues of equation 3.27 are related to the eigenfrequencies F by

$$F = \frac{\sqrt{\lambda}}{2\pi}. \quad (3.28)$$

Optimization of eigenfrequency problems is usually related to an increase of the lowest eigenfrequencies or to a maximization of the distance to a target frequency. Therefore, a response function is directly related to an eigenfrequency

$$f(\mathbf{s}) = F(\mathbf{s}). \quad (3.29)$$

Differentiation of this response function by applying the chain rule follows to

$$\frac{f(\mathbf{s})}{ds_i} = \frac{F(\mathbf{s})}{ds_i} = \frac{1}{4\pi\sqrt{\lambda}} \frac{d\lambda}{ds_i}. \quad (3.30)$$

The computation of first order derivatives of the eigenvalues λ with respect to a design variable s_i following the ideas presented in equations 3.21 and 3.22 gives

$$\frac{d\lambda}{ds_i} = \boldsymbol{\phi}^T \left(\frac{\partial \mathbf{K}}{\partial s_i} - \lambda \frac{\partial \mathbf{M}}{\partial s_i} \right) \boldsymbol{\phi}, \quad (3.31)$$

Similar to linear buckling optimization problems also eigenfrequency optimization problems often consider more than one eigenvalue. Hence, the objective may be formulated by a KS-function according to (3.25) with its first order derivative defined in (3.26).

3.4.5 Linear Compliance

The response function of linear compliance or linear strain energy is used to improve structural stiffness. In general, structures optimized with respect to strain energy utilize very efficient load carrying mechanisms. Compliance optimization is often combined with a constraint on structural mass to prevent an increase of stiffness via an increase of mass. Mostly, compact structures have a smaller strain energy than filigree structures. The combination of compliance minimization with a mass constraint is applied extensively for topology optimization problems following Michells theory [Mic04], c.f section 3.3.4.

Linear compliance can be formulated in a discrete form via

$$f(\mathbf{u}, \mathbf{s}) = \frac{1}{2} \mathbf{u}^T \mathbf{K} \mathbf{u}, \quad (3.32)$$

with the linear stiffness \mathbf{K} and the displacement field \mathbf{u} . This formulation of compliance is valid for geometrically linear problems. The first order derivative of (3.32) with respect to a design variable s_i is defined as

$$\frac{df}{ds_i} = \frac{1}{2} \mathbf{u}^T \frac{\partial \mathbf{K}}{\partial s_i} \mathbf{u} + \mathbf{u}^T \mathbf{K} \frac{\partial \mathbf{u}}{\partial s_i}. \quad (3.33)$$

The corresponding state derivative $\partial \mathbf{u} / \partial s_i$ is defined in section 3.5.1. Compliance optimization problems with shape variables are sensitive to finite elements that suffer from locking phenomena, c.f. [Dao05], [Cam04]. In such cases the structure gains stiffness by optimization of locking modes which is obviously a pure numerical effect.

The following example shows a linear compliance optimization of a shell structure. The initial geometry represents a flat quadratic plate of linear elastic material. The structure is Navier supported at the four corner nodes and subjected to dead load acting perpendicular to the initially flat plate. The optimization goal is minimization of compliance (3.32) by variation of vertical nodal coordinates without further constraints. The shell thickness remains constant during the optimization process. It is well known that a

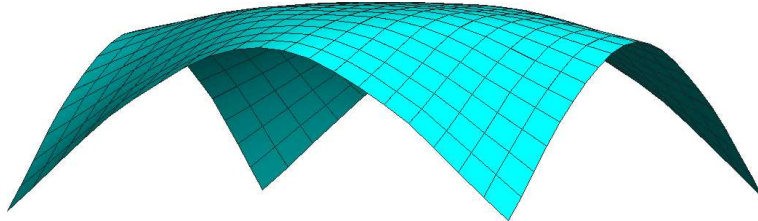


Figure 3.12: Stiffness optimized geometry of linear quadratic plate problem

flat point wise supported shell structure subjected to loads which act normal to the shell surface transfers the loads via bending and transverse shear to the supports. These load carrying mechanisms are much more inefficient than a load transfer via membrane and inplane shear forces. The structure displayed in figure 3.12 works to a large amount by membrane and inplane shear forces and is therefore much stiffer than the flat initial design. This results in smaller displacements and therefore to a much smaller strain energy, c.f. equation 3.32.

The small increase in mass due to the increased surface area of the optimized geometry yields to an increased dead load. This increased load acts like a constraint that prevents designs with an unlimited height. The specified gravitation load and the shell stiffness define an optimal design with a minimal compliance. If the height of the structure is increased above this limit point the increase of load cannot be compensated by an increased stiffness anymore. Thus, the compliance would increase again.

3.4.6 Nonlinear Compliance

Whenever the deformation field has a serious influence on mechanical properties or boundary conditions equation 3.32 cannot be applied for optimizing structural stiffness. In these cases a nonlinear representation of internal energy has to be applied.

Geometrically nonlinear structural problems are characterized by a nonlinear relation between load and displacement, e.g. by the curve depicted in figure 3.13. A numerically sufficient integration of internal energy requires a computation of the full load-displacement curve by very small load increments. It is obvious that this approach is very time consuming. Another drawback of this method is that the load-displacement curve changes completely after application of a design update during optimization. Hence, the full load displacement curve has to be computed again. The tremendous numerical effort of the exact approach motivates an approximation of the internal energy of nonlinear system by a few number of points on the load-displacement curve or by available tangent information. The most simple approximation is depicted in figure 3.13. It approximates the internal energy by the integral of a linear function established between the origin and an arbitrary point on the load-displacement curve characterized by the load f_0 and the corresponding displacement u_0 . The computation of this approximated integral is carried out by the equation

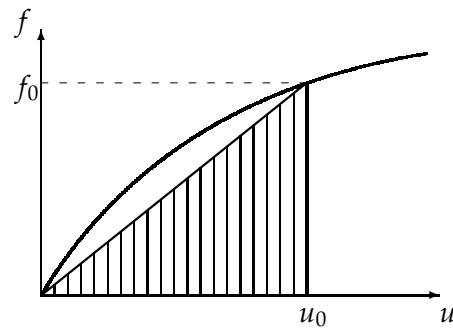


Figure 3.13: Nonlinear load displacement curve

$$f(\mathbf{u}, \mathbf{s}) = \frac{1}{2} (\mathbf{f}_0^{ext})^T \mathbf{u}_0, \quad (3.34)$$

with the external forces of the system \mathbf{f}_0^{ext} . The first order derivative of this response function is defined by

$$\frac{df}{ds_i} = \frac{1}{2} \left(\frac{\partial \mathbf{f}_0^{ext}}{\partial s_i} \right)^T \mathbf{u}_0 + \left(\frac{1}{2} \frac{\partial \mathbf{f}_0^{ext}}{\partial \mathbf{u}} \mathbf{u}_0 + \frac{1}{2} \mathbf{f}_0^{ext} \right)^T \frac{\partial \mathbf{u}}{\partial s_i} \quad (3.35)$$

with the state derivative $\partial \mathbf{u} / \partial s_i$ defined in section 3.5.2. The shape optimization of geometrically nonlinear problems is elaborated in detail in chapter 7.

The following example of nonlinear compliance optimization investigates the structural model specified in section 3.4.5. The only difference is the load which is scaled by a factor of 1000 to obtain a significant displacement field. The goal of the optimization problem is minimization of nonlinear compliance (3.34) by variation of vertical nodal coordinates and constant shell thickness. There are no further constraints applied to the optimization problem. The optimized geometry is depicted in figure 3.14. It shows

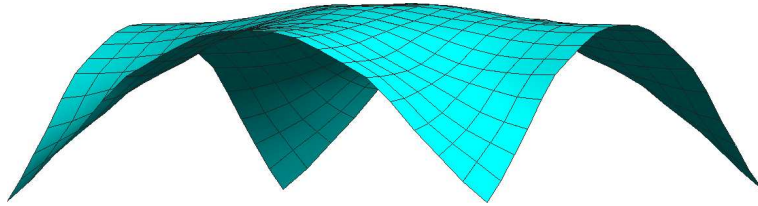


Figure 3.14: Stiffness optimized geometry of nonlinear quadratic plate problem

some significant differences compared to the optimization result of the linear problem, c.f. figure 3.12. Close to the corner nodes and the center of the edges the latter one is only simply curved whereas the nonlinear optimization result is doubly curved. This difference has a tremendous effect on the critical load of the structure which is significantly higher for doubly curved geometries. The differences of linear and nonlinear compliance optimization problems are elaborated in detail in chapter 7 and by the example presented in section 8.2.

The selection of response functions presented in this section is of course not complete. Each function which describes a desired structural property is applicable as response function in an optimization problem. Usually, the response functions have to be evaluated several times during the optimization process. This motivates formulations that allow for numerically efficient evaluation in order to reduce the overall solution time. Application of gradient based optimization strategies additionally requires continuous

differentiability of the response function with respect to the design variables.

3.5 State Derivative

The first order derivative of the state variables (here the displacements \mathbf{u}) with respect to a design variable s_i is denoted as state derivative. The response function derivatives specified in (3.18), (3.33) and (3.35) require the definition of the state derivative $\partial\mathbf{u}/\partial s_i$. In general, the computation of the state derivative depends on the structural model.

3.5.1 Linear State Derivative

The computation of the linear state derivative is based on the equilibrium condition of linear models formulated via

$$\mathbf{r}(\mathbf{u}, \mathbf{s}) = \mathbf{K}(\mathbf{s})\mathbf{u} - \mathbf{f}^{ext}(\mathbf{s}) = \mathbf{0}. \quad (3.36)$$

Differentiation of linear equilibrium with respect to a design variable results in the relation

$$\frac{d\mathbf{r}}{ds_i} = \frac{\partial\mathbf{K}}{\partial s_i}\mathbf{u} - \frac{\partial\mathbf{f}^{ext}}{\partial s_i} + \mathbf{K}\frac{\partial\mathbf{u}}{\partial s_i} = \mathbf{0} \quad (3.37)$$

which can be reformulated to the linear state derivative

$$\frac{\partial\mathbf{u}}{\partial s_i} = \mathbf{K}^{-1} \underbrace{\left(\frac{\partial\mathbf{f}^{ext}}{\partial s_i} - \frac{\partial\mathbf{K}}{\partial s_i}\mathbf{u} \right)}_{\mathbf{f}_{lin}^*}. \quad (3.38)$$

The vector \mathbf{f}_{lin}^* is commonly denoted as pseudo load vector because a system evaluation with this vector as right hand side results in displacement derivatives instead of displacements. The computation of the linear state derivative is necessary for derivatives of response functions related to linear compliance (equation 3.33) and stress (equation 3.18) if a linear mechanical model is used.

3.5.2 Nonlinear State Derivative

The equilibrium of geometrically nonlinear problems cannot be described by equation 3.36 due to the dependency of the stiffness matrix on the displacements. The resulting nonlinear stiffness matrix is denoted as tangential stiffness matrix \mathbf{K}_t . It is defined as the partial derivative of the residual

forces $\mathbf{r}(\mathbf{u}, \mathbf{s})$ with respect to the displacement field \mathbf{u} . The residuum follows from the equilibrium condition

$$\mathbf{r}(\mathbf{u}, \mathbf{s}) = \mathbf{f}^{int}(\mathbf{u}, \mathbf{s}) - \mathbf{f}^{ext}(\mathbf{u}, \mathbf{s}) = \mathbf{0} \quad (3.39)$$

with the internal forces \mathbf{f}^{int} and the external forces \mathbf{f}^{ext} . The equilibrium is fulfilled if the structural displacements and the external load specify a point on the load displacement curve, c.f. figure 3.13. The first order total derivative of (3.39) with respect to the design variables \mathbf{s} is formulated via

$$\frac{d\mathbf{r}}{ds_i} = \frac{\partial \mathbf{f}^{int}}{\partial s_i} + \frac{\partial \mathbf{f}^{int}}{\partial \mathbf{u}} \frac{\partial \mathbf{u}}{\partial s_i} - \left(\frac{\partial \mathbf{f}^{ext}}{\partial s_i} + \frac{\partial \mathbf{f}^{ext}}{\partial \mathbf{u}} \frac{\partial \mathbf{u}}{\partial s_i} \right) = \mathbf{0}. \quad (3.40)$$

This equation can be reformulated to obtain the nonlinear state derivative by

$$\frac{\partial \mathbf{u}}{\partial s_i} = \underbrace{\left(\frac{\partial \mathbf{f}^{int}}{\partial \mathbf{u}} - \frac{\partial \mathbf{f}^{ext}}{\partial \mathbf{u}} \right)^{-1}}_{\mathbf{K}_t} \left(\frac{\partial \mathbf{f}^{ext}}{\partial s_i} - \frac{\partial \mathbf{f}^{int}}{\partial s_i} \right) = \mathbf{K}_t^{-1} \underbrace{\left(\frac{\partial \mathbf{f}^{ext}}{\partial s_i} - \frac{\partial \mathbf{f}^{int}}{\partial s_i} \right)}_{\mathbf{f}_{nl}^*} \quad (3.41)$$

with the tangential stiffness matrix \mathbf{K}_t and the nonlinear pseudo load vector \mathbf{f}_{nl}^* . The nonlinear state derivative formulated in (3.41) is necessary for the derivative of the nonlinear compliance function specified in equation 3.35 and for the derivative of the stress response function (equation 3.18) if the underlying mechanical model is geometrically nonlinear.

3.6 Optimality Criteria

Instead of taking derivatives of response functions and applying mathematical optimization algorithms the Optimality Criteria (OC) methods evaluate a problem specific heuristic criterion to find the optimal design. Hence, OC-methods have to be designed for each specific class of problems. A general application of an optimality criterion is not possible. If an optimality criterion can be found it usually provides a very fast and efficient solution of the problem.

The most likely oldest OC-method is the Fully Stressed Design (FSD) concept. It was originally designed for truss structures and postulates that the structure with the minimal weight is also the structure with the maximum stress in all members. Based on this assumption an iteration algorithm can be designed which converges to the minimal weight design for all statically

determined truss structures. If applied to statically undetermined structures FSD converges to improved but not to optimal designs. Additionally, it is not straight forward to consider constraints, e.g. displacement limits. More information about the fully stressed design concept is presented in [HG92] and [Har08]

Another successful class of OC-methods are the bionic growth rules. These methods are inspired by natural structures like trees, bones or teeth. The designers of bionic growth rules argue that the nature had much time to find the best designs of their structures and that non-optimal designs are eliminated by the evolutionary process. The design update of the bionic growth rule presented in [Mat90] is based on the assumption that optimal shapes exhibit homogeneous surface stresses. Application of this rule to weight minimization problems results in a redistribution of material to highly stressed regions. Bionic growth rules are successfully applied for several types industrial optimization problems.

The Updated Reference Strategy (URS) is designed for the form finding of membrane structures [BR99]. From the optimization point of view it can be considered as OC-method designed for weight minimization of surface structures. The URS postulates that the minimal surface represents the geometry which allows equilibrium of a 2-d isotropic stress field with the boundary. If the full boundary is fixed the value of applied isotropic prestress does not affect the final geometry. The URS is a very efficient approach to solve the problems depicted in figures 3.7 and 3.9. In the last years it was enhanced to consider boundary cables, anisotropic prestress and internal pressure. This allows computation of more realistic membrane structures which are no mathematical minimal surfaces anymore [WB05], [Wüc07], [Lin09]. A detailed introduction to the updated reference strategy and its application as mesh regularization method is presented in chapter 6. Except of the mentioned mesh regularization approach no OC-methods are applied in the optimization problems investigated in this thesis.

Chapter 4

Gradient Based Shape Optimization

This chapter presents a detailed introduction to numerical shape optimization with gradient based optimization strategies. The proposed methods focus on their suitability to large optimization problems. This is necessary because FE-based shape parametrization techniques are investigated which usually yield to huge design spaces. It is shown that efficient sensitivity analysis strategies, first order optimization methods and line search algorithms using polynomial approximations can be combined to highly efficient solution algorithms for constrained and unconstrained optimization problems. FE-based shape parametrization circumvents the crucial problem of proper design space formulations. This chapter is supplemented by chapters 5 and 6 which provide additional information to specific topics of sensitivity analysis and necessary regularization techniques. The proposed methods are efficient, robust and generally applicable.

4.1 Convexity and Uniqueness

Convexity and uniqueness are mathematical terms to describe the curvature of a function and the number of extremum points of this function. A function is denoted as convex if all lines specified between two arbitrary points on the function have no intersection with the function. Hence, the function depicted in figure 4.1 is convex whereas the function in figure 4.2 is non-convex.

The convexity of a response function in structural optimization depends on the type of the function and on the type of variables. Response functions utilized for gradient based shape optimization of large systems are usually highly non-convex. Thus, they exhibit many local minima min_l where one

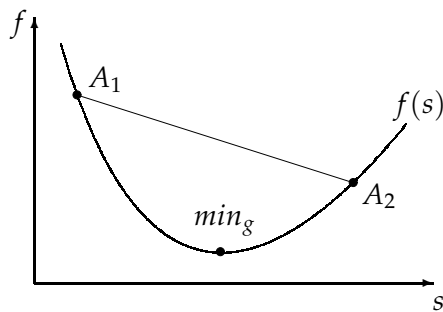


Figure 4.1: Convex function

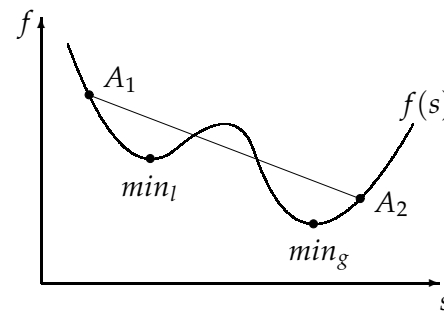


Figure 4.2: Non-convex function

of these is also the global minimum min_g , c.f. figure 4.2.

The convexity of response functions and the uniqueness of optimal results are topics of active discussions in the optimization community. Strictly speaking there is no guarantee that gradient based optimization algorithms find the global optimum min_g . In the predominant number of applications they will just find a local minimum min_l . This motivates developers of zero order methods to emphasize the global convergence behavior of their algorithms. Unfortunately zero order methods are not applicable to large optimization problems, c.f. section 3.2.1.

There exist several methods to reduce the non-convexity of a response function. First of all it is the function definition itself. In many cases integral formulations run much smoother than local discrete parameters. Thus, the desired structural property should be quantified in an integral formulation, if possible. Also, the type of shape parametrization and the number of design variables have a big influence on the convexity of the response function. In general, the number of variables should be reasonable for the actual problem but it should not be needlessly increased. The regularization methods presented in chapter 6 are also well suited to reduce the negative effects of non-convex response functions.

The probably most important approach to influence optimal designs of gradient based optimization methods is the choice of the initial design. Usually, small changes in the initial design provide a good estimation of the robustness of the full optimization model. Especially for shape optimization problems small modifications of the initial design sometimes cause surprising effects. It is well known that the specification of the initial design is a very time consuming part of the modeling procedure. Hence, variations of initial designs are not always performed.

4.2 Shape Parametrization

As denoted in the previous section the type of shape parametrization has a big influence on the solution of the optimization problem. The shape parametrization of a geometry provides the space of possible designs denoted as design space. It is obvious that the optimized geometry is restricted to the chosen design space. Hence, the definition of a small design space limits the optimizer to a small set of geometric variations.

In the predominant number of applications the geometry of an optimization problem is specified by coordinates of a set of control points $\bar{\mathbf{X}}_i$ and the respective shape functions N_i . Thus, the geometry in the reference configuration \mathbf{X} (c.f. figure 2.1) can be formulated by

$$\mathbf{X} = \sum_j N_j \bar{\mathbf{X}}_j. \quad (4.1)$$

The coordinates of the control points are defined as design variables s_i . The different shape parametrization methods described in this section are mainly characterized by the choice of control points and the choice of shape functions.

4.2.1 CAD

Shape parametrization via Computer Aided Design (CAD) methods is well established in industry. The control points of CAD models specify the so called control polygon where the control points are not necessarily interpolated by the final shape. There exist many possibilities to specify the shape functions of CAD models, e.g. polygons, splines, B-splines or Coons patches. Actually, many commercial codes use Non Uniform Rational B-Splines (NURBS) to specify curves, surfaces or volumes. Application of NURBS functions allows for a large variety of geometries with only a small number of parameters, c.f [PT97].

General drawbacks of CAD parametrizations are the time consuming modeling and remodeling steps during optimization which cannot be automated. The remodeling is necessary whenever the optimal geometry cannot be represented by the current parametrization. Another challenge of CAD parametrizations are continuity requirements across patch boundaries which are not easy to ensure.

In general, CAD parametrizations result in a relatively small number of design variables and therefore to a robust optimization problem. More in-

formation about CAD parametrization of shape optimization problems is presented in [Ble90] and [Sch05].

4.2.2 Shape Basis Vectors

Application of shape basis vectors for shape parametrization directly utilizes selected FE-nodes as control points. Hence, there is no need for an additional CAD model. Similar to CAD parametrizations the shape functions can be specified by polygons, splines or B-splines. It is important to specify the full set of shape functions up to the desired degree. Otherwise the geometry representation might not be complete. A characteristic property of shape basis vectors is their definition over the full mesh and not only over the nodes that determine the shape of the structure. Hence, there is no general need to apply mesh regularization algorithms.

The basic drawbacks of shape basis vectors are similar to the drawbacks of CAD parametrizations, namely, the complicated and time consuming modeling and remodeling. Another complicated and time consuming step is the transfer of the optimized FE-mesh into a CAD model for further design or machining. Construction of shape basis vectors and implementation issues are discussed in [Har08].

4.2.3 Morphing

Morphing techniques are another tool to specify general mesh deformations without an underlying CAD model. They are originally designed for image manipulation. Application of morphing as shape parametrization method is based on the separation of the FE-mesh in morphing boxes. In each box a set of control points is specified. The number of morphing boxes with their control point coordinates specify the design space. Shape functions of a desired order are specified by the control points in the morphing box. Similar to shape basis vectors also the shape functions in the morphing boxes are defined over the full mesh. Thus, mesh regularization methods are not absolutely necessary. More information about morphing techniques and the representation in commercial codes is presented in [Har08].

4.2.4 Topography

The shape parametrization techniques specified in previous sections are applicable to 1-D, 2-D surface and 3-D solid geometries. Topography op-

timization is based on a special shape parametrization of plate or shell structures. It is used to optimize bead structures where predefined bead geometries are utilized to define the design update. Thus, the continuous design update specified over the design variables is approximated by the interaction of a set of fixed update functions. A general problem of topography optimization is the high mesh distortion after application of the bead functions. Distorted elements have a serious influence on the quality of the structural response. Additionally, the examples investigated in [Har08] and [Sch05] show a loss of symmetry in initially symmetric problems. Similar to topology optimization the final design has to be carefully interpreted to derive a mechanically useful structure. More information about commercial topography optimization software is presented in [Har08] and [Sch05]. A more theoretical introduction and implementation issues are presented in [Dao05].

4.2.5 FE-based

FE-based shape parametrization provides a maximum size of design space and needs minimal effort during modeling phase. In this approach the nodes and ansatz functions of the FE-mesh are used as design variables and shape functions, respectively. Obviously, it is sufficient to specify the coordinates of those nodes as design variables that influence the geometry. This should be visualized by figure 4.3a which shows a cube discretized with hexahedrons and cutted by the plane A. The coordinates related to surface normal directions n_j with $j \in \{1..N_{nc}\}$ indicate those coordinates that determine the geometry of the cube. The coordinates related to surface tangential planes or interior 3-D directions t_k with $k \in \{1..N_{tc}\}$ define the discretization of the cube but not its geometry. Following the general concept of shape derivatives which was originally formulated by the french mathematician Jaques Hadamard only the variation of coordinates n_j should affect the system response. The derivative of response functions with respect to the coordinates t_k should give zero because these coordinates do not affect the shape. Due to the approximating character of finite elements the indicated derivatives result in spurious values different from zero. This effect is even amplified by incorrect element responses caused by locking phenomena. Finally, the complete optimization result would be seriously affected by deficiencies of the finite elements. Hence, it is much more convenient to specify the optimization variables s_i only from the set of normal coordinates n_j ($s_j \in \{n_1, n_2, \dots, n_{N_{nc}}\}$). The tangential coordinates

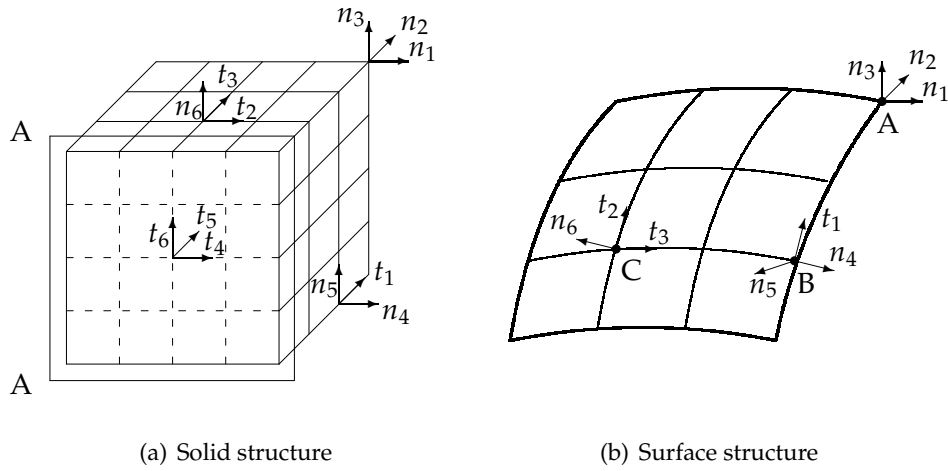


Figure 4.3: Design variables for shape derivatives

t_k are controlled by mesh regularization schemes proposed in chapter 6. In general, this method of separation of nodal coordinates can be applied to all kind of finite element models.

Of course also shell structures allow specification of coordinates that affect the shape and coordinates that just control the discretization. This separation is based on local cartesian coordinate systems established at the element nodes. These coordinate systems define the surface normal and the tangent plane. Thus, one obtains the set of normal coordinates n_j and the set of tangential coordinates t_k which specify geometry of the shell and discretization of the mesh, respectively. To prevent the mentioned ill posed optimization problems the optimization variables s_i are chosen from the set of normal coordinates, $s_i \in \{n_1, n_2, \dots, n_{N_{nc}}\}$. By this definition a vertex node (node A in figure 4.3b) has a maximum number of three optimization variables whereas an edge node (node B in figure 4.3b) has a maximum number of two optimization variables. The inner nodes of a shell structure (node C in figure 4.3b) have only one coordinate which determines the actual geometry. Hence, this normal direction is specified as optimization variable.

Due to the mentioned drawbacks of CAD parametrization, shape basis vectors and morphing the FE-based shape parametrization is utilized for the following derivations and examples. It should be emphasized that application of FE-based shape parametrization requires regularization methods to control the wave length of the response gradients and the mesh quality. These regularization methods are presented in chapter 6. Additionally, ef-

efficient sensitivity analysis methods are required due to the huge number of design variables for large FE-models. In this context adjoint formulations are presented in section 4.3.4.

FE-based parametrization permits the most flexible design spaces that fit optimal to the mechanics of the structural model. This is the basis of high quality shape optimization results with a perfect relation to structural properties.

4.3 Sensitivity Analysis

The term sensitivity describes the effect of an input variation on the output. Knowledge of sensitivities of systems or processes is an important issue in nearly all fields that utilize mathematical models to formulate complex processes, e.g. natural or financial sciences. For shape optimization problems the sensitivity analysis describes the evaluation of derivatives of response functions with respect to design variables. The existing approaches to compute these response gradients are summarized in table 4.4. In the follow-

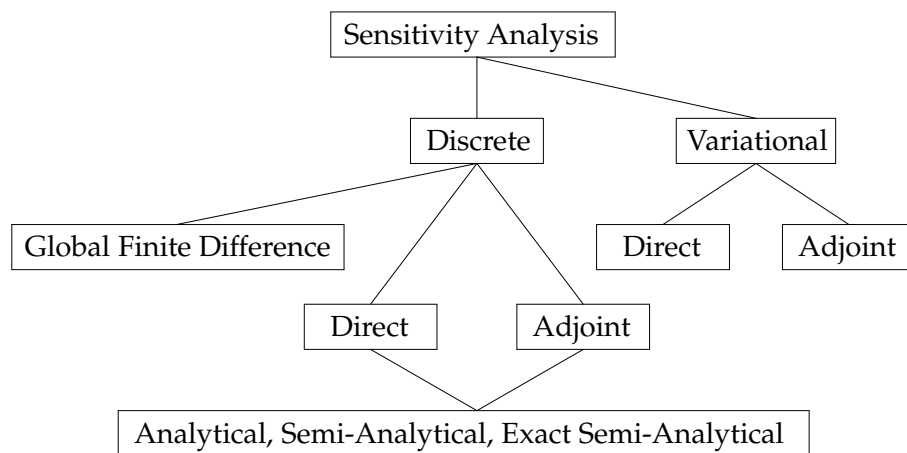


Figure 4.4: Methods for sensitivity analysis

ing sections theory and implementation of the depicted sensitivity analysis methods are compared. They differ significantly with respect to numerical effort and accuracy.

4.3.1 Global Finite Difference

The global finite difference method approximates the derivative of a response function by a finite difference formulation. In many cases a simple forward finite difference step is applied

$$\frac{\partial f}{\partial s_i} \approx \frac{f(\mathbf{u}, \mathbf{s} + \Delta s_i) - f(\mathbf{u}, \mathbf{s})}{\Delta s_i} \quad (4.2)$$

where $\mathbf{s} + \Delta s_i$ specifies the disturbance of the structure in direction of variable s_i . Global finite difference approximations of response derivatives can be implemented very easy even for response functions which do not permit analytic differentiation. The basic drawbacks of this method are the tremendous numerical effort and the approximation error. Equation 4.2 requires two complete function evaluations for the approximation of one derivative. Mostly, each function evaluation corresponds to the solution of an equation system. In general $n + 1$ system evaluations are necessary to compute the derivatives of n design variables by first order finite difference approximations. Thus, sensitivity analysis by global finite differences is very time consuming and, therefore, only applicable for a few number of design variables.

4.3.2 Variational vs. Discrete

In contrast to the global finite difference approach variational and further discrete sensitivity analysis methods utilize analytical derivatives. The basic difference between these methods is the sequence of discretization and differentiation. In the variational approach the continuous formulation of the governing equations are derived and then discretized. The basic goal of variational sensitivity analysis is the formulation of a pseudo load vector. Application of this vector as right hand side of a standard finite element problem allows for computation of the state derivative, c.f. section 3.5. Thus, the sensitivity analysis can be performed without modifications of existing FE-codes. Variational formulations also permit adjoint sensitivity analysis which has great advantages for optimization problems with a large number of design variables and a small number of response functions, c.f. section 4.3.4. Variational sensitivity analysis is a convenient approach in combination with existing FE-codes. The basic drawback is the poor flexibility and the problem that the pseudo load vector has to be derived and implemented separately for each mechanical problem. More information

about variational sensitivity analysis is presented in [HG92], [Cam04] and [Dao05].

The discrete sensitivity analysis is based on a differentiation of the discretized governing equations. Thus, discrete methods need more information from finite element codes, e.g. the state variables, the stiffness matrix or external forces. For several response functions these additional information can be used to derive very efficient formulations for the sensitivities. Due to these benefits and the existing access to all types of finite element data the discrete sensitivity analysis is used in the following.

4.3.3 Direct Sensitivity Analysis

According to figure 4.4 variational and discrete sensitivity analysis can be derived in the direct and the adjoint formulation. The direct approach is based on an explicit evaluation of the state derivative for each design variable, c.f. equations 3.38 and 3.41. It should be noted that the state derivative is independent of the response function. It just depends on the mechanical model and the actual design variable. The computation of n state derivatives for n design variables by the direct approach needs the solution of n systems of equations. Additionally, n state derivatives have to be stored. The direct approach is beneficial when the stored state derivatives are applied in many response functions. In detail the numerical effort compared to the adjoint approach is smaller when the number of design variables is smaller than the number of response functions. For shape optimization problems with FE-based parametrization this is almost never the case. These problems are usually characterized by a huge number of design variables and a small number of response functions. Thus, the direct sensitivity analysis is not applicable to these problems due to the tremendous numerical effort and the memory requirements.

4.3.4 Adjoint Sensitivity Analysis

The adjoint formulation of the sensitivity analysis is numerically much more efficient for problems with a large number of design variables and a small number of response functions. In general, it requires the solution of n systems of equations for the derivative of n response functions. This should be illustrated by two examples where the first one is related to a defined target displacement of a single node. It is assumed that the mechanical model is described by the nonlinear equilibrium equation, c.f. equation

3.39. The response function is specified by the minimization of the nodal displacement

$$f(\mathbf{s}, \mathbf{u}) = u_t \rightarrow \min. \quad (4.3)$$

Computing the derivative with respect to a design variable s_i gives

$$\frac{df}{ds_i} = \frac{\partial f}{\partial s_i} + \left(\frac{\partial f}{\partial \mathbf{u}} \right)^T \frac{\partial \mathbf{u}}{\partial s_i} = \left(\frac{\partial f}{\partial \mathbf{u}} \right)^T \frac{\partial \mathbf{u}}{\partial s_i} \quad (4.4)$$

where $\partial f / \partial s_i$ is equal to zero in this special example. Using the nonlinear state derivative specified in (3.41) allows for the formulation of the direct derivative

$$\frac{df}{ds_i} = \left(\frac{\partial f}{\partial \mathbf{u}} \right)^T \mathbf{K}_t^{-1} \mathbf{f}_{nl n}^*. \quad (4.5)$$

with the tangential stiffness \mathbf{K}_t and the nonlinear pseudo load $\mathbf{f}_{nl n}^*$. Instead of solving the system of equations for the nonlinear pseudo load the formulation can be modified such that the equation system is solved for the displacement derivative of the objective. Thus, the equation system has to be solved only once and not for each pseudo load vector. Exploiting the symmetry of the tangential stiffness the resulting adjoint derivative is specified by

$$\frac{df}{ds_i} = \underbrace{\left(\mathbf{K}_t^{-1} \frac{\partial f}{\partial \mathbf{u}} \right)^T}_{\lambda^T} \mathbf{f}_{nl n}^*. \quad (4.6)$$

Hence, the sensitivity analysis for the simple displacement function can be performed by evaluation of a scalar product between the adjoint variable λ and the pseudo load vector $\mathbf{f}_{nl n}^*$.

The reformulation of (4.5) to (4.6) requires symmetry of the tangential stiffness matrix. This requirement is fulfilled for weak forms (c.f. equation 2.24) that are symmetric bilinear forms ([BS94]) which is the case when test functions are similar to shape functions. This approximation method is commonly denoted as Bubnov-Galerkin method. Discretization of these weak forms yields to so called self adjoint operators which can be formulated in a symmetric matrix.

In a second example the adjoint sensitivity analysis of the linear compliance (3.32) is presented. Substituting the linear state derivative (3.38) in the linear compliance derivative (3.33) gives

$$\frac{df}{ds_i} = \frac{1}{2} \mathbf{u}^T \frac{\partial \mathbf{K}}{\partial s_i} \mathbf{u} + (\mathbf{K} \mathbf{u}) \mathbf{K}^{-1} \mathbf{f}_{lin}^*. \quad (4.7)$$

Once again the symmetry of the stiffness matrix allows a reformulation

$$\frac{df}{ds_i} = \frac{1}{2} \mathbf{u}^T \frac{\partial \mathbf{K}}{\partial s_i} \mathbf{u} + \mathbf{u}^T \underbrace{\mathbf{K} \mathbf{K}^{-1}}_{\mathbf{I}} \mathbf{f}_{lin}^* \quad (4.8)$$

Substitution of the linear pseudo load by the explicit formulation (equation 3.38) allows a further modification to

$$\frac{df}{ds_i} = -\frac{1}{2} \mathbf{u}^T \frac{\partial \mathbf{K}}{\partial s_i} \mathbf{u} + \mathbf{u}^T \frac{\partial \mathbf{f}^{ext}}{\partial s_i}. \quad (4.9)$$

It can be observed that the derivative of the linear compliance formulated in equation 4.9 does not require any global operation. The whole analysis is done by element data which allows for extremely fast algorithms.

The presented examples substantiate the benefits of adjoint sensitivity analysis compared to direct sensitivity analysis. The adjoint formulations allow a much faster computation and require only a small amount of memory. Thus, all the examples presented here utilize adjoint formulations for sensitivity computation.

The following two sections investigate the derivatives of element data with respect to the design variables. Usually, the adjoint formulations permit an element wise computation of the gradients. Therefore, element data like stiffness matrix, load vectors or stresses have to be derived.

4.3.5 Analytical Sensitivity Analysis

The analytical sensitivity analysis is based on exact analytical differentiation of element quantities. The analytical derivative of a linear stiffness matrix is used to present the basic procedure. Usually a stiffness matrix can be expressed by

$$\mathbf{K} = \int_{V_i} \mathbf{B}^T \mathbf{D} \mathbf{B} |\mathbf{J}| dV_i \quad (4.10)$$

with the B-operator \mathbf{B} , the material matrix \mathbf{D} , the determinant of the Jacobian $|\mathbf{J}|$ and the domain for the numerical integration V_i . The analytical derivative of this equation with respect to a shape variable is found by application of the product rule

$$\begin{aligned} \frac{\partial \mathbf{K}}{\partial s_i} = & \int_{V_i} \left(\frac{\partial \mathbf{B}}{\partial s_i} \right)^T \mathbf{D} \mathbf{B} |\mathbf{J}| dV_i + \int_{V_i} \mathbf{B}^T \frac{\partial \mathbf{D}}{\partial s_i} \mathbf{B} |\mathbf{J}| dV_i + \\ & \int_{V_i} \mathbf{B}^T \mathbf{D} \frac{\partial \mathbf{B}}{\partial s_i} |\mathbf{J}| dV_i + \int_{V_i} \mathbf{B}^T \mathbf{D} \mathbf{B} \frac{\partial |\mathbf{J}|}{\partial s_i} dV_i. \end{aligned} \quad (4.11)$$

The constant element integration domain V_i does not give a derivative with respect to the design variables.

In case of sizing optimization the derivatives are much simpler because B-operator and mostly also the material matrix do not depend on sizing variables. It is obvious that implementation of equation 4.11 gives lengthy and relatively complicated element routines. Due to the serious numerical effort of dense matrix products the computation of analytical shape derivatives needs significantly more time compared to the computation of a standard stiffness matrix, c.f. [Kim90]. The derivation of analytical derivatives of element data requires a deep knowledge of the element formulation, especially for complicated elements like nonlinear shells with EAS and ANS extensions. The complexity of these formulations and the significant numerical effort motivate the approximation of analytical derivatives by finite differences which can be applied to any formulation in a black-box kind of standard application..

4.3.6 Semi-Analytical Sensitivity Analysis

The substitution of analytical derivatives by finite differences should overcome the basic drawbacks of analytical sensitivity analysis, namely the complicated formulations that prevent a sensitivity analysis if the element routines are inaccessible. Also the semi-analytical approach is introduced at the example of the linear stiffness matrix. The analytical derivative defined in (4.11) can be approximated by a first order equation

$$\frac{\partial \mathbf{K}}{\partial s_i} \approx \frac{\mathbf{K}(\mathbf{u}, s_i + \Delta s) - \mathbf{K}(\mathbf{u}, s_i)}{\Delta s} \quad (4.12)$$

or a second order equation

$$\frac{\partial \mathbf{K}}{\partial s_i} \approx \frac{\mathbf{K}(\mathbf{u}, s_i + \Delta s) - \mathbf{K}(\mathbf{u}, s_i - \Delta s)}{2\Delta s} \quad (4.13)$$

where the terms first order and second order are related to the decrease of the approximation error for decreasing perturbations Δs . The basic benefit of semi-analytical sensitivity analysis is the small programming effort and the predictable numerical effort. It is obvious that a stiffness derivative needs approximately twice the time of a standard stiffness evaluation. Another advantage is that existing element routines do not have to be modified.

The drawback of each finite difference method are approximation errors and round-of errors. The derivative suffers from approximation errors

whenever the perturbation Δs is too large. If the perturbation is too small round-off errors disturb the result. Usually, the range of suitable perturbations has to be investigated for each application.

Application of finite difference methods to derivatives of element data shows a very specific type of approximation error. This error is related to the rigid body rotation vectors of the elements where elements with higher order shape functions like Bernoulli beams and Kirchhoff plates behave significantly more sensitive. Chapter 5 presents a method to eliminate this type of approximation errors by an efficient method independent of the specific element formulation. The resulting exact semi-analytical sensitivity analysis permits a robust and efficient approximation of the element derivatives with minimal approximation errors.

4.4 Side Constraints

Side constraints limit the admissible range of design variables, e.g. allowable shell thickness or beam cross sections of sizing optimization problems. Shape optimization problems utilize side constraints to describe the maximum constructed space of the optimal structure. In many applications these constraints are necessary to prevent trivial results, e.g. zero cross sections. In general, side constraints are not treated as "real" constraints in the optimization problem, c.f. equation 3.1. In detail, they do not enter the Lagrangian function (3.2) and the Karush-Kuhn-Tucker conditions (3.3) - (3.5). A reason for this is the simple structure of side constraints that allows for a simplified treatment. Another reason is the huge number of side constraints that are usually defined. In many problems each variable has an upper and a lower side constraint. In these cases the number of constraints would be at least two times the number of variables which would end in a very expensive solution process. Thus, the side constraints are treated for each optimization algorithm in a specific manner. The implementation in MMA methods is presented in [Dao05].

Following the idea of "move limits", first order gradient methods like Conjugate Gradient (section 4.6.2), Feasible Direction (section 4.7.1) or Augmented Lagrange (section 4.7.2) allow the abidance of side constraints by limitations in the design update step. This approach is simple, very efficient and robust for moderate design update steps which are necessary for constrained optimization problems anyway.

The basic procedure of this approach is visualized in figure 4.5. It shows a

simplified shape optimization problem with the geometry at iteration step i characterized by the points N_1 , N_2 and N_3 .

The depicted geometrical constraint is treated as side constraint of the design variables formulated at the points N_1 , N_2 and N_3 . It may result from limitations of the constructed space. The application of the pure design update ΔX yields to the geometry depicted by the dashed line. Obviously it violates the constraint near point n_2 . Therefore the design update is modified

such that the point n_2 is placed directly on the boundary of the constraint. The resulting geometry described by the points n_1 , n_2 and n_3 is feasible and can be used to compute the design update of the next iteration step $i + 1$. This general concept is usually denoted as trust region concept.

The following example visualizes the introduced procedure by the catenoid problem presented in section 3.4.1 where the initial catenoid design has a radius equal to 0.5. It is enhanced by a cylinder with the radius equal to 0.4 representing a geometrical constraint. It is obvious that the optimal solution depicted in figure 3.9 cannot be reached anymore because it would violate the constraint. The constrained optimum shown in figure 4.7 touches

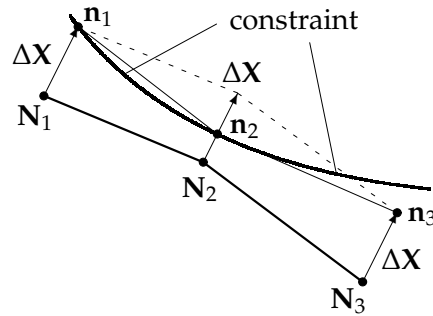


Figure 4.5: Constrained design update

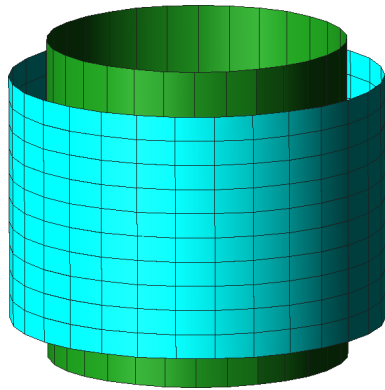


Figure 4.6: Initial catenoid design

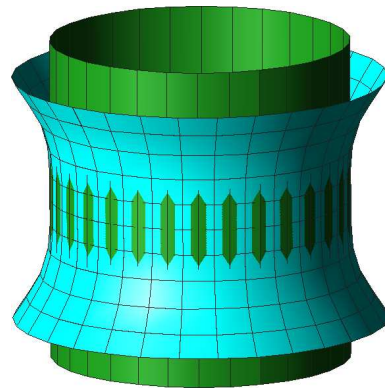


Figure 4.7: Constrained catenoid

the cylinder in the middle of the catenoid. It represents a minimal surface under a geometric constraint. In general, sets of geometrical primitives like cylinders, spheres, boxes, cones and tori are well suited to describe complex

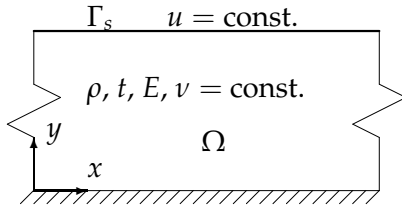


Figure 4.8: 2-d Domain

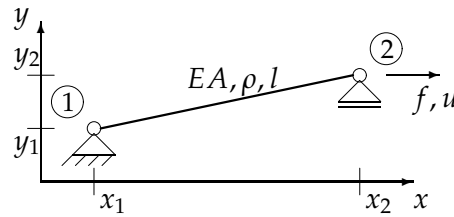


Figure 4.9: 2-d Truss model

limits of constructed spaces. The exact analytical implementations of these primitives allow for fast and exact algorithms to treat these constraints as side constraints of the optimization problem.

4.5 Size Effects in Response Gradients

The basic output of each optimization algorithm is the design update which can be interpreted as design velocity with the iteration steps as time steps. Gradient based optimization algorithms utilize derivatives of response functions to compute the design update. Thus, any inaccuracy in the gradient fields also appears in the design update. Due to the non-convexity of the response function the disturbed design update may result in another local minimum. Such local minima are usually inferior to the minima resulting from undisturbed gradients.

The following example investigates an important source of these inaccuracies, namely the parametrization. Figure 4.8 shows a section of a simple two dimensional domain of linear elastic material with constant thickness and density. The lower boundary of this domain is fixed and the upper boundary is subjected to a constant vertical displacement field u . The shape of Ω is determined by the shape of the design boundary Γ_s which is initially a straight line. It is obvious that the derivative for instance of mass (3.15) and compliance (3.33) with respect to vertical coordinates y have to be constant over Γ_s . Variational sensitivity analysis (c.f. section 4.3) gives exactly the desired constant gradient field. Here the derived analytical equations are discretized. Discrete sensitivity analysis methods do not result in constant gradient fields because the derivatives are affected by the parametrization of the domain. This effect appears for analytical as well as semi-analytical derivatives.

The influence of the parametrization on discrete sensitivities is investigated

by a truss and a membrane finite element for shape gradients of mass and compliance. The general procedure applies in the same way to other element types, other types of design variables and other response functions.

Truss model

The truss element depicted in figure 4.9 is defined by extensional stiffness EA , density ρ and length l . The length of the truss is formulated in a general way by

$$l = \sqrt{(x_2 - x_1)^2 + (y_2 - y_1)^2}. \quad (4.14)$$

The model has one degree of freedom namely the x-displacement of node 2. Application of the nodal force f results in the nodal displacement u . In the following, the gradients of structural mass and linear strain energy are investigated with respect to their dependence on the length l of the truss element. It is referred to sections 3.4.1 and 3.4.5 for more information about these response functions. The differentiation is performed with respect to one design variable namely the x-coordinate of node 2 denoted by x_2 . The mass of a truss element is defined by

$$m^e = \rho \cdot A \cdot l. \quad (4.15)$$

Substitution of (4.14) in (4.15) and differentiation with respect to the design variable x_2 yields to the gradient of structural mass

$$\frac{dm^e}{dx_2} = \rho \cdot A \frac{dl}{dx_2} = \rho \cdot A \frac{x_2 - x_1}{l}. \quad (4.16)$$

It is easy to verify that the value of the mass gradient depends on the length l of the element.

Under the assumption of constant nodal loads the derivative of linear structural strain energy is defined by

$$\frac{dg}{dx_2} = -\frac{1}{2}u \frac{dK}{dx_2}. \quad (4.17)$$

Expressing the truss stiffness by EA/l and substitution of the length derivative specified in (4.16) allows for a specific formulation of the strain energy derivative

$$\frac{dg}{dx_2} = -\frac{1}{2}u \frac{\partial K}{\partial l} \frac{\partial l}{\partial x_2} = -\frac{1}{2}u \left[-\frac{EA}{l^2} \frac{x_2 - x_1}{l} \right] u = \frac{EA(x_2 - x_1)}{2l^3} u^2. \quad (4.18)$$

Obviously, also the gradient of linear strain energy depends on the size of the element. It should be clearly emphasized that the size effect in the two gradients is of different order. Whereas the element length shows up

linearly in the mass derivative it is cubic in the strain energy derivative. Hence, the strain energy gradients are much more affected by element sizes than mass gradients.

Membrane model

For sake of simplicity the investigation of the membrane element is restricted to rectangular flat quadrilaterals. Other shapes would require numerical integration which prevents the presentation of analytic formulas.

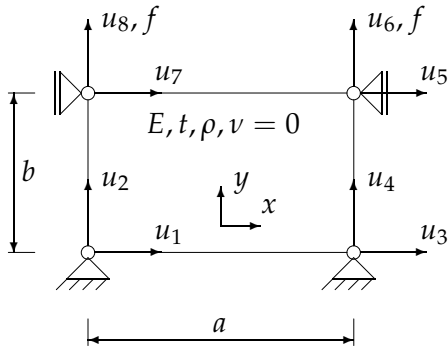


Figure 4.10: Wall model

The wall element depicted in figure 4.10 is used subsequently. It is supported such that the only remaining degrees of freedom are the nodal displacements u_6 and u_8 . Each of these dofs is subjected to a constant nodal load f such that $u_6 = u_8$. The kinematic relation is established by a linear elastic material with Poisson's ratio $\nu = 0$. Similar to the truss model the gradients of element mass and linear strain energy were

computed. The differentiation is performed with respect to the element height b which serves as design variable.

The mass of the applied rectangular wall element is defined as

$$m^e = \rho \cdot a \cdot b \cdot t. \quad (4.19)$$

Differentiation with respect to the element height b yields to the result

$$\frac{dm^e}{db} = \rho \cdot a \cdot t, \quad (4.20)$$

which still contains the element width a . Thus, the presented mass derivative of a rectangular wall element depends linearly on the element size.

Due to the supports the stiffness matrix of the wall element is reduced to a 2x2 matrix defined as

$$\mathbf{K} = \begin{bmatrix} K_{66} & K_{68} \\ K_{86} & K_{88} \end{bmatrix} \quad (4.21)$$

with the components

$$K_{66} = K_{88} = \frac{Et}{12} \left(\frac{4a}{b} + \frac{2b}{a} \right) \quad \text{and} \quad K_{68} = K_{86} = \frac{Et}{12} \left(\frac{2a}{b} - \frac{2b}{a} \right), \quad (4.22)$$

c.f. [Wer01]. Differentiation of linear strain energy requires the stiffness matrix derivative which are specified by the components

$$\frac{dK_{66}}{db} = \frac{dK_{88}}{db} = \frac{Et}{12} \left(-\frac{4a}{b^2} + \frac{2}{a} \right) \quad \text{and} \quad \frac{dK_{68}}{db} = \frac{dK_{86}}{db} = \frac{Et}{12} \left(-\frac{2a}{b^2} - \frac{2}{a} \right). \quad (4.23)$$

Computation of the strain energy derivative by equation 4.9 results in the relation

$$\frac{dg}{db} = -\frac{1}{2} \begin{bmatrix} u_6 \\ u_8 \end{bmatrix}^T \begin{bmatrix} \frac{\partial K_{66}}{\partial b} & \frac{\partial K_{68}}{\partial b} \\ \frac{\partial K_{86}}{\partial b} & \frac{\partial K_{88}}{\partial b} \end{bmatrix} \begin{bmatrix} u_6 \\ u_8 \end{bmatrix}. \quad (4.24)$$

A constant nodal load does not have a shape derivative. Therefore, the external load term of equation 4.9 does not appear in (4.24). Substitution of (4.23) in (4.24) and taking into account that $u_6 = u_8 = u$ the above equation can be simplified to

$$\frac{dg}{db} = \frac{Eta}{2b^2} u^2. \quad (4.25)$$

It is easy to verify that also the presented shape derivative of a wall element suffers from element size effects. In this case the derivative increases linearly with an increasing element width a . In contrast to that the derivative decreases quadratically with an increasing element height b .

In general gradient fields of each parametrization suffer from size effects. For complicated element formulations and parametrizations these effects are complex and hard to identify. They depend

- on the type of parametrization (CAD, Morphing, FE-based, ...),
- on the type of finite element,
- on the type of design variable and
- on the type of response function.

The above statements are illustrated by several numerical experiments. Therefore the 2-d domain depicted in figure 4.8 is discretized by three different meshes shown in figure 4.11. These discretizations are applied to

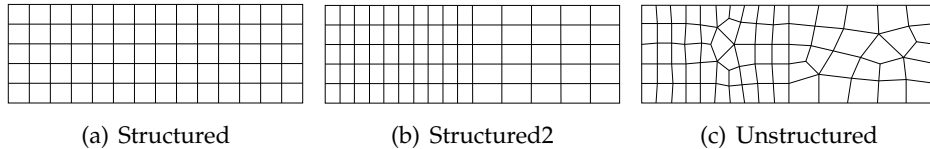


Figure 4.11: Discretizations of 2-d Domain

compute the shape gradient on the boundary Γ_s for structural mass and linear strain energy. The y-coordinates of the FE-nodes on Γ_s are chosen as design variables. The graphs in figure 4.12 and 4.13 show the normalized

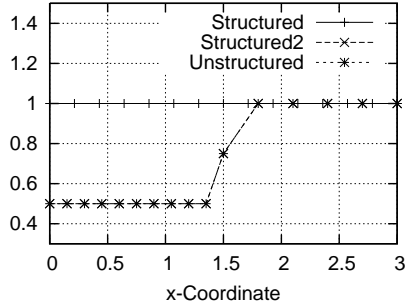


Figure 4.12: Mass gradients

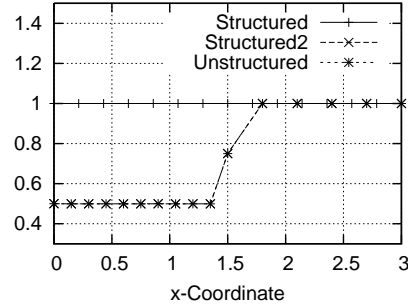


Figure 4.13: Strain energy gradients

mass gradients and the strain energy gradients on Γ_s . It is obvious that the discretization has a tremendous influence on the gradients. The only graph that shows the desired constant behavior belongs to the discretization depicted in figure 4.11a. The other two graphs show a serious influence due to the different element sizes. In this special example the size effect is restricted to the width of the elements at the boundary Γ_s . Hence the graphs of the discretizations depicted in figure 4.11b and 4.11c are equal. These investigations show that the influence of different parametrizations has to be considered carefully in optimization algorithms. In the following, three different remedies were motivated:

1. Securing of good mesh quality.
2. Application of curvature information.
3. Gradient scaling by dual shape functions.

A good mesh quality is the simplest way to reduce the disturbing influence of size effects for FE-based parametrizations. In detail it is necessary to ensure

- nearly equal element sizes,
- best possible aspect ratios,
- symmetric discretizations of symmetric geometries.

CAD or morphing parametrizations require a nearly equal size of CAD elements and morphing boxes respectively. Additionally, the number of finite elements in each parametrization object should be nearly equal.

A well known way to include a proper variable scaling in optimization algorithms is the application of Newton or quasi Newton methods. These methods compute the search direction by

$$\mathbf{s}_d^{(k)} = -\mathbf{H}^{-1}\nabla f^{(k)}. \quad (4.26)$$

where \mathbf{H} denotes the exact or approximated Hessian matrix containing the second order derivatives. The curvature of the response function at the design $\mathbf{s}^{(k)}$ allows for proper scaling of the gradients and highly efficient search directions.

Following the main ideas of variational sensitivity analysis motivates the application of dual element basis functions to compute proper gradient scaling factors. As mentioned earlier, the variational sensitivity analysis does not show size effects in the gradients. Since the equations were discretized after differentiation the respective nodal values represent the sampling points of a distributed sensitivity field. Discrete Sensitivities of response functions with respect to coordinates of FE-nodes represent consistent nodal values of this sensitivity field but not the sampling points. Thus, the goal is to compute the unknown distributed sensitivity field from known nodal values. The dual basis functions of finite elements allow for the computation of distributed quantities from consistent nodal values. They are able to reconstruct e.g. surface loads from consistent nodal forces of this load. This provides a promising basis for the efficient derivation of gradient scaling factors. Then, the scaled gradients do not include disturbing discretization effects and ensure computations of efficient search directions without the necessity of second order information.

4.6 Unconstrained Optimization Algorithms

In general optimization algorithms are separated according to their suitability to constrained optimization problems. Unconstrained optimization algorithms can only be applied to unconstrained optimization problems. In this class of problems neither inequality constraints nor equality constraints are defined, c.f. equation 3.1. But side constraints can be considered by most unconstrained optimization algorithms by simple modifications.

Unconstrained optimization strategies compute for the current optimization step k a design update $\mathbf{d}^{(k)}$ based on the objective gradient $\nabla f^{(k)}$ which is defined by

$$\nabla f^{(k)} = \frac{df(\mathbf{s}^{(k)})}{d\mathbf{s}} \quad (4.27)$$

with the actual design \mathbf{s}^k . The design update is computed by scaling of the search direction \mathbf{s}_d with the step length parameter α , c.f. section 4.8

$$\mathbf{d}^{(k)} = \alpha^{(k)} \mathbf{s}_d^{(k)} (\nabla f^{(k)}). \quad (4.28)$$

The method how to compute the search direction is specific for each optimization algorithm. Unconstrained optimization algorithms are seldomly applied in practical applications because most of the optimization problems contain constraints. But the ideas of unconstrained methods are utilized in many sophisticated constrained optimization algorithms.

4.6.1 Method of Steepest Descent

The most simple unconstrained optimization algorithm is the method of Steepest Descent (SD). It computes the search direction at step k by

$$\mathbf{s}_d^{(k)} = -\nabla f^{(k)}. \quad (4.29)$$

Thus, it is always ensured that the objective can be improved. The basic drawback of the SD method is bad convergence if the curvature of the objective with respect to the design variables differ seriously. This ends up in the well known zigzagging behavior and slow convergence rate. Variable scaling is a simple and efficient approach to prevent these convergence problems. The method of steepest descent can be extended to the Constraint Steepest Descent (CSD) method which is applicable to constrained optimization problems, c.f. [Aro04]. The general steepest descent optimization algorithm is depicted in figure 4.14.

4.6.2 Method of Conjugate Gradients

Application of the Conjugate Gradient (CG) algorithm is also a method to improve the convergence rate of the steepest descent approach. The search direction of the CG method incorporates the curvature of the objective by the parameter β such that

$$\mathbf{s}_d^{(k)} = -\nabla f^{(k)} + \beta \mathbf{s}_d^{(k-1)}. \quad (4.30)$$

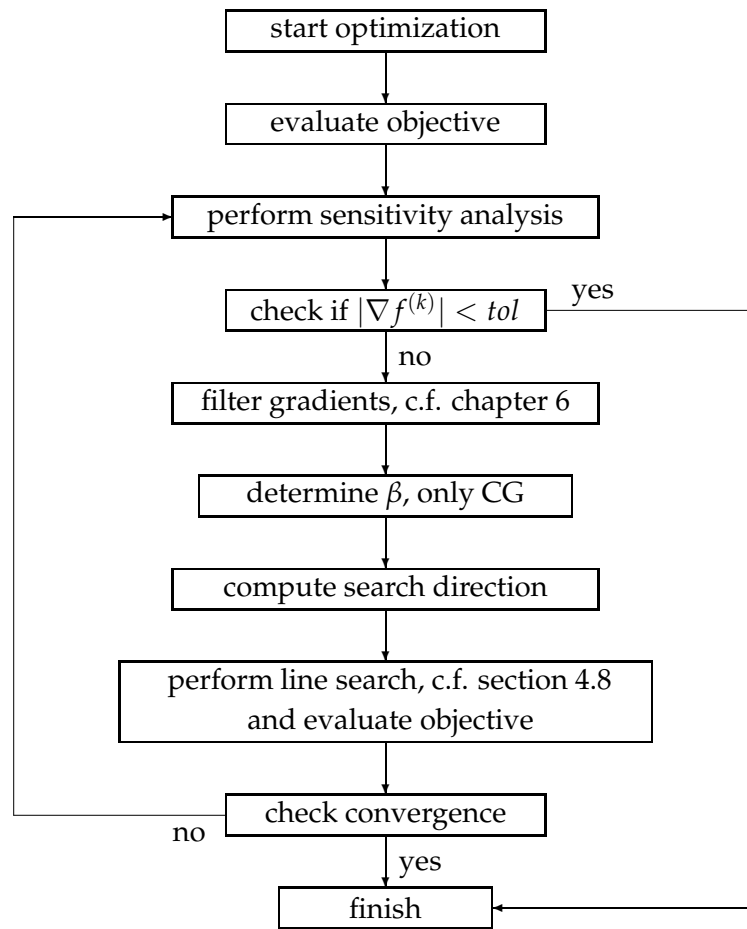


Figure 4.14: CG / SD optimization algorithm

The parameter β can be computed by the current and the previous objective gradients

$$\beta = \frac{\nabla f^{(k)} \cdot \nabla f^{(k)}}{\nabla f^{(k-1)} \cdot \nabla f^{(k-1)}}. \quad (4.31)$$

For most optimization problems the CG method shows a faster convergence than the steepest descent method. In general, the faster convergence preponderates the increased numerical effort of computation of β and the storage of the old search direction $\mathbf{s}_d^{(k-1)}$ and turns out to be numerically more efficient.

The basic implementation of the Steepest Descent and the Conjugate Gradient method is illustrated in figure 4.14. The algorithm is converged if the maximum number of iterations is reached or if the L_2 norm of the gradient vector is smaller than a specified tolerance tol .

4.7 Constrained Optimization Strategies

4.7.1 Method of Feasible Directions

Methods of Feasible Directions [Zou60] are direct methods of first order. In general, they do not require evaluation of Lagrange multipliers. The Method of Feasible Direction (MFD) computes a search direction such that the next design is feasible

$$\mathbf{s}_d^{(k)} \cdot \nabla g_i(\mathbf{s}^{(k)}) \leq 0 \quad (4.32)$$

and usable

$$\mathbf{s}_d^{(k)} \cdot \nabla f(\mathbf{s}^{(k)}) \leq 0. \quad (4.33)$$

The optimization problem is converged if one of these conditions can not be fulfilled. Conditions 4.32 and 4.33 are visualized in figure 4.15.

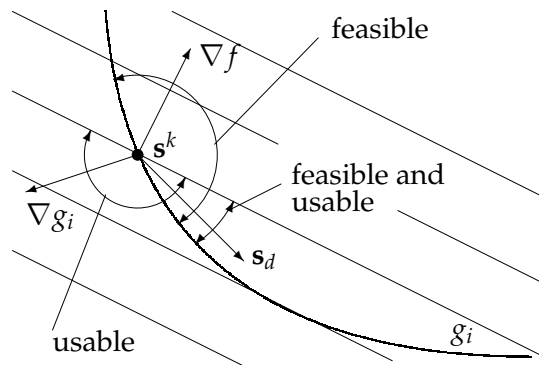


Figure 4.15: Method of Feasible Direction

Additionally, equations 4.32 and 4.33 require a feasible initial design. This is a serious drawback because in many practical applications feasible designs are not easy to define. However, there exist several methods to compute feasible designs by the method of feasible directions, c.f. [HG92] and [Van84]. The benefit of the method is that all intermediate solutions are feasible. Thus, the optimization procedure can be terminated at each step. In any case one obtains a feasible and improved design from the optimizer. There exist many publications about improvements of feasible direction methods regarding robustness (e.g. [SS93]), treatment of infeasible initial designs (e.g. [PTM77]) and improvement of convergence (e.g. [KC00]). Actual feasible direction methods are very powerful and robust optimization strategies.

Additionally, equations 4.32 and 4.33 require a feasible initial design. This is a serious drawback because in many practical applications feasible designs are not easy to define. However, there exist several methods to compute feasible designs by the method of feasible directions, c.f. [HG92] and [Van84]. The

The determination of the search direction \mathbf{s}_d is usually formulated by the linear problem:

$$\begin{aligned}
\text{Maximize} \quad & \beta & (4.34) \\
\text{such that} \quad & \nabla f(\mathbf{s}^{(k)}) \cdot \mathbf{s}_d + \beta \leq 0, \\
& \nabla g_i(\mathbf{s}^{(k)}) \cdot \mathbf{s}_d + \beta \theta_i \leq 0, & i = \{1, \dots, n_{act}^g\} \\
& -1 \leq s_{d_j} \leq 1 & j = \{1, \dots, n^{dv}\}
\end{aligned}$$

where n_{act}^g and n^{dv} denote the number of active constraints and the number of design variables respectively.

In equation 4.34 the parameter θ_i specifies a push-off factor that controls the angle between the tangent at the constraint g_i and the search direction \mathbf{s}_d . The directions determined by $\theta_i = 0$ and $\theta_i \rightarrow \infty$ describe the tangent on constraint g_i and the tangent on the objective f respectively, c.f. [Van84]. The linear problem specified in (4.34) is usually solved efficiently and fast by the well known Simplex method. Unfortunately, the feasible direction strategy defined so far is not well suited for application to large shape optimization problems with FE-based parametrization. The reasons are:

- Size of linear problem
Usually, the linear problem specified in (4.34) yields to a dense coefficient matrix with the dimension $(n_{act}^g + 1) \times n^{dv}$. Such a matrix requires a huge amount of memory for a large number of design variables and many constraints.
- Inadequate smoothness
As described in chapter 6 the FE-based parametrization requires smooth geometries and, therefore, also smooth search directions \mathbf{s}_d . Here, a smooth search direction specifies a design update that results in a smooth geometry after its application. In this context the term smooth is related to the curvature of the surface geometry. The solution of the above defined linear problem yields to non-smooth search directions because the necessary constraint $\mathbf{s}_d \cdot \mathbf{s}_d \leq 1$ is nonlinear and, therefore, not applicable to the Simplex solver.

The remedy for both problems is based on the idea of Lagrange multipliers (3.2), c.f. [Zou60] and [Van84]. The main idea is the transfer of the linear problem defined in (4.34) to

$$\begin{aligned}
\text{Maximize} \quad & \mathbf{p} \cdot \mathbf{y} & (4.35) \\
\text{such that} \quad & \mathbf{A}\mathbf{y} \leq 0, \\
& \mathbf{y} \cdot \mathbf{y} \leq 1
\end{aligned}$$

established for design $\mathbf{s}^{(k)}$ where

$$\mathbf{y} = \begin{pmatrix} s_{d_1} \\ s_{d_2} \\ \cdot \\ \cdot \\ s_{d_{n^{dv}}} \\ \beta \end{pmatrix}, \quad \mathbf{p} = \begin{pmatrix} 0 \\ 0 \\ \cdot \\ \cdot \\ 0 \\ 1 \end{pmatrix} \quad \text{and} \quad \mathbf{A} = \begin{bmatrix} \nabla^T g_1 & \theta_1 \\ \nabla^T g_2 & \theta_2 \\ \cdot & \cdot \\ \cdot & \cdot \\ \nabla^T g_{n^{act}} & \theta_{n^{act}} \\ \nabla^T f & 1 \end{bmatrix} \quad (4.36)$$

This nonlinear problem is equivalent to the linear problem stated as

$$\mathbf{B}\mathbf{u} + \mathbf{v} = \mathbf{c} \quad (4.37)$$

with $\mathbf{B} = -\mathbf{A}\mathbf{A}^T$, $\mathbf{c} = -\mathbf{A}\mathbf{p}$ and the initial solution $\mathbf{v} = \mathbf{c}$ and $\mathbf{u} = \mathbf{0}$. The desired search direction follows finally by

$$\mathbf{y} = \mathbf{p} - \mathbf{A}^T \mathbf{u}. \quad (4.38)$$

The solution of (4.37) instead of (4.34) is much more efficient and the computed search direction is much more reliable. The benefit in efficiency is related to the coefficient matrix \mathbf{B} which is significantly smaller than the matrix \mathbf{A} which is used in problem 4.35. The search direction is more reliable because it is based on a linear combination of objective gradient and constraint gradients. Whenever all considered gradients fulfill specified continuity requirements the search direction also fulfills these continuity requirements because it turns out to be a weighted sum of these gradients.

The parameters θ_i are continuously adapted during the optimization process in order to ensure a search direction that points into the feasible domain and additionally allows for a sufficient improvement of the objective. Additionally, a phenomenon called "zigzagging" is avoided by continuous adaption of the push-off factors. This phenomenon is caused by a sequence of active and inactive constraints and usually results in bad convergence behavior. Vanderplaats suggests in [Van84] the application of the update formula

$$\theta_i = \left[1 - \frac{g_i(\mathbf{s}^{(k)})}{\epsilon} \right]^2 \theta_0 \quad (4.39)$$

with $\epsilon < 0$ for the modification of the push-off factors. The parameter ϵ specifies a small tolerance region around the constraint boundary $g_i(\mathbf{s}^{(k)}) = 0$. As soon as the constraint i reaches the tolerance level ($g_i(\mathbf{s}^{(k)}) = \epsilon$) it becomes active and $\theta_i = 0$. The push-off factor increases quadratically until $\theta_i = \theta_0$ (mostly $\theta_0 = 1$) as the constraint reaches the level $g_i(\mathbf{s}^{(k)}) = 0$. The

size of the tolerance region depends on the type of the constraint. Highly nonlinear functions, e.g. stresses require a value of $\epsilon \approx -0.05$ whereas nearly linear functions, e.g. mass are robustly tackled by $\epsilon \approx -0.005$.

The flow chart of an MFD optimization algorithm is given in figure 4.16.

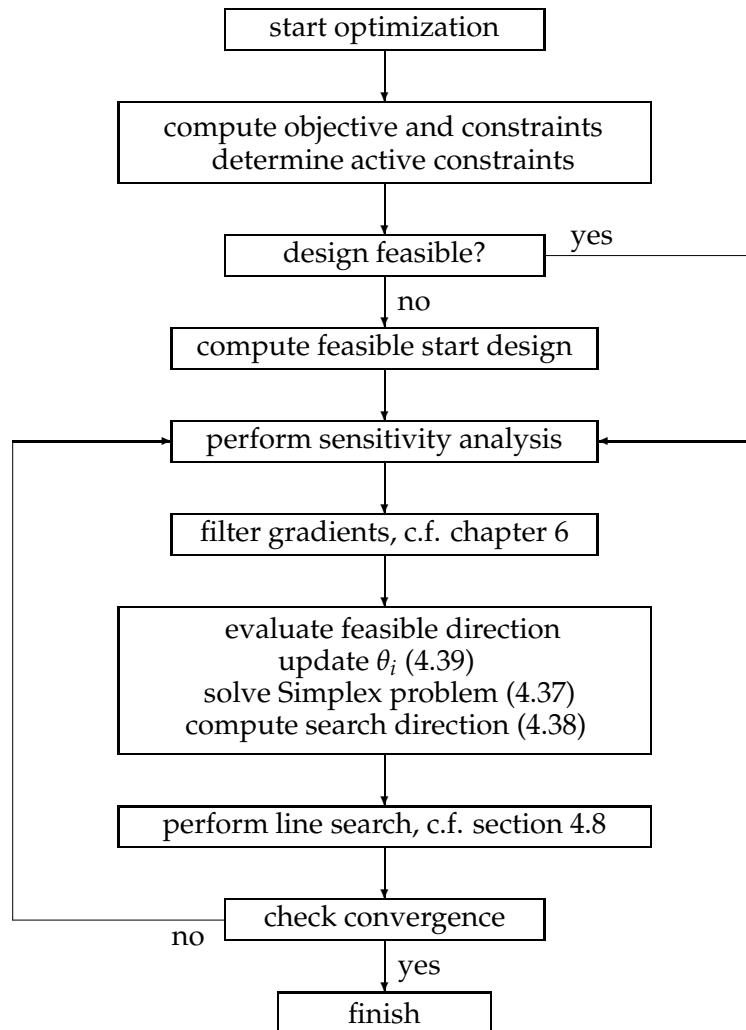


Figure 4.16: MFD optimization algorithm

4.7.2 Augmented Lagrange Multiplier Method

The Augmented Lagrange Multiplier (ALM) Method is an algorithm for constrained optimization problems using first order gradients and Lagrange multipliers. Like in other penalty methods (c.f. [HG92], [Van84]) the

constraint problem is solved by several unconstrained optimization steps. The unconstrained problem is formulated by an augmented Lagrangian function which tends to the original objective close to the constrained optimum.

The ALM Method was originally developed for equality constrained optimization problems but there exist several enhancements regarding inequality constrained problems. The following derivations focus on application for inequality constraints. In contrast to interior point methods like the Method of Feasible Directions the ALM Method does not require a feasible initial design. Moreover, it is not seldom that the algorithm works for many optimization steps in the infeasible domain until it reaches feasible designs.

Basically, the minimization of the constrained optimization problem (3.1) is substituted by unconstrained minimization of an augmented Lagrangian function stated as

$$L_A(\mathbf{s}^{(k)}, \boldsymbol{\lambda}, r_p) = f(\mathbf{s}^{(k)}) + \sum_{i=1}^{n_{act}^s} (\lambda_i \Psi_i + r_p \Psi_i^2) \quad (4.40)$$

with

$$\Psi_i = \max \left[g_i(\mathbf{s}^{(k)}), -\frac{\lambda_i}{2r_p} \right]. \quad (4.41)$$

Equation 4.40 is similar to the standard Lagrangian function (3.2) except of the last term but both equations tend to the objective function for the constrained optimum where $g_i(\mathbf{s}^{(k)}) \rightarrow 0$. The function Ψ_i specified in (4.41) is necessary to consider that the constraint $g_i(\mathbf{s}^{(k)})$ may be active or inactive during the optimization process.

The ALM Method minimizes (4.40) where the Lagrange multipliers λ_i are updated continuously. As final result one obtains the optimal design that fulfills all constraints, the set of active constraints and the respective Lagrange multipliers. The first order derivative of (4.40) with respect to the design variables \mathbf{s} is specified by

$$\frac{dL_A(\mathbf{s}^{(k)}, \boldsymbol{\lambda}, r_p)}{d\mathbf{s}} = \nabla L_A(\mathbf{s}^{(k)}, \boldsymbol{\lambda}, r_p) = \nabla f(\mathbf{s}^{(k)}) + \sum_{i=1}^{n_{act}^s} (\lambda_i \nabla \Psi_i + 2r_p \Psi_i \nabla \Psi_i) \quad (4.42)$$

with

$$\nabla \Psi_i = \begin{cases} \nabla g_i(\mathbf{s}^{(k)}) & \text{if } g_i(\mathbf{s}^{(k)}) > -\frac{\lambda_i}{2r_p} \\ 0 & \text{if } g_i(\mathbf{s}^{(k)}) < -\frac{\lambda_i}{2r_p}. \end{cases} \quad (4.43)$$

The search direction \mathbf{s}_d of the ALM Method is usually specified by the negative gradient of the augmented Lagrangian

$$\mathbf{s}_d^{(k)} = -\nabla L_A(\mathbf{s}^{(k)}, \boldsymbol{\lambda}, r_p). \quad (4.44)$$

During the optimization process the Lagrange parameters and penalty factors are updated by

$$\lambda_i^{(k+1)} = \lambda_i^{(k)} + 2r_p^{(k)} \max \left[g_i(\mathbf{s}^{(k+1)}), -\frac{\lambda_i^{(k)}}{2r_p^{(k)}} \right] \quad (4.45)$$

and

$$r_p^{(k+1)} = \gamma r_p^{(k)} \quad \text{with} \quad \gamma \geq 1 \quad \text{and} \quad r_p^{(k+1)} < r_p^{max} \quad (4.46)$$

respectively. Similar to other approximation techniques like penalty methods or Sequential Quadratic Programming (SQP) Methods some additional assumptions are necessary to compute the step length in the line search, c.f. section 4.8. The objective function is generally not well suited because it does not account for the constraints. The Lagrange function (equation 3.2) is also not appropriate because it is a saddle function. SQP Methods usually apply special merit functions which approximate the optimum and serve as measure for the determination of the step length. ALM Methods provide the augmented Lagrangian which is convex close to the optimum for sufficiently large penalty factors. Therefore, the line search can be formulated by polynomial interpolation of the augmented Lagrangian as presented in [Van84].

The implementation of the ALM Method for inequality constraint problems is presented in figure 4.17. It shows the basic algorithmic steps and the references to the respective formulas. More information about ALM Methods is presented in [HG92] and [Van84].

There exist several other constrained optimization methods, e.g. the Method of Moving Asymptotes (MMA) and the Sequential Quadratic Programming Method (SQP). In [Dao05] the MMA approach was applied to constraint shape optimization problems with FE-based parametrization. This approach works well if the the problem allows a sufficient approximation of the move limits. The SQP Method is a second order approach which employs approximated second order derivatives. This method was not applied here because of two major disadvantages.

- In general, the first order response derivatives with respect to FE parameters are not smooth. The necessary continuity is established

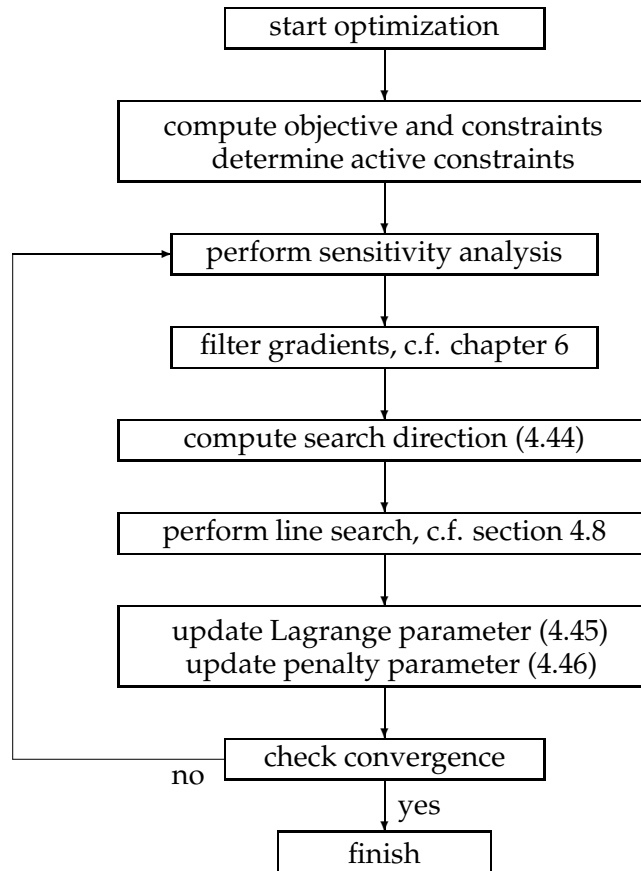


Figure 4.17: ALM optimization algorithm

by the regularization methods presented in chapter 6. Consequently, the approximation of second order derivatives suffers seriously from non-smooth first order gradients. Hence, the second order information of the Hessian matrix is of minor quality only and may be misleading.

- Structural optimization with FE-based parametrization results in large design spaces and therefore to numerically expensive sensitivity analysis procedures. The numerical effort as well as amount of required memory of SQP Methods is significantly larger than for first order methods because of the Hessian matrix.

4.8 Line Search

The intermediate result of each optimization step is the search direction \mathbf{s}_d . The line search algorithm computes the step length α which is used as scaling parameter to specify the design update, c.f. equation 4.28. Obviously, the line search parameter should be chosen such that the design update results in a maximum reduction of the objective. Thus, the step length determination is a one dimensional optimization problem. Many mathematical optimization procedures do not require an exact determination of the step length. An adequate approximation is mostly sufficient and requires much less numerical effort. There exists a large variety of one dimensional optimization strategies which are in general applicable for a step length approximation.

The Golden Section Method is an interval search method that applies zero order information [Van84]. It requires unimodal functions and an interval containing the minimum. The interval size is sequentially decreased such that the minimum remains in the resulting interval. For each step the Golden Section Method requires only one additional function evaluation. The iteration is terminated when the interval size reaches a predefined limit. In general, the FE-based parametrization leads to highly non-convex optimization problems which do not provide unimodal functions for the line search procedure. Thus, the Golden Section Method is not applicable to this type of problems.

The Armijo test [Aro04] is an inaccurate line search method that requires only a minimal number of function evaluations. The Armijo test is passed when the objective is sufficiently decreased for a reasonable step size. This check is based on the function value at the initial position and the first order gradients. As presented in chapter 6 these gradients are usually not smooth. Due to this the extrapolation based on gradient information may be misleading.

Polynomial interpolations are a powerful class of one dimensional optimization algorithms. These methods are usually based on zero and/or first order information. Higher order methods like cubic or quartic interpolations are mostly based on first order information which may disturb the results seriously as explained before. But the quadratic interpolation can be effectively formulated by only zero order data. This ensures a very robust approach with a minimum number of function evaluations. The basic properties of this approach are depicted in figure 4.18.

The computation starts at the current design expressed by the objective value $f_0^{(k)}$.

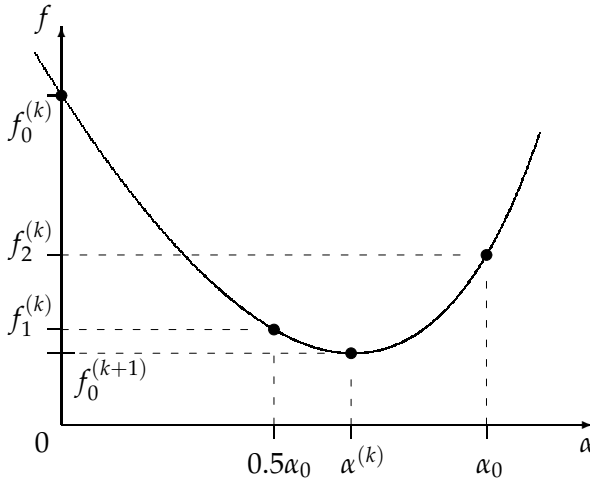


Figure 4.18: Quadratic line search

Two subsequent design updates by $\alpha = 0.5\alpha_0$ and $\alpha = 1.0\alpha_0$ provide the function values $f_1^{(k)}$ and $f_2^{(k)}$. The predefined parameter α_0 determines the search interval and additionally serves as upper bound to the step length parameter $\alpha^{(k)}$. Whenever the computed step length is larger than α_0 the step length for the next iteration step is computed by $\alpha^{(k)} = \alpha_0$. Based on the known objective values $f_0^{(k)}$, $f_1^{(k)}$ and $f_2^{(k)}$ and the step length α_0 the optimal step length $\alpha^{(k)}$ can be computed by

$$\alpha^{(k)} = \frac{3f_0^{(k)} - 4f_1^{(k)} + f_2^{(k)}}{4(f_0^{(k)} - 2f_1^{(k)} + f_2^{(k)})} \alpha_0 \quad (4.47)$$

If the computed step length is smaller than zero the procedure is repeated for a decreased step length parameter α_0 . This quadratic line search requires three function evaluations per step if $0 \leq \alpha^{(k)} \leq \alpha_0$. In this case the functions values for $f_1^{(k)}$, $f_2^{(k)}$ and $f_0^{(k+1)}$ have to be evaluated. In the case that $\alpha^{(k)} \geq \alpha_0$ only two function evaluations are necessary because the updated design is already expressed by $f_0^{(k+1)} = f_2^{(k)}$.

Chapter 5

Exact Semi-Analytical Sensitivity Analysis

This chapter presents a straightforward and generally applicable method for detection and elimination of errors in semi-analytical design sensitivities for any kind of FE formulation. As motivated in section 4.3.6 the semi-analytical approach has many advantages in application. The only serious disadvantage is the approximation error due to the finite size of the perturbation. Unfortunately, these small errors in the computation of element derivatives increase seriously when these derivatives are used in further computations. Thus, application of semi-analytical sensitivities requires correction methods to minimize this error amplification.

The basic effects of the mentioned approximation errors can be shown via beam elements, e.g. with Euler-Bernoulli kinematics and Timoshenko kinematics. Additionally, these simple elements offer the possibility to emphasize the consequences of the approximation errors by analytical computations of the error terms. These two element types show serious differences in the errors of the sensitivities. The ideas gained by the simple 1-d elements are easily extended to 3-d solid or shell elements.

5.1 Motivation

By choice of a small but finite perturbation parameter Δs in the element derivatives either truncation or approximation errors occur. These errors have serious influence on the accuracy of the sensitivity analysis. Barthelemy and Haftka observed in [BH88] two different types of errors.

For elements with Euler-Bernoulli or Kirchhoff kinematics, the numerical error of displacement sensitivities with respect to shape design variables increases inversely proportional to the square of the size of the perturbed

elements. The source of inaccuracy is the approximation of the pseudo load vector (3.38) (c.f. [BH88]), which is the load that must be applied to the structure to obtain the displacement sensitivity field. For the above mentioned elements the sensitivity displacement field is not a reasonable displacement field for the model and its boundary conditions. The displacement sensitivity to a length dimension is dominated by shear rather than bending. These shear components cause large components in the pseudo load vector. Furthermore, small truncation errors are included in the pseudo load which amplify into large errors in the displacement sensitivities (c.f. [Lun94]).

A second type of error is related to long span structures subjected to bending. This inaccuracy occurs for all element formulations and is caused by the rotation of the elements. In this case the errors of the displacement sensitivities with respect to a length dimension increase rapidly with the length of the structure.

There exists a great variety of methods which try to eliminate the above mentioned problems, c.f. the review in [vKHK05]. Haftka and Adelman ([HA89]) use central differences instead of forward differences to decrease the approximation error. Cheng, Gu and Zhou ([CGZ89]) propose an alternate forward backward approximation scheme which also decreases the approximation error. Cheng, Gu and Wang ([CGW91]) introduced a second order correction method. None of these methods can completely eliminate the accuracy problem. 'Exact' sensitivities are obtained due to a method derived by Olhoff, Rasmussen and Lund ([ORL92], [LO93], [LO94], [Lun94]), which computes correction factors for a premultiplication. The application of the so called natural method was proposed by Mlejnek ([Mle92]). Within this approach the modal description is used which offers an easy identification and elimination of the error terms. Cheng and Olhoff derived a method for the computation of correction factors for the stiffness matrix derivative. They showed in ([CO93]) a direct dependency between the rigid body rotation vectors and the approximation errors. Based on these two approaches van Keulen and de Boer ([vKdB98] and [dBvKV02]) introduced the method of exact differentiation of rigid body modes which also eliminates the errors completely. However, this method depends on the specific finite element formulation. Thus, it has to be derived and programmed for each element separately. This property prevents a straightforward implementation in existing finite element codes.

5.2 Problem Description

The source of the accuracy problems in the semi-analytical sensitivity analysis is shown within this section. Euler-Bernoulli and Timoshenko formulations are used to derive the error terms analytically. Additionally, consequences on discretized beam structures are shown by two examples.

Recalling the work of Mlejnek ([Mle92]) it is assumed that a free, unsupported structure can undergo rigid body translations and rotations. These so called "zero eigen vectors" $\boldsymbol{\phi}$ do not introduce any forces, i.e.:

$$\mathbf{K}\boldsymbol{\phi} = \mathbf{0} \quad (5.1)$$

The partial derivative of Equation (5.1) with respect to a design variable s yields:

$$\frac{\partial \mathbf{K}}{\partial s} \boldsymbol{\phi} + \mathbf{K} \frac{\partial \boldsymbol{\phi}}{\partial s} = \mathbf{0} \quad (5.2)$$

By a premultiplication with $\boldsymbol{\phi}^T$ one obtains:

$$\boldsymbol{\phi}^T \frac{\partial \mathbf{K}}{\partial s} \boldsymbol{\phi} + \boldsymbol{\phi}^T \mathbf{K} \frac{\partial \boldsymbol{\phi}}{\partial s} = 0 \quad (5.3)$$

Applying (5.1) in (5.3) gives the rigid body condition for the derivative of the stiffness matrix.

$$\boldsymbol{\phi}^T \frac{\partial \mathbf{K}}{\partial s} \boldsymbol{\phi} = 0 \quad (5.4)$$

This condition holds for rigid body translation vectors ($\boldsymbol{\phi}_t$) as well as for rigid body rotation vectors ($\boldsymbol{\phi}_r$):

$$\boldsymbol{\phi}_t^T \frac{\partial \mathbf{K}}{\partial s} \boldsymbol{\phi}_t = 0; \quad \boldsymbol{\phi}_r^T \frac{\partial \mathbf{K}}{\partial s} \boldsymbol{\phi}_r = 0. \quad (5.5)$$

The approximation of the exact derivative of the stiffness matrix by first order forward and first order central finite difference expressions yields:

$$\begin{aligned} \frac{\partial \mathbf{K}}{\partial s} &\approx \frac{\mathbf{K}(s + \Delta s) - \mathbf{K}}{\Delta s} = \frac{\Delta \mathbf{K}^f}{\Delta s}; \\ \frac{\partial \mathbf{K}}{\partial s} &\approx \frac{\mathbf{K}(s + \Delta s) - \mathbf{K}(s - \Delta s)}{2\Delta s} = \frac{\Delta \mathbf{K}^c}{2\Delta s} \end{aligned} \quad (5.6)$$

and as described in the following one observes for the rigid body conditions (5.5₁) and (5.5₂):

$$\begin{aligned} \boldsymbol{\phi}_t^T \frac{\Delta \mathbf{K}^f}{\Delta s} \boldsymbol{\phi}_t &= 0; \quad \boldsymbol{\phi}_t^T \frac{\Delta \mathbf{K}^c}{2\Delta s} \boldsymbol{\phi}_t = 0; \\ \boldsymbol{\phi}_r^T \frac{\Delta \mathbf{K}^f}{\Delta s} \boldsymbol{\phi}_r &\neq 0; \quad \boldsymbol{\phi}_r^T \frac{\Delta \mathbf{K}^c}{2\Delta s} \boldsymbol{\phi}_r \neq 0 !!! \end{aligned} \quad (5.7)$$

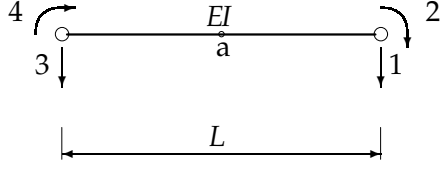
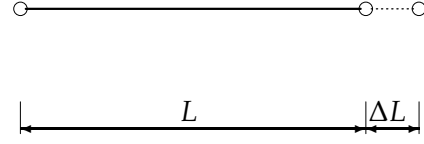


Figure 5.1: Dofs of beam elements

Figure 5.2: Length perturbation by ΔL

In general, the prerequisite for the rigid body rotation is not fulfilled exactly if the partial derivative is approximated by a finite difference formulation. Subsequently, the error terms for the linear Euler-Bernoulli and the Timoshenko beam element are derived analytically to identify the error behavior. Based on the definition for the nodal degrees of freedom which is specified in figure 5.1 the stiffness matrix for a linear Euler-Bernoulli beam takes the well known format:

$$\mathbf{K}_b = EI \begin{bmatrix} \frac{12}{L^3} & -\frac{6}{L^2} & -\frac{12}{L^3} & -\frac{6}{L^2} \\ -\frac{6}{L^2} & \frac{4}{L} & \frac{6}{L^2} & \frac{2}{L} \\ -\frac{12}{L^3} & \frac{6}{L^2} & \frac{12}{L^3} & \frac{6}{L^2} \\ -\frac{6}{L^2} & \frac{2}{L} & \frac{6}{L^2} & \frac{4}{L} \end{bmatrix}, \quad (5.8)$$

with the Young's modulus E and the second moment of inertia I . The quantity EI is denoted as bending stiffness. The derivative of \mathbf{K}_b with respect to the length L is defined by:

$$\frac{\partial \mathbf{K}_b}{\partial L} = EI \begin{bmatrix} -\frac{36}{L^4} & \frac{12}{L^3} & \frac{36}{L^4} & \frac{12}{L^3} \\ \frac{12}{L^3} & -\frac{4}{L^2} & -\frac{12}{L^3} & -\frac{2}{L^2} \\ \frac{36}{L^4} & -\frac{12}{L^3} & -\frac{36}{L^4} & -\frac{12}{L^3} \\ \frac{12}{L^3} & -\frac{2}{L^2} & -\frac{12}{L^3} & -\frac{4}{L^2} \end{bmatrix} \quad (5.9)$$

The first order forward and central finite difference approximations (c.f. equation 5.6) of the derivative are given by equations 5.10 and 5.11 respectively, where the length increment is taken as ΔL . As motivated before the error in the semi-analytical sensitivities is related to the rigid body rotation vector $\boldsymbol{\phi}_r$. For a rotation around the center of a geometrically linear 2-d beam element (point a in figure 5.1) this vector is given by:

$$\boldsymbol{\phi}_r^T = \left[\frac{L}{2}\theta \quad \theta \quad -\frac{L}{2}\theta \quad \theta \right] \quad (5.12)$$

$$\frac{\Delta \mathbf{K}_b^f}{\Delta L} = EI \begin{bmatrix} \frac{-12(3L^2+3L\Delta L+(\Delta L)^2)}{(L+\Delta L)^3L^3} & \frac{6(2L+\Delta L)}{(L+\Delta L)^2L^2} & \frac{12(3L^2+3L\Delta L+(\Delta L)^2)}{(L+\Delta L)^3L^3} & \frac{6(2L+\Delta L)}{(L+\Delta L)^2L^2} \\ \frac{6(2L+\Delta L)}{(L+\Delta L)^2L^2} & \frac{-4}{(L+\Delta L)L} & \frac{-6(2L+\Delta L)}{(L+\Delta L)^2L^2} & \frac{-2}{(L+\Delta L)L} \\ \frac{12(3L^2+3L\Delta L+(\Delta L)^2)}{(L+\Delta L)^3L^3} & \frac{-6(2L+\Delta L)}{(L+\Delta L)^2L^2} & \frac{-12(3L^2+3L\Delta L+(\Delta L)^2)}{(L+\Delta L)^3L^3} & \frac{-6(2L+\Delta L)}{(L+\Delta L)^2L^2} \\ \frac{6(2L+\Delta L)}{(L+\Delta L)^2L^2} & \frac{-2}{(L+\Delta L)L} & \frac{-6(2L+\Delta L)}{(L+\Delta L)^2L^2} & \frac{-4}{(L+\Delta L)L} \end{bmatrix} \quad (5.10)$$

$$\frac{\Delta \mathbf{K}_b^c}{2\Delta L} = EI \begin{bmatrix} \frac{12(3L^2+\Delta L^2)}{(L+\Delta L)^3(-L+\Delta L)^3} & \frac{12L}{(L+\Delta L)^2(-L+\Delta L)^2} & \frac{-12(3L^2+\Delta L^2)}{(L+\Delta L)^3(-L+\Delta L)^3} & \frac{12L}{(L+\Delta L)^2(-L+\Delta L)^2} \\ \frac{12L}{(L+\Delta L)^2(-L+\Delta L)^2} & \frac{4}{-L^2+\Delta L^2} & \frac{-12L}{(L+\Delta L)^2(-L+\Delta L)^2} & \frac{2}{-L^2+\Delta L^2} \\ \frac{-12(3L^2+\Delta L^2)}{(L+\Delta L)^3(-L+\Delta L)^3} & \frac{-12L}{(L+\Delta L)^2(-L+\Delta L)^2} & \frac{12(3L^2+\Delta L^2)}{(L+\Delta L)^3(-L+\Delta L)^3} & \frac{-12L}{(L+\Delta L)^2(-L+\Delta L)^2} \\ \frac{12L}{(L+\Delta L)^2(-L+\Delta L)^2} & \frac{2}{-L^2+\Delta L^2} & \frac{-12L}{(L+\Delta L)^2(-L+\Delta L)^2} & \frac{4}{-L^2+\Delta L^2} \end{bmatrix} \quad (5.11)$$

Applying the rigid body test by pre- and postmultiplying the approximated derivatives with the vector $\boldsymbol{\phi}_r$ yields:

$$\begin{aligned} \boldsymbol{\phi}_r^T \frac{\Delta \mathbf{K}_b^f}{\Delta L} \boldsymbol{\phi}_r &= \frac{12EI\Delta L\theta^2}{(L+\Delta L)^3}; \\ \boldsymbol{\phi}_r^T \frac{\Delta \mathbf{K}_b^c}{2\Delta L} \boldsymbol{\phi}_r &= \frac{12EI\Delta L^2(3L^2+\Delta L^2)\theta^2}{(L^2-\Delta L^2)(L+\Delta L)^2(L-\Delta L)^2}. \end{aligned} \quad (5.13)$$

Additionally, the stiffness matrix, the exact derivative and the approximated derivatives of the linear Timoshenko beam are provided. A reduced 1-point integration is used to prevent the well known shear locking effects of this element formulation.

$$\mathbf{K}_t = \begin{bmatrix} \frac{GA}{L} & -\frac{GA}{2} & -\frac{GA}{L} & -\frac{GA}{2} \\ -\frac{GA}{2} & \frac{EI}{L} + \frac{GAL}{4} & \frac{GA}{2} & -\frac{EI}{L} + \frac{GAL}{4} \\ -\frac{GA}{L} & \frac{GA}{2} & \frac{GA}{L} & \frac{GA}{2} \\ -\frac{GA}{2} & -\frac{EI}{L} + \frac{GAL}{4} & \frac{GA}{2} & \frac{EI}{L} + \frac{GAL}{4} \end{bmatrix} \quad (5.14)$$

$$\frac{\Delta \mathbf{K}_t^f}{\Delta L} = \begin{bmatrix} -\frac{GA}{(L+\Delta L)L} & 0 & \frac{GA}{(L+\Delta L)L} & 0 \\ 0 & \frac{GAL^2+GAL\Delta L-4EI}{4(L+\Delta L)L} & 0 & \frac{GAL^2+GAL\Delta L+4EI}{4(L+\Delta L)L} \\ \frac{GA}{(L+\Delta L)L} & 0 & -\frac{GA}{(L+\Delta L)L} & 0 \\ 0 & \frac{GAL^2+GAL\Delta L+4EI}{4(L+\Delta L)L} & 0 & \frac{GAL^2+GAL\Delta L-4EI}{4(L+\Delta L)L} \end{bmatrix} \quad (5.16)$$

$$\frac{\Delta \mathbf{K}_t^c}{2\Delta L} = \begin{bmatrix} -\frac{GA}{L^2-\Delta L^2} & 0 & \frac{GA}{L^2-\Delta L^2} & 0 \\ 0 & \frac{-4EI+GAL^2-GA\Delta L^2}{4(L^2-\Delta L^2)} & 0 & \frac{4EI+GAL^2-GA\Delta L^2}{4(L^2-\Delta L^2)} \\ \frac{GA}{L^2-\Delta L^2} & 0 & -\frac{GA}{L^2-\Delta L^2} & 0 \\ 0 & \frac{4EI+GAL^2-GA\Delta L^2}{4(L^2-\Delta L^2)} & 0 & \frac{-4EI+GAL^2-GA\Delta L^2}{4(L^2-\Delta L^2)} \end{bmatrix} \quad (5.17)$$

$$\frac{\partial \mathbf{K}_t}{\partial L} = \begin{bmatrix} -\frac{GA}{L^2} & 0 & \frac{GA}{L^2} & 0 \\ 0 & -\frac{EI}{L^2} + \frac{GA}{4} & 0 & \frac{EI}{L^2} + \frac{GA}{4} \\ \frac{GA}{L^2} & 0 & -\frac{GA}{L^2} & 0 \\ 0 & \frac{EI}{L^2} + \frac{GA}{4} & 0 & -\frac{EI}{L^2} + \frac{GA}{4} \end{bmatrix} \quad (5.15)$$

The so called shear stiffness is defined by the parameter GA with the shear modulus G and the cross section area A .

The rigid body test is also applied to the approximated derivatives of the Timoshenko beam element. This results in the following error terms for the first order forward and central finite difference approaches:

$$\begin{aligned} \boldsymbol{\phi}_r^T \frac{\Delta \mathbf{K}_t^f}{\Delta L} \boldsymbol{\phi}_r &= \frac{GA\Delta L\theta^2}{L + \Delta L}; \\ \boldsymbol{\phi}_r^T \frac{\Delta \mathbf{K}_t^c}{\Delta L} \boldsymbol{\phi}_r &= -\frac{GA\Delta L^2\theta^2}{L^2 - \Delta L^2}. \end{aligned} \quad (5.18)$$

It becomes obvious, that the approximations of the stiffness matrix derivative do not fulfill the rigid body test neither for Euler-Bernoulli nor for Timoshenko kinematics. A more detailed inspection of the error terms (equations 5.13 and 5.18) shows a less critical behavior of the central difference approximations. Here, the errors are decreased by a factor of $\Delta L/L$ as compared to the forward finite differences. However, one has to provide an additional stiffness matrix for the configuration $\mathbf{K}(s - \Delta s)$. The prescribed errors have serious influences on the accuracy of displacement sensitivities. This is shown by the following two examples. Subsequently, only first order forward finite differences are applied to show the error propagation

of the semi-analytic approach. Therefore, the superscript f used so far is omitted to simplify the formulations.

5.2.1 Model Problem I

The first example [BH88] considers a cantilever beam of length $L = 1$ under a tip moment. The number of elements n varies from 1 to 20.

Thus the length of each single element L_e decreases with L/n . The goal is to determine the sensitivity of the tip displacement u_1 with respect to the length of the beam for the different discretizations. The analytical Euler-Bernoulli solution is compared to the numerical Euler-Bernoulli and Timoshenko results. The analytical solution of the displacement function $u(x)$ and its derivative $u'(x)$ of MP I ends up in the equations:

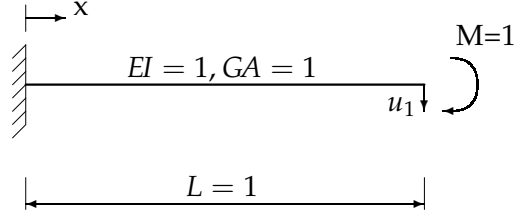


Figure 5.3: Cantilever with tip moment

The analytical solution of the displacement function $u(x)$ and its derivative $u'(x)$ of MP I ends up in the equations:

$$u(x) = \frac{Mx^2}{2EI} \quad \text{and} \quad \frac{du(x)}{dx} = u'(x) = \frac{Mx}{EI} \quad (5.19)$$

respectively. Thus, one obtains for the sensitivity of the tip displacement u_1

$$u'(x = L) = \frac{ML}{EI} = 1. \quad (5.20)$$

The semi-analytical sensitivities of the Euler-Bernoulli and the Timoshenko elements are computed by

$$\begin{aligned} \frac{d\mathbf{u}_b}{dL} &\approx \mathbf{K}_b^{-1} \left(-\frac{\Delta\mathbf{K}_b}{\Delta L} \mathbf{u}_b \right) \quad \text{and} \\ \frac{d\mathbf{u}_t}{dL} &\approx \mathbf{K}_t^{-1} \left(-\frac{\Delta\mathbf{K}_t}{\Delta L} \mathbf{u}_t \right) \quad \text{respectively.} \end{aligned} \quad (5.21)$$

The parameter ΔL is defined as $p \cdot L_e$ with $p = 1 \cdot 10^{-04}$ and the element length $L_e = L/n$. As depicted in figure 5.4 the sensitivity error of the Euler-Bernoulli beam elements is much more amplified than for the Timoshenko beam elements. Furthermore the graph increases quadratically with the number of elements. This effect was also recognized by Barthelemy and Haftka in [BH88] and many others. The sensitivities of the Timoshenko beam do not show such inaccuracies. The reason of this behavior are the

error terms formulated in (5.13) and (5.18). The error of the Euler-Bernoulli beam increases dramatically (third power in the denominator) if the length of the element L_e tends to zero. The denominator of the right hand side

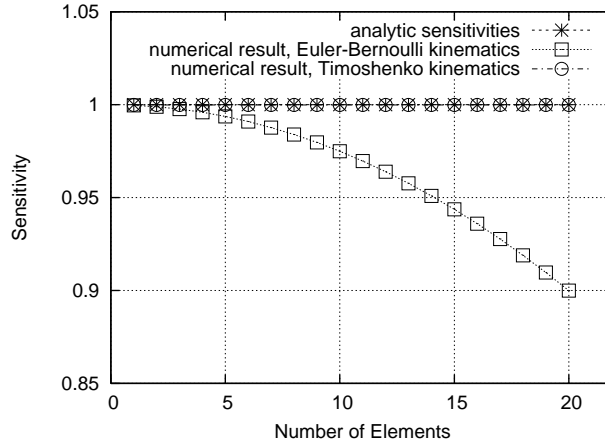


Figure 5.4: du_b/dL and du_t/dL for MP I

of equation 5.18a is only linear and hence, the error propagation does not show this behavior. Thus, this kind of error has a tremendous effect to elements with higher order kinematic assumptions. Later it is shown that these general observations can be extended to more dimensional problems including plates and shells with Reissner-Mindlin kinematics respectively.

A second type of error (c.f. [BH88]) is shown by example II.

5.2.2 Model Problem II

The second example also considers a cantilever beam. In contrast to Model Problem I the length of the beam L and the tip moment M are not constant. Instead of the beam length the length of elements L_e is constant ($L_e = 1$). Thus, the length of the beam varies by $L = n \cdot L_e$ with $n \in \{1..20\}$. The tip moment decreases by $M = 1/n$. Bending and shear stiffness are constant ($EI = GA = 1$).

Also in this example the sensitivity of the tip displacement with respect to the beam length is compared for analytical and semi-analytical calculations. Timoshenko and Euler-Bernoulli beam elements are applied for the numerical simulations and the analytical result is computed by the Euler-Bernoulli beam theory. The derivative of the displacement function

at $x = L$ is given by:

$$\frac{du(x=L)}{dx} = u'(x=L) = \frac{ML}{EI}. \quad (5.22)$$

Substituting the expressions $L = L_e \cdot n$ and $M = 1/n$ in Equation (5.22) yields to:

$$\begin{aligned} \frac{du(x=L)}{dx} = u'(x=L) &= \frac{L_e \cdot n}{n \cdot EI} \implies \\ u'(x=L) &= \frac{L_e}{EI} = 1. \end{aligned} \quad (5.23)$$

Thus, the exact result is equal to 1, for an arbitrary beam length. According to Model Problem I the numerical results are computed by equations 5.21a and 5.21b. The results of this example are depicted in figure 5.5. It is

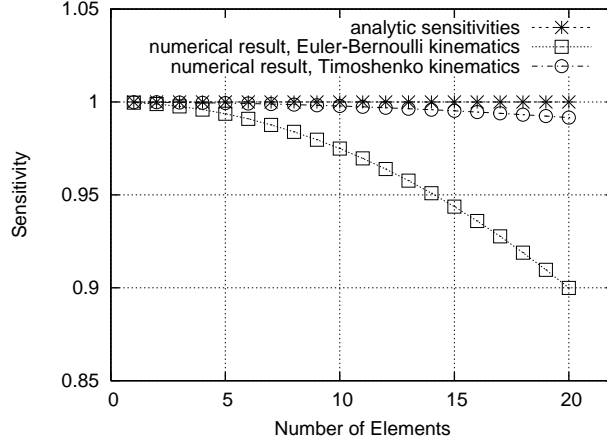


Figure 5.5: du_b/dL and du_t/dL for MP II

interesting to see that the numerical results of the Euler-Bernoulli beam as well as of the Timoshenko beam show inaccuracies. These errors increase quadratically with the beam length. Obviously, this behavior is also caused by the error terms (5.13) and (5.18). Due to the problem setting of this example the tip displacement as well as the rotation angle θ of each element increase with increasing beam length. The error terms depend quadratically on the rotation vector which results in the depicted behavior.

The inaccuracies of the displacement sensitivities of Timoshenko and Euler-Bernoulli beam elements can be resumed to the following two statements:

1. Bending driven models (i.e. Euler-Bernoulli beams, Kirchhoff shells) show accuracy problems in the displacement sensitivities with increasing discretization density. Shear driven models like Timoshenko

beams or Reissner-Mindlin shells do not show this effect. The order of the shape functions does not affect this approximation error. This can also be shown for membrane elements, e.g. with bilinear and biquadratic formulations respectively.

2. Models with moderate rigid body rotations of the elements also show accuracy problems in the approximated displacement derivatives. This type of inaccuracy appears for all kind of elements because it is related to the rotation angle.

The following section provides an efficient method to correct the errors contained in the approximated displacement sensitivities.

5.3 Exact Semi-Analytical Sensitivities

This section presents an effective and straightforward method to compute a modified stiffness matrix derivative which satisfies the rigid body test, c.f. (5.7)b. The basic idea is to modify the approximated stiffness matrix derivative by another matrix based on the dyadic products of element rotation vectors. Subsequently, the method is introduced for the 1-d case. It can easily be extended to 2-d and 3-d problems. Furthermore, the derivations concentrate on the forward finite difference approximations.

The goal is to compute a factor a such that the modified stiffness matrix derivative $\Delta\mathbf{K}^*$ fulfills the rigid body condition

$$\underbrace{\boldsymbol{\phi}_r^T \left(\frac{\Delta\mathbf{K}}{\Delta L} + a \boldsymbol{\phi}_r \boldsymbol{\phi}_r^T \right) \boldsymbol{\phi}_r}_{\Delta\mathbf{K}^*} = 0. \quad (5.24)$$

This gives the form:

$$\begin{aligned} \boldsymbol{\phi}_r^T \frac{\Delta\mathbf{K}}{\Delta L} \boldsymbol{\phi}_r + a (\boldsymbol{\phi}_r \cdot \boldsymbol{\phi}_r) (\boldsymbol{\phi}_r \cdot \boldsymbol{\phi}_r) &= 0 \implies \\ a &= - \frac{\boldsymbol{\phi}_r^T \frac{\Delta\mathbf{K}}{\Delta L} \boldsymbol{\phi}_r}{(\boldsymbol{\phi}_r \cdot \boldsymbol{\phi}_r) (\boldsymbol{\phi}_r \cdot \boldsymbol{\phi}_r)} \end{aligned} \quad (5.25)$$

By applying this procedure to the Euler-Bernoulli and Timoshenko beam element one obtains the parameters:

$$a_b = - \frac{48EI\Delta L}{\theta^2 (L_e + \Delta L)^3 (L_e^4 + 8L_e^2 + 16)} \quad \text{and} \quad (5.26)$$

$$a_t = - \frac{4GA\Delta L}{\theta^2 (L_e + \Delta L) (L_e^4 + 8L_e^2 + 16)} \quad (5.27)$$

respectively. The result is a modified approximation of the stiffness matrix derivative, called $\Delta\mathbf{K}^*$ which satisfies the rigid body condition (equation 5.7b)

$$\begin{aligned} \boldsymbol{\phi}_r^T (\Delta\mathbf{K}^*) \boldsymbol{\phi}_r &= 0 \quad \text{with} \\ \Delta\mathbf{K}^* &= \frac{\Delta\mathbf{K}}{\Delta L} + a \boldsymbol{\phi}_r \boldsymbol{\phi}_r^T. \end{aligned} \quad (5.28)$$

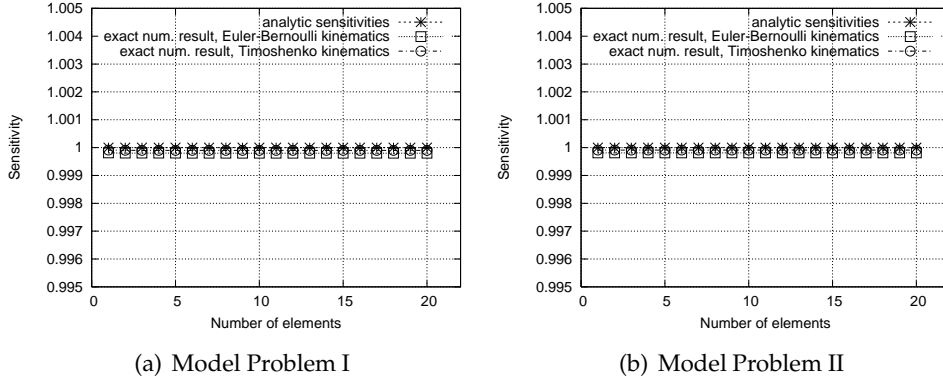


Figure 5.6: Modified sensitivities for Model Problems I and II

A repeated computation of the model problems results in the graphs depicted in figures 5.6a and 5.6b. The only modification in the algorithm is the exchange of the term $\frac{\Delta\mathbf{K}}{\Delta L}$ by $\Delta\mathbf{K}^*$ in equations 5.21a and 5.21b. One can easily see that the errors disappear completely for Euler-Bernoulli as well as for Timoshenko beam elements. The remaining difference between the analytical and the numerical results is caused by the approximation error. The order $1 \cdot 10^{-04}$ corresponds to the perturbation factor, c.f. page 79.

The method introduced so far can be extended to 2-d and 3-d elements in a straightforward manner. Therefore, equation 5.24 is generalized to:

$$\boldsymbol{\phi}_r^{iT} \underbrace{\left(\frac{\Delta\mathbf{K}}{\Delta s} + a^{jk} \boldsymbol{\phi}_r^j \boldsymbol{\phi}_r^{kT} \right)}_{\Delta\mathbf{K}^*} \boldsymbol{\phi}_r^l = 0, \quad \forall i, j, k, l \in \{1..n_r\}. \quad (5.29)$$

with the number of rigid body rotation vectors n_r and the perturbation Δs . This leads to a system of equations which has to be solved. The size depends on the number of dimensions and the orthogonality conditions between the rigid body rotation vectors.

5.3.1 Orthogonalization of Rotation Vectors

The set of corresponding rigid body rotation vectors can be found by inspection for every available FE-formulation without any problem. However, these rigid body rotation vectors are in general not orthogonal. This affects the efficiency of the evaluation of equation 5.29 seriously. A reformulation of this equation results in

$$\boldsymbol{\phi}_r^{iT} \left(\frac{\Delta \mathbf{K}}{\Delta S} \right) \boldsymbol{\phi}_r^l + \boldsymbol{\phi}_r^{iT} (a^{jk} \boldsymbol{\phi}_r^j \boldsymbol{\phi}_r^{kT}) \boldsymbol{\phi}_r^l = 0, \quad \forall i, j, k, l \in \{1..n_r\}. \quad (5.30)$$

By a further manipulation of the second term one obtains

$$\underbrace{\boldsymbol{\phi}_r^{iT} \left(\frac{\Delta \mathbf{K}}{\Delta S} \right) \boldsymbol{\phi}_r^l}_{b^{il}} + a^{jk} \underbrace{(\boldsymbol{\phi}_r^i \cdot \boldsymbol{\phi}_r^j)}_{c^{ij}} \underbrace{(\boldsymbol{\phi}_r^k \cdot \boldsymbol{\phi}_r^l)}_{c^{kl}} = 0, \quad \forall i, j, k, l \in \{1..n_r\}. \quad (5.31)$$

$\underbrace{\hspace{10em}}_{d^{ijkl}}$

This expression can be reformulated to a linear system of equations of the form

$$a^{jk} d^{ijkl} = -b^{il}, \quad \forall i, j, k, l \in \{1..n_r\} \quad (5.32)$$

with a^{jk} as unknown parameters. This formulation can be written in a 9x9 system of equations for 3-d finite elements ($n_r = 3$), e.g.

$$-b^{11} = a^{11} d^{1111} + a^{12} d^{1121} + a^{13} d^{1131} + \dots + a^{33} d^{1331}. \quad (5.33)$$

Using the symmetry conditions $c^{ij} = c^{ji}$ and $c^{kl} = c^{lk}$ simplifies equation 5.33 to a 6x6 system of equations which is still expensive to be solved.

Subsequently, a method is introduced which simplifies the computation of the modification terms significantly. The basic idea of this method is to orthogonalize the rotation vectors by linear considerations.

In the further investigations it is assumed that the rigid body rotation vectors $\boldsymbol{\phi}_r^i, i \in \{1,2,3\}$ with the property $\boldsymbol{\phi}_r^i \cdot \boldsymbol{\phi}_r^j \neq 0, \forall i \neq j$ are given. Thus, this set of vectors is non-orthogonal. A set of orthogonal vectors has to fulfill the condition $\boldsymbol{\phi}_r^i \cdot \boldsymbol{\phi}_r^j = 0$ for $i \neq j$. The first step is to find a vector $\boldsymbol{\phi}_r^{2*}$ which follows from

$$\boldsymbol{\phi}_r^{2*} = \alpha \boldsymbol{\phi}_r^1 + \boldsymbol{\phi}_r^{2*}. \quad (5.34)$$

The necessary condition $\boldsymbol{\phi}_r^1 \cdot \boldsymbol{\phi}_r^{2*} = 0$ gives an equation for the parameter α

$$\alpha = \frac{\boldsymbol{\phi}_r^1 \cdot \boldsymbol{\phi}_r^2}{(\boldsymbol{\phi}_r^1)^2} \quad (5.35)$$

The vector $\boldsymbol{\phi}_r^{3*}$ with $\boldsymbol{\phi}_r^1 \cdot \boldsymbol{\phi}_r^{3*} = 0$ and $\boldsymbol{\phi}_r^{2*} \cdot \boldsymbol{\phi}_r^{3*} = 0$ is computed by

$$\boldsymbol{\phi}_r^3 = \gamma \boldsymbol{\phi}_r^1 + \beta \boldsymbol{\phi}_r^{2*} + \boldsymbol{\phi}_r^{3*}. \quad (5.36)$$

The requirement $\boldsymbol{\phi}_r^1 \cdot \boldsymbol{\phi}_r^{3*} = 0$ and $\boldsymbol{\phi}_r^{2*} \cdot \boldsymbol{\phi}_r^{3*} = 0$ gives the equations to evaluate γ and β

$$\gamma = \frac{\boldsymbol{\phi}_r^1 \cdot \boldsymbol{\phi}_r^3}{(\boldsymbol{\phi}_r^1)^2} \quad \text{and} \quad \beta = \frac{\boldsymbol{\phi}_r^{2*} \cdot \boldsymbol{\phi}_r^3}{(\boldsymbol{\phi}_r^{2*})^2}. \quad (5.37)$$

The vector $\boldsymbol{\phi}_r^{3*}$ can now be computed by equation 5.36. Finally, one obtains a set of three orthogonal vectors $\boldsymbol{\phi}_r^1$, $\boldsymbol{\phi}_r^{2*}$ and $\boldsymbol{\phi}_r^{3*}$. It is beneficial for the subsequent formulations to normalize the vectors ($\{\boldsymbol{\phi}_r^1 \boldsymbol{\phi}_r^{2*} \boldsymbol{\phi}_r^{3*}\} \rightarrow \{\boldsymbol{\phi}_{rn}^1 \boldsymbol{\phi}_{rn}^{2*} \boldsymbol{\phi}_{rn}^{3*}\}$). In the sequel it is assumed that these vectors are orthonormal basis vectors.

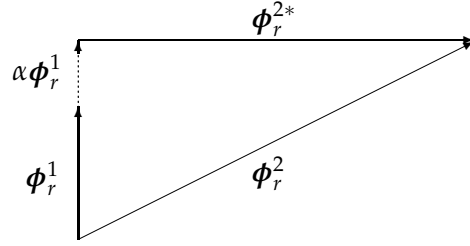


Figure 5.7: Orthogonalization of $\boldsymbol{\phi}_r^2$

The implementation of the new rotation vectors in equation 5.31 permits the following serious simplification

$$\underbrace{\boldsymbol{\phi}_{rn}^{i\top} \left(\frac{\Delta \mathbf{K}}{\Delta s} \right) \boldsymbol{\phi}_{rn}^l}_{b^{il}} + \underbrace{a^{jk} (\boldsymbol{\phi}_{rn}^i \cdot \boldsymbol{\phi}_{rn}^j)}_{\delta_{ij}} \underbrace{(\boldsymbol{\phi}_{rn}^k \cdot \boldsymbol{\phi}_{rn}^l)}_{\delta_{kl}} = 0, \quad \forall i, j, k, l \in \{1..n_r\}. \quad (5.38)$$

The final result can be found by a further straightforward reformulation

$$a^{il} = -b^{il}, \quad \forall i, l \in \{1..n_r\}. \quad (5.39)$$

Under the assumption of orthonormal vectors $\boldsymbol{\phi}_{rn}^i$ the computation of the modification parameter a_{il} is reduced to a matrix vector product and a scalar product between two vectors. Of course, one has to provide the orthonormal vectors. Nevertheless, this approach is much more efficient than the solution of a 6x6 system of equations. Finally, the modified stiffness matrix derivative $\Delta \mathbf{K}^*$ follows from equation 5.29.

5.4 Application to 3-d Model Problems

Three dimensional shell elements with Reissner-Mindlin kinematics are used to discretize the model problems of the following sections. The basic properties of the shell formulation are briefly introduced subsequently.

As it is well known shell models of the Reissner-Mindlin type can be used to analyze thin to moderate thick shells because shear deformation is considered. The technical advantage of this type of shell elements is that displacement and rotation fields are discretized independently which allows for simple shape functions of only C_0 continuity for the prize of shear locking problems. To avoid those additional considerations have to be made. Here, the Enhanced Assumed Strain (EAS) method is used which is a powerful and general approach to fix several geometrical locking phenomena, c.f. [Kos04].

The Reissner-Mindlin shells employed here are formulated by 6 degrees of freedom per node. Three translations of the shell midplane are completed by three displacements of the shell director. Figure 5.9 shows the definition for a single node P . The nodal translations are called u_x , u_y and u_z . The deformation of the director from the initial configuration $\mathbf{A3}$ to the current configuration $\mathbf{A3}^d$ is governed by the degrees of freedom α , β and γ . One

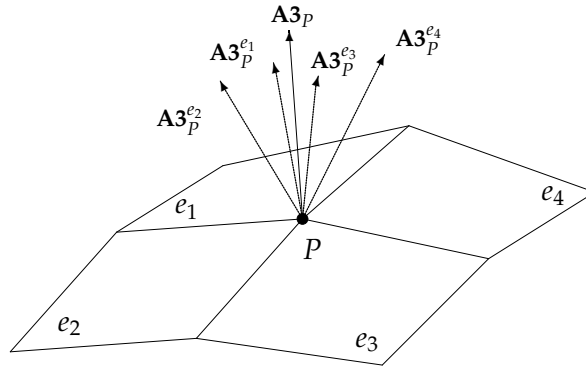


Figure 5.8: Interpolated director

crucial point is the definition of the director. In general, the surrounding elements e_k around a node P contribute to the direction of the normal at this node which gives rise to the following equation:

$$\mathbf{A3}_P = \frac{\sum_{k=1}^{nae} \mathbf{A3}_P^{e_k}}{|\sum_{k=1}^{nae} \mathbf{A3}_P^{e_k}|} \quad (5.40)$$

The parameter nae specifies the number of neighboring elements to node P . Figure 5.8 shows a graphical interpretation of equation 5.40. The unique director $\mathbf{A3}_P$ is computed by the normals of the neighboring elements $\mathbf{A3}_P^{e_i}$ with $i \in \{1 \dots nae\}$. Here the parameter nae is equal to four. Consequently

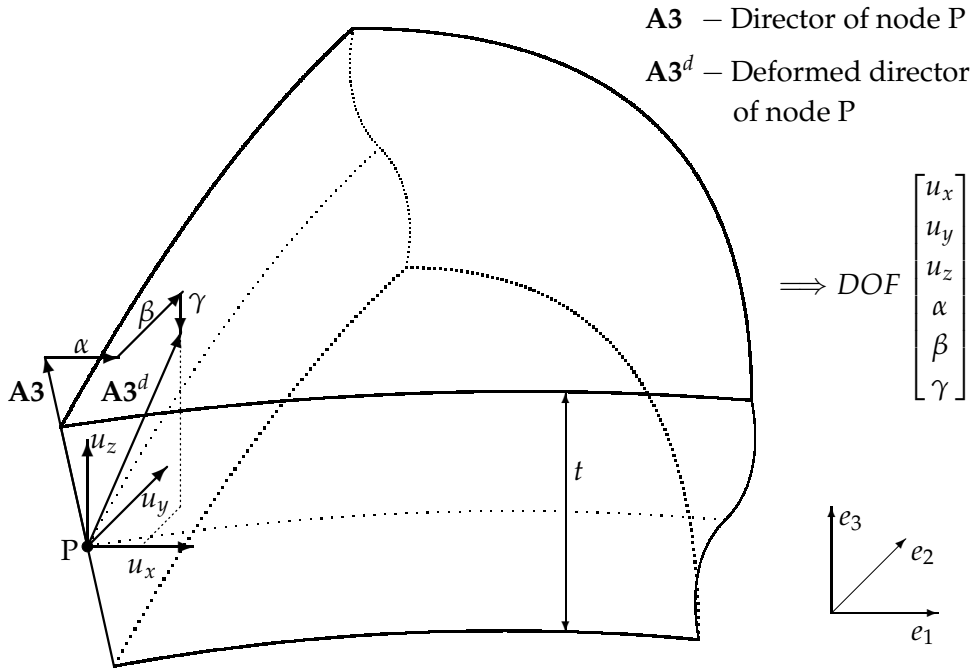


Figure 5.9: Nodal DOF of a 6 parameter Reissner-Mindlin shell

the stiffness matrix of a shell element depends on the directors of the element nodes which in turn are affected by the coordinates of the surrounding nodes. A more detailed description of this shell formulation can be found in [Bis99] and the references therein.

Because of the complex relation to system degrees of freedom the analytical sensitivity of the element stiffness matrix is very cumbersome to determine. The suggested semi-analytical approach appears to be exact and significantly more efficient at the same time.

5.4.1 Sensitivity Analysis

The derivatives of the applied objective (3.32) with respect to the design variable are computed by a semi-analytical (SA), an exact semi-analytical (ESA) and a global finite difference (GFD) formulation. The GFD of the compliance F with respect to the design variable s serves as reference result. It is computed by

$$\frac{dF}{ds} \approx \frac{F(s + \Delta s) - F(s)}{\Delta s} \longrightarrow \Delta F^{GFD}. \quad (5.41)$$

The basis for the formulation of the semi-analytical derivative is given by equation 4.9. Here the analytical derivative of the stiffness matrix is approximated by a finite difference formulation:

$$\begin{aligned}\frac{dF}{ds} &\approx -\frac{1}{2}\mathbf{u}^T \frac{\mathbf{K}(s + \Delta s) - \mathbf{K}(s)}{\Delta s} \mathbf{u} \\ &= -\frac{1}{2}\mathbf{u}^T \frac{\Delta \mathbf{K}}{\Delta s} \mathbf{u} \quad \longrightarrow \quad \Delta F^{SA}.\end{aligned}\quad (5.42)$$

Again, the semi-analytical derivatives show the errors mentioned in section 5.2. The stiffness matrix derivative is modified as shown in section 5.3 to give exact semi-analytical derivatives. They are computed by

$$\frac{dF}{ds} \approx -\frac{1}{2}\mathbf{u}^T \Delta \mathbf{K}^* \mathbf{u} \quad \longrightarrow \quad \Delta F^{ESA}, \quad (5.43)$$

with $\Delta \mathbf{K}^*$ according to equation 5.29.

The examples of the following sections are chosen to show the behavior of the semi-analytical and the exact semi-analytical sensitivities compared to the global finite differences. They consider simple cantilever problems comparable to the motivation examples presented in section 5.2.

The basic goal of the following examples is to investigate the approximation errors of the semi-analytical and the exact semi-analytical approach. GFD results of both formulations serve as reference solution. The semi-analytical and the exact semi-analytical sensitivities are scaled by the GFD results to obtain the graphs of the subsequent diagrams:

$$\Delta F_{scal}^{SA} = \frac{\Delta F^{SA}}{\Delta F^{GFD}} \quad \text{and} \quad \Delta F_{scal}^{ESA} = \frac{\Delta F^{ESA}}{\Delta F^{GFD}}. \quad (5.44)$$

5.4.2 Model Problem III

The third model problem of this chapter treats a cantilever beam of length $L_b = 1$. The width and the thickness are specified by 1.0 and 0.1 respectively. The beam is clamped at $x = 0$ and loaded by a static nodal load $f = 2f^1 + 5f^2 = 1$ with $f^2 = 2f^1$ at $x = L_b$. Kinematics and material law are defined by linear formulations. Rectangular shell elements with Reissner-Mindlin kinematics are used to discretize the structure. The geometry of the cantilever is fixed but the number of elements varies for the subsequent investigations. The number of elements in length direction is modified between 1 and 16, but the number of elements in width direction remains constant. Figure 5.10 shows an example with 3 element rows in length direction.

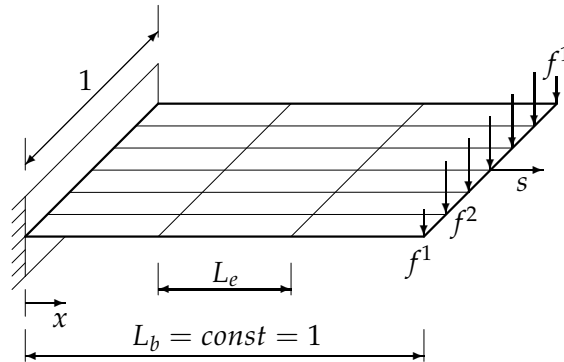


Figure 5.10: Model Problem III

This example considers the influence of a tip perturbation Δs for a decreasing element edge length. Here, the perturbation is constant over the tip of the beam. The perturbation is computed by $\Delta s = p$ with $p = 1 \cdot 10^{-05}$. Table 5.1 shows the corresponding edge length of the elements L_e , the per-

n	L_e	Δs	$\Delta s/L_e$
1	1	1E-05	1E-05
2	0.5	1E-05	2E-05
4	0.25	1E-05	4E-05
8	0.125	1E-05	8E-05
16	0.0625	1E-05	1.6E-04

Table 5.1: Perturbation parameters for MP III

turbation Δs and the relation between perturbation and characteristic element length for the increasing number of elements. This relation becomes larger as the number of elements increases. The influence of the factor $\Delta s/L_e$ on the sensitivities is visualized in figure 5.11. It shows the scaled semi-analytical and exact semi-analytical sensitivities. It becomes obvious, that the semi-analytical sensitivities show a linearly increasing error. The source of this error is the increasing factor $\Delta s/L_e$. Another problem formulation where this factor would be kept constant does not show such a error propagation. The graph of the exact semi-analytical sensitivities does not show any difference to the reference result. Thus, the sensitivity errors of this model problem are completely cured.

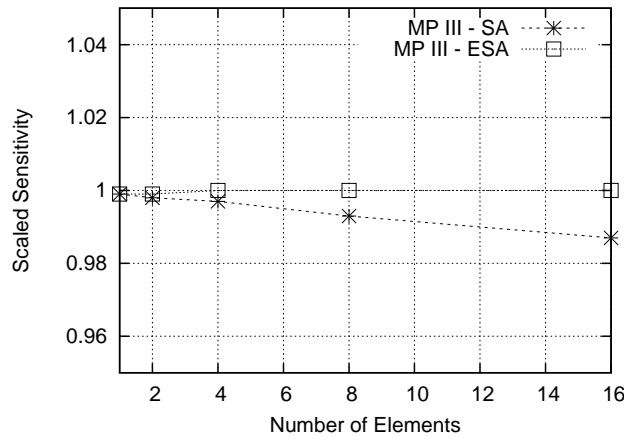


Figure 5.11: Scaled sensitivities for Model Problem III

5.4.3 Model Problem IV

The next example is also related to a cantilever beam. It is also clamped at $x = 0$ but loaded by nodal forces $f(n) = 2f^1(n) + 5f^2(n)$ with $f^2(n) = 2f^1(n)$ at $x = L_b$. The applied elements are equal to Model Problem III, also the number of elements n varies between 1 and 16 ($n \in \{1..16\}$). In contrast to the former examples the length of the beam increases by the number of elements, because the length of the elements remains constant ($L_e = 1.0$). The goal of this model problem is the investigation of the in-

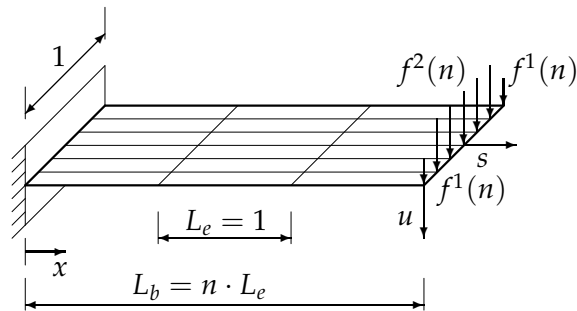


Figure 5.12: Model Problem IV

fluence of an increasing beam length on the approximation of the sensitivities. Obviously, the displacement field influences the sensitivities obtained by equations 5.41, 5.42 and 5.43. Hence, the results are not comparable for

an increasing beam length due to the increasing deformation. To disable the influence of an increasing displacement field on the results one has to ensure that the tip displacement remains constant. This prerequisite demands a decreasing tip load $f(n)$ for an increasing beam length L_b . The linear Euler-Bernoulli beam theory results in the following equation for the tip displacement of a cantilever beam subjected to a tip load:

$$u = \frac{f \cdot L_b^3}{3 \cdot EI}. \quad (5.45)$$

Enforcing u to be constant, the load for an arbitrary beam length follows from

$$f = \frac{3 \cdot EI \cdot u}{L_b^3}. \quad (5.46)$$

The resulting tip loads $f(n)$ for the specific beam lengths $L = n \cdot L_e$ are listed in table 5.2.

L_b	Tip Load f
1	1
2	0.125
4	0.015625
8	0.001953
16	0.000244

Table 5.2: Tip load $f(n)$

n	L_e	Δs	$\Delta s / L_e$
1	1.0	1E-05	1E-05
2	1.0	1E-05	1E-05
4	1.0	1E-05	1E-05
8	1.0	1E-05	1E-05
16	1.0	1E-05	1E-05

Table 5.3: Perturbation for MP IV

The perturbation Δs is computed by $\Delta s = p \cdot L_e = p \cdot 1.0$. Hence, the perturbation as well as the relation between perturbation and element length are independent of the beam length as listed in table 5.3. The scaled sensitivities for Model Problem IV are depicted in figure 5.13. Obviously, the error in the semi-analytical sensitivities increases quadratically with an increasing beam length. This behavior could be expected because the graphs in figure 5.5 show a similar behavior. These two figures can be compared because the configuration of Model Problem II is nearly equivalent to Model Problem IV, except of the element types.

The graph of the exact semi-analytical sensitivities indicates that the proposed correction method effectively eliminates the undesired effects.

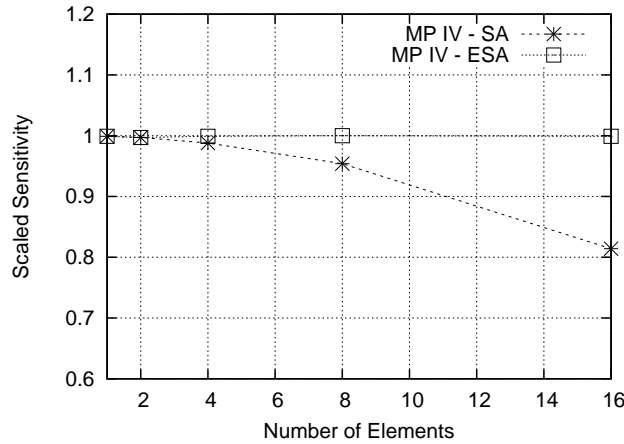


Figure 5.13: Scaled sensitivities for Model Problem IV

5.5 Summary

Influence of element type, element length and element rotation on the computation of semi-analytic sensitivities are investigated by the examples of this section. Additionally, the performance of the correction method introduced in section 5.3 was demonstrated. Based on the results of Model Problems I - IV the following statements are made.

- The accuracy problems of the semi-analytic sensitivities depend on the kinematic assumptions of the elements. Elements with the same kinematics like Euler-Bernoulli beams and Kirchhoff shells as well as Timoshenko beams and Reissner-Mindlin shells behave analogously.
- The crucial factor for the accuracy of the approximated derivatives is the ratio between perturbation and element length ($\Delta s/L_e$). If the ratio is small enough, even the semi-analytical sensitivity analysis might be good enough.
- In most cases the results of the exact semi-analytical sensitivity analysis are nearly identical with the analytical solutions. The only error which remains in the derivatives is the approximation error of the finite difference formulation. This error can not be avoided.
- The numerical effort for the modification of the stiffness matrix derivative is negligible due to the orthogonalization of the rotation vectors.

-
- Further approaches for the elimination of errors in semi-analytical design sensitivity analysis are based on higher order approximations, e.g. central differences. The crucial disadvantage of these methods are additional perturbation steps which lead to an increasing computation time.
 - The procedure to compute the improved approximation of the stiffness matrix derivative is independent from the specific FE-formulation. The only information which is necessary is the definition of the nodal degrees of freedom to specify a set of rigid body rotation vectors. Thus, the method is applicable to all kind of Finite Elements without significant implementation effort.

Chapter 6

Regularization of Shape Optimization Problems

It is well known [HG92], [BWDC05] that structural optimization problems formulated on large design spaces require regularization methods to achieve reliable results. Coarse parametrization methods like CAGD or Morphing are one possibility to regularize the optimal results. Obviously, the optimal result is limited by such coarse parametrizations. FE-based parametrizations necessarily require regularization methods to ensure reliable mesh independent results and to satisfy e.g. manufacturing or aesthetic constraints. These regularization methods can be separated into out-of-plane regularization and in-plane regularization. The out-of-plane regularization is applied to the source of the design update namely the response gradients, c.f. equation 4.28. The in-plane regularization is applied to ensure robust and reliable grids during the optimization process. Hence, these methods only change the discretization of the geometry but not the geometry itself. A more detailed motivation of the separation of design parameters can be found in section 4.2.5.

The proposed out-of-plane regularization method applied to the response function gradients is presented in section 6.2 whereas the developed in-plane regularization method is introduced in section 6.3.

6.1 Motivation

As introduced before the necessity of out-of-plane regularization is based on non-smooth response function gradients. Independently of the type of differentiation (analytical, semi-analytical or global finite difference) the gradients are not smooth. In this context the term "smooth" is related to a geometrical curvature measure because in shape optimization problems

the smoothness of the gradients directly affects the smoothness of the geometry. If the gradients are not smooth the geometry in the next optimization step will be also not smooth. Obviously, a disturbed geometry will cause non-smooth gradients again. Without out-of-plane regularization this procedure continues until the whole mechanical model is irregular. Since the separation in large or small curvatures is highly problem specific it is impossible to specify a fixed allowable curvature limit. Hence, the out-of-plane regularization method must be able to influence the curvature of the gradient fields by a simple and robust approach.

There exist several reasons for the development of non-smooth gradient fields. In general, this effect is caused by mathematical properties of the underlying function spaces, by kinematics and load carrying behavior of the specific mechanical model and by deficiencies of the applied finite element formulations:

- The derivatives of response functions (objectives and constraints) are not as smooth as the functions itself. This is caused by the fact that the derivatives of a function exhibit larger local curvatures than the function itself. There exist only few exceptions from this statement e.g. trigonometric functions. A more detailed introduction into this topic can be found in [MP05]
- Especially for stiffness maximization of shell structures there exists an intrinsic interaction between local and global improvements of the objective. This results in local regions with high curvatures (local stiffeners like beads) and other regions with nearly flat geometries.
- The applied finite elements may also abet non-smooth gradient fields. This is caused by incorrect element responses, e.g. if the elements suffer from locking phenomena. Unstructured grids with different element aspect ratios may also show such an behavior. These effects can be decreased by application of elements which give reliable responses (hybrid elements, EAS elements [Cam04]) or by grids with reasonable element aspect ratios.

The above mentioned observations of shape optimal finite element models are well known since many years. In industry this problem is solved by CAD approaches with coarse geometry models. Hence, the maximum curvature of the geometry is limited by the CAD model. It is obvious that the improvement of the applied objective is also limited by the coarse geometry model. However, there exist several approaches to overcome the

problem of non-smooth gradient fields. They are mostly applied to FE-based optimization strategies and are able to improve the smoothness of the gradients.

Mohammadi [Moh97] as well as Jameson and Martinelli [JM98] propose a local smoothing operator which projects the disturbed gradient fields to a C^1 continuous gradient field. This is realized by repeated solution of the following system of equations:

$$(\mathbf{I} - \epsilon \nabla) \frac{d\tilde{f}}{ds_l} = \frac{df}{ds_l} \quad (6.1)$$

with the non-smooth derivatives $\frac{df}{ds_l}$ and the projected derivatives $\frac{d\tilde{f}}{ds_l}$. The parameter ϵ controls the end of the iteration procedure by setting $\epsilon = 0$ if the convergence criterion is reached. The term $\nabla \frac{df}{ds_l}$ specifies the curvature of the objective function, which is eliminated by the above mentioned iterative procedure. Mohammadi, Jameson and Martinelli apply this local second order projection method for shape optimization of fluid problems. In such applications the appearance of shock fronts yields to locally irregular gradient fields.

Azegami and Kaizu [AK07] developed the so called "Traction Method". The aim of this method is to compute a smooth gradient field by solution of a linear elastic boundary value problem defined in the original domain and loaded with the non-smooth gradient field. The authors note that application of this method is possible to shape as well as to topology optimization problems. Additionally this method decreases the size effect of the parametrization presented in section 4.5.

Bendsøe and Sigmund [BS03] propose a so called sensitivity filter to decrease the mesh dependency of topology optimization problems. Within this approach the sensitivity of a single design variable is modified by a weighted average of the sensitivities in a fixed neighborhood

$$\frac{\partial \tilde{f}}{\partial s_l} = \frac{1}{s_l \sum_{m=1}^N \tilde{H}_m} \sum_{m=1}^N \tilde{H}_m s_m \frac{\partial f}{\partial s_l}, \quad (6.2)$$

where N is the number of elements in the filter domain. Bendsøe and Sigmund define the weight factor (convolution operator) as

$$\tilde{H}_m = r_{min} - dist(l, m). \quad (6.3)$$

The parameter r_{min} controls the radius of the filter operator and $dist(l, m)$ specifies the distance between element l and element m . Elements m with

$dist(l, m) > r_{min}$ are not considered in the smoothed gradient of element l . The authors apply this method to topology optimization problems with the SIMP approach which treats the density of element l as design variable s_l . Although the authors do not provide a mathematical prove of this methods it produces robust results with only a little amount of extra CPU time.

Materna and Barthold [MB08] apply a method based on configurational forces e.g. for in plane mesh regularization. Here, they compute variational sensitivities for the internal potential energy with respect to the coordinates of the finite element nodes. The final result of the procedure is a grid that provides a lower internal energy for the mechanical model and hence a more accurate result.

The Poisson regularization is often applied in reconstruction of measured surface data [AN07], e.g. by laser scanning methods and in image processing. In the context of surface reconstruction the data suffer from noise which is unavoidable in measuring processes. This noise is eliminated by application of the Poisson equation which includes the Laplace operator. Application of the Laplacian to the measured data extracts the local curvature which is sequentially reduced by an update scheme. One crucial point in such applications is the detection of sharp edges which must not smoothed out.

6.2 Projection of Sensitivities

In this section a robust, efficient and reliable projection method for non-smooth gradient fields is presented. The method is based on the mathematical theory of convolution integrals which is well known since many years.

In order to show the tremendous effects of multimodal response functions on the gradient fields the simple one dimensional function depicted in figure 6.1 is applied. It shows the function $f(x) = (x - 2)^2$ which is called "Basic Response". This function is disturbed by the noise function $n(x) = 0.3 * \sin(5x)$. The sum $f_d(x) = f(x) + n(x) = (x - 2)^2 + 0.3 * \sin(5x)$ gives a "Disturbed Response" also visualized in figure 6.1. The effect of the noise function $n(x)$ increases tremendously after differentiation of f and f_d . The derivative of the Basic Response ($df(x)/dx = 2x - 4$) shows a completely different behavior compared to the derivative of the Disturbed Response ($df_d(x)/dx = 2x - 4 + 1.65 * \cos(5.5x)$). The former one shows constant slope and no curvature whereas the latter one exhibits large differences in

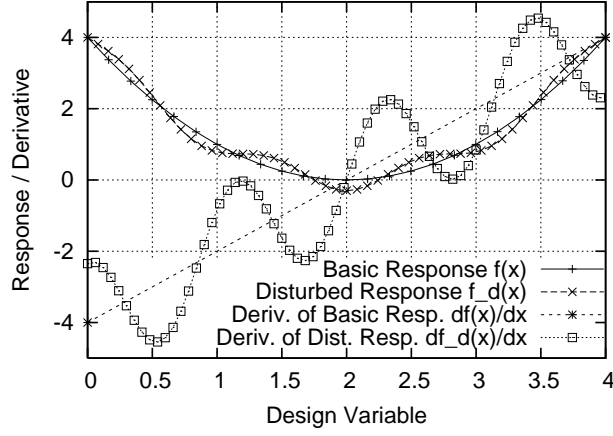


Figure 6.1: Objective with noise

slope and curvature. It is easy to observe that gradient based optimization strategies suffer seriously from such wavy gradient fields.

This simple example motivates the development and emphasizes the crucial importance of filter methods for gradient based optimization schemes. In general, small perturbations of response functions can not be prevented, e.g. due to the approximating character of FE-models. After differentiation of these response functions the error dominates the whole gradient field and actually prevents accurate design updates. These disturbed design updates often point to local minima with poor structural properties. Since the errors are much more visible in the gradients fields than in the function itself the filter method is conveniently applied to the gradient fields. This motivation shows that regularization techniques are necessary for FE-based parametrization schemes in order to ensure robust and stable optimization methods and best possible results.

6.2.1 Theory of Convolution Integrals

The proposed projection or smoothing operator is based on convolution [Yos80] of the disturbed gradient field df_d/ds_i with a filter function g written as $df_d/ds_i * g$. It is defined as the integral of the product of these functions:

$$\frac{df}{ds_i} = \left(\frac{df_d}{ds_i} * g \right)(s_i) = \int_{R^n} \frac{df_d}{ds_i}(s_i - \tau)g(\tau)d\tau, \quad (6.4)$$

whereas R^n represents the n dimensional domain of the filter function and τ states as local variable of g . For shell optimization problems the gradient

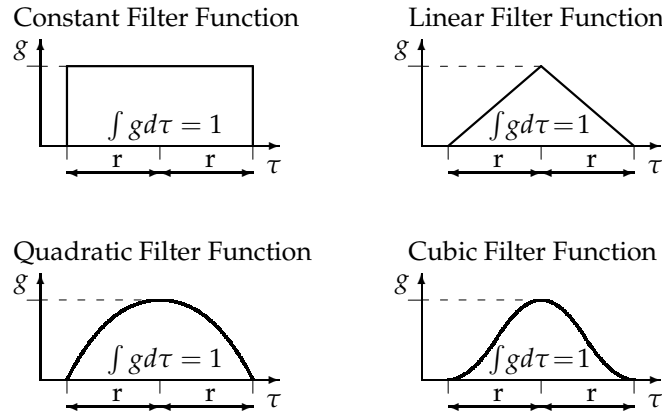


Figure 6.2: Filter functions

field $df_d ds_i$ as well as the filter function g are 2-d functions. Hence, the convolution of these functions is defined by integration over the area of the filter function g . An application of this approach to 3-d models (discretized by bricks) needs a volume integral.

The filter function g can be considered as a mollifier with several characteristic properties. It is non negative, has compact support and the integral $\int g d\tau$ is equal to 1. In mathematics mollifier functions are also infinitely often continuously differentiable. For application as filter function for non-smooth gradient fields this property is not necessary. Further important properties of convolution integrals are commutativity $f * g = g * f$, associativity $f * (g * h) = (f * g) * h$, associativity with scalar multiplication $a(f * g) = (af) * g = f * (ag)$ and the differentiation rule $D(f * g) = Df * g = f * Dg$. The support of the smoothed function df/ds_i is slightly enlarged compared to df_d/ds_i , cf. Figure 6.5. Additionally, the difference in L_1 norm between the original and the smoothed function is bounded by a positive constant.

Example I

The first example shows the application of four filter functions (constant, linear, quadratic, cubic) and three filter radii (0.25, 0.75, 1.25) to smooth the derivative of the disturbed response $df_d(x)/dx$ presented in figure 6.1. The filter functions are sketched in figure 6.2. The filter functions are symmetric and they are defined over the domain $2r$. In general, also exponential functions are applicable as filter functions. In contrast to simple polynomials such functions are infinitely often continuously differentiable.

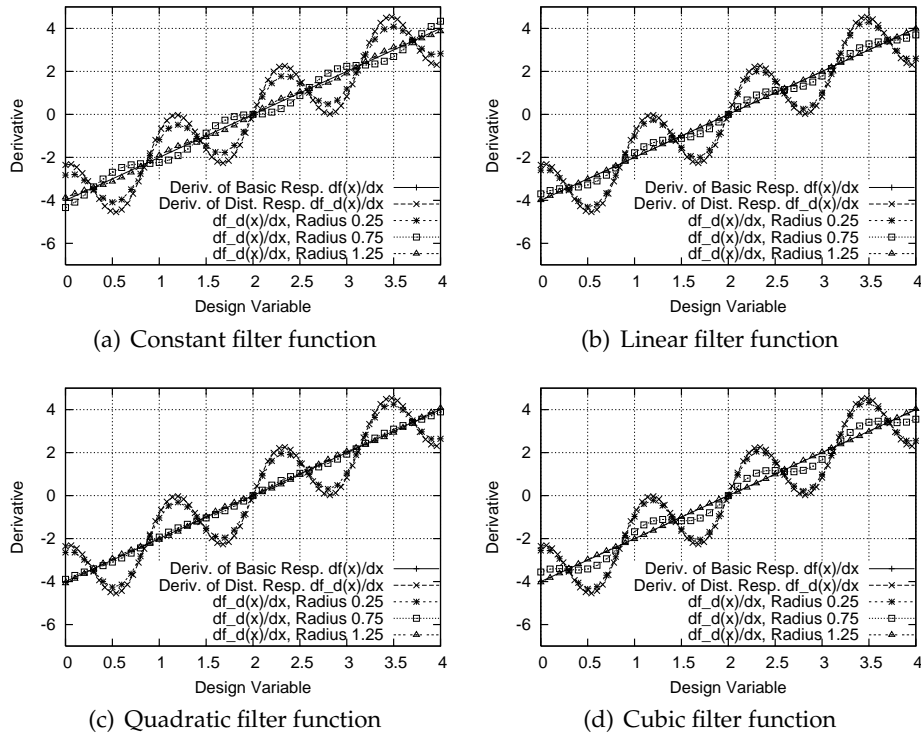


Figure 6.3: Smoothed sensitivities

Figure 6.3 shows the results of application of the four types of filter functions to the disturbed derivative function (figure 6.1). In general, all filter functions are able to smooth the gradient function effectively. Obviously the disturbed function $df_a(x)/dx$ becomes smoother if the filter radius of the filter functions becomes larger. This is shown exemplary by the graphs of the filter radius $r = 0.75$. Very good correlation is observed for all filter functions if the filter radius is increased to $r = 1.25$. However, for this kind of periodic noise function the graph of the constant filter function (figure 6.3a) shows minimal oscillations. Obviously the obtained results depend on the kind of basic response and noise function. Application of other noise functions may yield to slightly different results but the influence of noise effect is decreased seriously.

6.2.2 Application as Filter Function

The filter method introduced in (6.4) is defined for continuous functions. In finite element analysis only discrete function values at the nodes are available. The reformulation of the convolution integral to discrete values

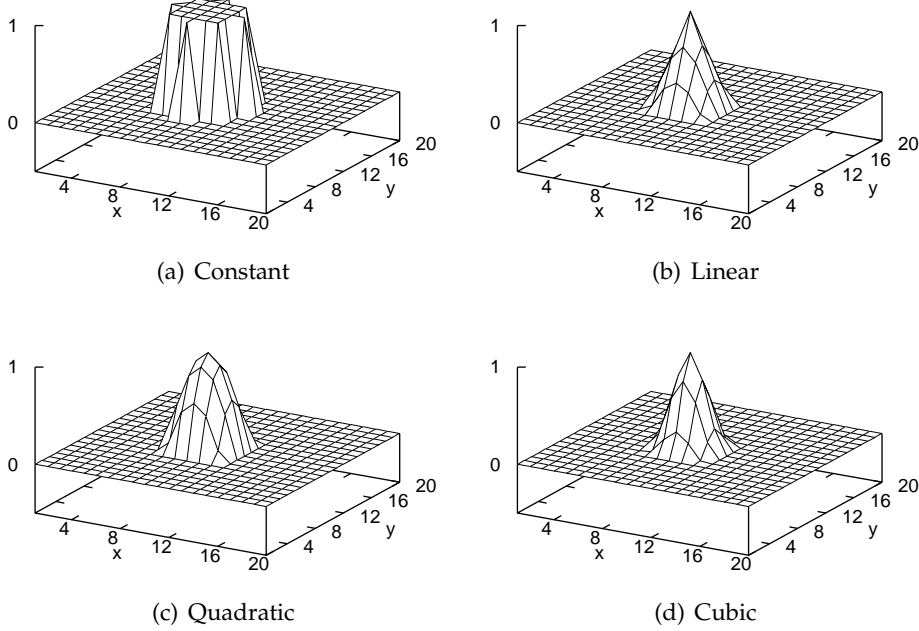


Figure 6.4: 2-d Filter functions with radius $r=3$

$df_d/ds_i, g : D$ with $D \subseteq \mathbb{Z}$ reads as

$$\frac{df}{ds_i} = \left(\frac{df_d}{ds_i} * g \right)(s_i) = \sum_{k \in D} \frac{df_d}{ds_i}(s_i - k)g(k) \quad (6.5)$$

For smoothing of discrete response functions of finite element models the set D is defined by the set of optimization variables at finite element nodes.

According to the 1-d filter functions depicted in figure 6.2 the respective 2-d functions are drawn in figure 6.4 for filter radius $r = 3$. Obviously, the integral of the several filter functions is not equal to 1. This is considered by a scaling of the RHS of equation (6.5) with $1 / \int g d\tau$.

Example II

Figure 6.5 visualizes a basic property of smoothing operations by convolution namely the enlarged support of the smoothed function. The two dimensional and constant function f_c in figure 6.5a has the value 1 in the domain $6 < x < 15, 6 < y < 15$ and the value 0 elsewhere. The function f_s plotted in figure 6.5b is obtained by convolution of f_c with a linear filter function with radius equal to 3 (cf. figure 6.4b). The result shows a clear smoothing in the support region of function f_c . But the convolution yields to an enlarged support of function f_s . This function has nonzero values in

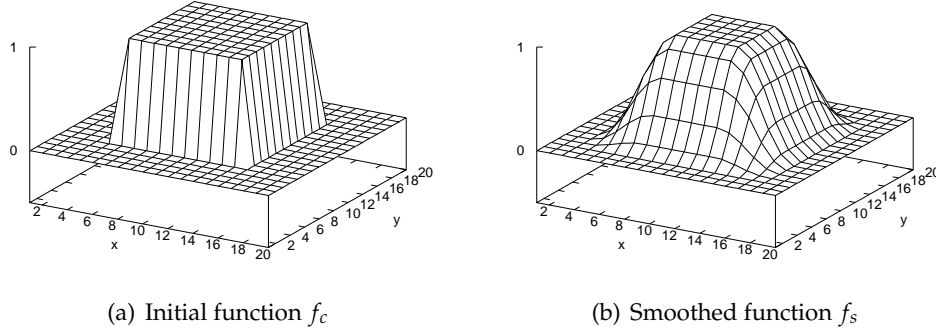


Figure 6.5: Enlarged support due to smoothing operator

the domain $4 < x < 17, 4 < y < 17$. In general, the size of the enlarged support depends on the radius of the filter function, a large filter radius yields to a big shift in the support region and vice versa. For applications to optimization problems this effect becomes visible near the boundary of the gradient field because the design space of a mechanical model is limited and, hence, the enlarged support of the sensitivity field can not be modeled by this space.

Example III

The last example of this section shows the application of 2-d filter functions to a mathematical model problem. Figure 6.6a shows a biquadratic example function defined over the domain $l_x \leq x \leq L_x, l_y \leq y \leq L_y$ with $l_x = l_y = 1$ and $L_x = L_y = 20$ by

$$f_{bq}(x, y) = \frac{2650((x - L_x)(x - l_x)(y - L_y)(y - l_y))^2}{L_x L_y (L_x L_y - 2L_x - 2L_y + 4)} \quad (6.6)$$

This function has the value 0 at $x = 1 \wedge x = L_x \forall y \in \{l_y..L_y\}$ and at $y = 1 \wedge y = L_y \forall x \in \{l_x..L_x\}$. The function reaches its maximum at $x = L_x/2 \wedge y = L_y/2$. A random function $f_{rand}(x, y) = rand\{-1..1\}$ defined over $l_x < x < L_x, l_y < y < L_y$ is added to (6.6) to simulate the noise which is contained in the sensitivity fields of mechanical response functions. The sum $f_{bq} + f_{rand} = f_{bq}^n$ is shown in figure 6.6b. The global characteristics of the basic function f_{bq} (e.g. global maximum) are also visible in the disturbed function, but local information cannot be extracted from it.

Like in Example I constant, linear, quadratic and cubic filter functions with a variable filter radius are applied to smooth the disturbed function. The goal is to obtain the best approximation of f_{bq} by smoothing the function f_{bq}^n . The resulting functions are called $f_{filt,r}^s$ for the four different filter functions $filt \in \{constant, linear, quadratic, cubic\}$ and the filter radii

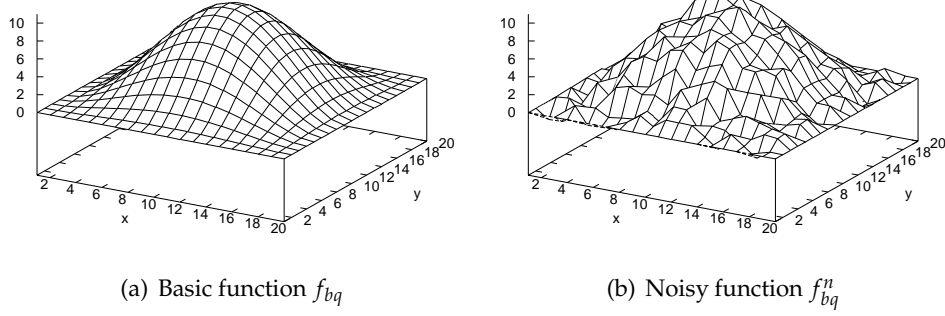


Figure 6.6: 2-d Quadratic example function

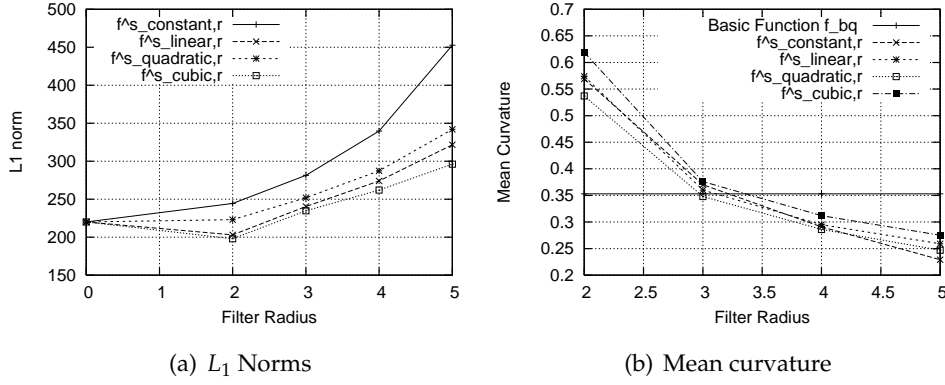


Figure 6.7: Error propagation of Example III

$r \in \{1,2,3,4\}$. The quality of the smoothed functions is measured by three performance criteria.

- the L_1 norm of the difference between the basic function f_{bq} and the result of the filtering process $f_{filt,r}^s$
- the mean of mean curvature of the nodes of $f_{filt,r}^s$ where the sum of mean curvature of all nodes is divided by the number of nodes,
- and the maximum mean curvature of $f_{filt,r}^s$.

The L_1 norm, equation 6.7, of the difference between the smoothed result and the basic function f_{bq} shows for all types of filter functions ($func$) a similar behavior with only minor differences, cf. figure 6.7a.

$$N_{L_1}^{r,func} = \sum_x \sum_y |f_{bq}(x,y) - f_{filt,r}^s(x,y,func)| \quad (6.7)$$

The linear and the cubic filter functions with a radius of 2 are able to decrease the error. For the quadratic filter function the error remains constant and for constant filter function the error becomes larger. With an further increasing filter radius r the L_1 norm increases also. This is caused by the fact that a small part of the basic response is smoothed out by the filter function. This small part can be considered as the smoothing error. The amount of smoothing error is related to the size of the filter radius. The different graphs in figure 6.7a show that the type of filter function has also influence on the smoothing error. The best results in terms of the L_1 norm are obtained by cubic filter functions where constant filter functions yield to worst results. In general, the smoothing error can not be measured directly because the basic function (without noise) is usually not known.

Figure 6.7b shows the mean curvature of the basic function (constant graph) and the mean curvatures of the smoothed functions. Also in this figure the graphs of the different filter functions show a similar behavior. All four filter functions are able to reduce the mean curvature in the result efficiently. For filter radii $r \geq 4$ the mean curvature of the smoothed results is smaller than for the basic function. This phenomenon is also caused by the smoothing error because the high curvature regions of the basic response f_{bq} are partially smoothed out.

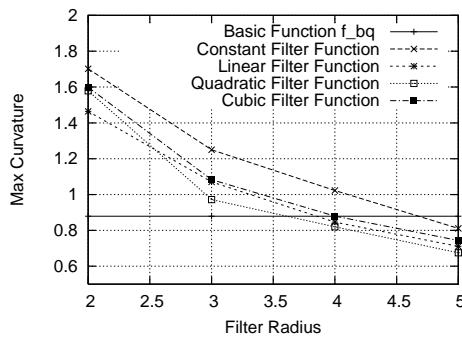


Figure 6.8: Max. mean curvature

The third criterion to be evaluated is the maximum mean curvature shown in figure 6.8. The basic response function f_{bq} has a maximum mean curvature of 0.88. The resulting curvature values for the smoothed functions show a similar behavior. An increasing filter radius r gives a decreased mean curvature where the linear, quadratic and cubic filter functions reach the value of the basic function for $r = 4$. The curvature reduction of the constant filter function is not as effective as for the other filter functions.

Based on the results visualized in figures 6.7a, 6.7b and 6.8 $f_{cubic,A}^s$ is the best agreement between good approximation of basic response function f_{bq} and smoothing of the noise.

The smoothed function $f_{cubic,A}^s$ depicted in figure 6.9b shows a very good correlation to the basic function f_{bq} . The basic properties of f_{bq} like max-

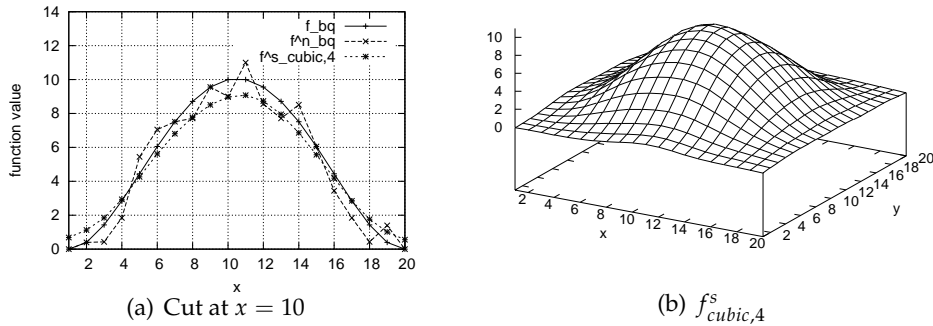


Figure 6.9: Smoothing results

imum at $x = 10, y = 10$ and $f_{bq} = 0$ at the support are also reflected by $f_{cubic,4}^s$. This can be identified in more detail in figure 6.9a. This diagram shows the function values of f_{bq}, f_{bq}^n and $f_{cubic,4}^s$ along the cutting line at $x = 10$. The graph of $f_{cubic,4}^s$ is not influenced by the noise function and shows only minor differences to f_{bq} . But near the boundary at $x = 0$ and $x = 20$ the mentioned boundary effect (cf. Example III) is also contained in the smoothed result. Nevertheless, the filtered function $f_{cubic,4}^s$ is a good approximation of f_{bq} that eliminates the disturbing influence of the noise very effectively.

The application of convolution integrals as filter method for disturbed gradient fields yields to smooth sensitivity distributions which can be directly utilized for the design update. But near the boundary or in regions with high curvatures the smoothing error prevents exact approximations of the gradients if the filter radius is too large. This problem can be reduced by multiple filter operations with a smaller filter radius. Another modification of the original filter algorithm is the application of elliptical filter functions near the boundary. By this method the enlargement of the support can be decreased significantly.

6.3 Mesh Regularization

In contrast to the out-of-plane regularization method introduced in the previous section the mesh regularization is denoted as in-plane-regularization method. The basic goal is to ensure robust and reliable FE-meshes in order to disturb the direct sensitivity analysis as less as possible.

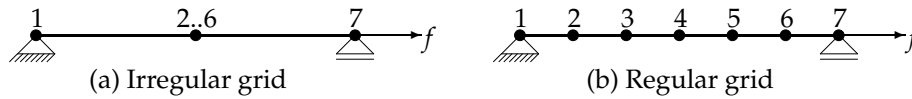


Figure 6.11: "Optimal" Solutions

6.3.1 Motivation

Figure 6.10 shows the initial configuration of a simple beam optimization problem. The circular structure is supported at nodes 1 and 7 and loaded by a force f at node 7. The optimization goal is stiffness maximization for the given boundary conditions where the straight connection between nodes 1 and 7 is the optimal solution. The optimization variables are the normal nodal coordinates of nodes 2..6. Now, it is assumed that the direction of the design variables remains constant during the optimization procedure. Obviously, there exists an arbitrary number of discretizations to represent the optimal geometry. Two possible meshes are depicted in figures 6.11a and 6.11b.

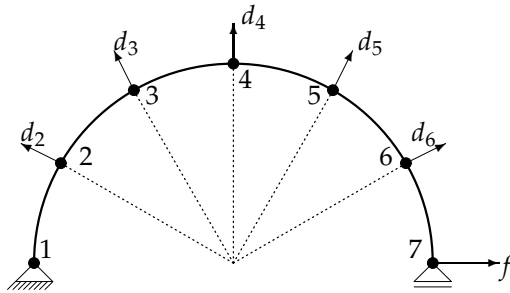


Figure 6.10: Initial configuration

In 6.11a the nodes 2..6 are coalesced at the center of the structure. Thus, the length of the inner elements tends to zero and the length of the outer elements tends to the radius of the initial configuration. Therefore, the geometry of the optimal solution is correct but the mechanical model

is irregular. However, this discretization is the result of the optimization problem with the specified assumptions. Obviously, the optimization strategy has to be supplemented with an in-plane regularization method to avoid such irregular results. Another optimal solution is presented in figure 6.11b. It also shows the correct geometry but now with a feasible mechanical model. This result is obtained by the in-plane regularization approach introduced in section 6.3.4. Within this method the necessary mesh adaption is distributed over the whole model. This ensures stable element aspect ratios and therefore robust and reliable results.

Based on this simple example the basic properties of a mesh regularization method can be stated. Each mesh regularization method should improve

the mesh quality and it has to preserve the geometry. This leads to methods that allow for a floating FE mesh over the geometry managed by suitable projection operators. The determination of mesh quality strongly depends on the special application and the applied finite elements. In many cases the quality of quadrilaterals and hexahedrons is determined by the inner angles which should be close to 90 degrees. Triangles or tetrahedrons with good quality usually have nearly equal edge lengths.

Mesh regularization methods are distinguished in geometrical and mechanical approaches. Pure geometrical methods are based on a local criterion which improves the mesh locally. Mechanical methods solve the mesh optimization problem by an auxiliary mechanical model. Usually, both methods require the solution of an additional system of equations which requires significant numerical effort. The presented geometrical methods may also be formulated in an explicit scheme which does not require the solution of an equation system. Unfortunately, the convergence of such explicit formulations is rather poor but the application to shape optimization problems does not require too small convergence tolerances.

6.3.2 Geometrical Methods

Geometrical mesh regularization methods apply a local criterion for mesh improvement. A famous class of geometrical methods are the Laplace smoother [ZTZ00]. These methods are based on the computation of the center of gravity of point clouds. Usually, they are robust and stable and require only a small numerical effort.

The basic principles and a suitable implementation should be visualized by the simple example sketched in figure 6.12. It shows a simple irregular grid spanned by the nodes n_i with $i \in \{1..10\}$. The goal of the mesh regularization is to modify the position of node n_1 denoted with \mathbf{x}_1 such that the quality of the mesh is improved.

The most simple Laplace operator is the so called Umbrella Operator. This operator determines the optimal position of an inner node by the average position of the surrounding nodes expressed by

$$\tilde{\mathbf{x}}_1^* = \frac{1}{N} \sum_{i=2}^{10} \mathbf{x}_i \quad (6.8)$$

where N denotes the number of neighboring nodes, here $N = 9$. This operator works well for regular grids spanned by triangles, quadrilaterals,

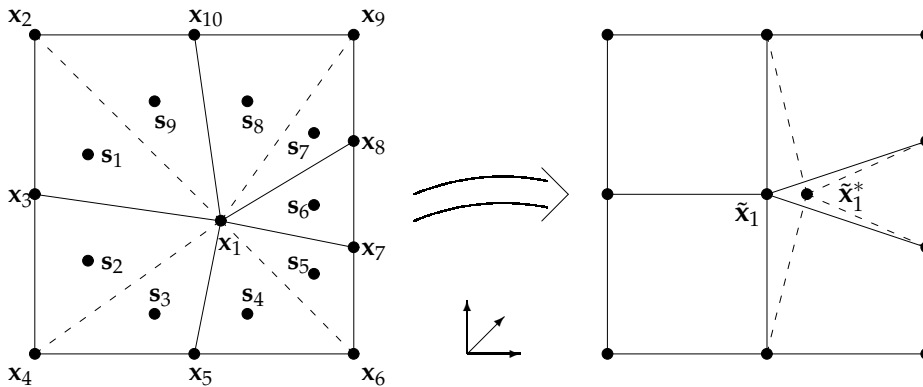


Figure 6.12: Mesh regularization by Laplace smoother

tetrahedrons or hexahedrons. It is obvious that this method fails for irregular grids. In the above sample grid this would end up in a nodal position \tilde{x}_1^* closer to the nodes n_6 and n_7 instead of the center of the grid.

A simple and robust enhancement of the umbrella operator is the inclusion of the center of gravity weighted by the area content. This modification allows for application of the umbrella operator to irregular grids. Computation of area and center of gravity for arbitrary element types is possible but not straight forward. Triangles or tetrahedrons offer a simple and very efficient computation of these data. This motivates an auxiliary triangulation of the neighborhood of node n_1 to compute area content and center of gravity by simple geometrical elements. The example grid depicted in figure 6.12 can be triangulated by 9 elements where the additional element edges are marked by dashed lines. The investigated node is member of each element which yields to element e_1 consisting of the nodes $\{n_2, n_3, n_1\}$. The optimal position of node n_1 is now computed by

$$\tilde{x}_1 = \frac{1}{N} \sum_{j=1}^9 A_j \mathbf{s}_j \quad (6.9)$$

where N denotes the number of neighboring elements and j defines a counter over these elements. The parameters \mathbf{s}_j and A_j denote the center of gravity and the area content of element e_j , respectively. It is easy to verify that this simple enhancement increases the application fields of the umbrella operator significantly. The implementation of the area content additionally offers the opportunity to consider properties of the initial discretization during the optimization process. This effectively prevents an effect called over-smoothing.

6.3.3 Mechanical Methods

In contrast to geometrical methods the class of mechanical methods formulate an auxiliary mechanical problem leading to an improved mesh. In general, two mechanical theories are applied, elasticity theory and potential field theory.

Elasticity Theory

There exist several methods to formulate mesh regularization schemes based on elasticity theory. The class of pseudo elastic continuum models consider the mesh motion at the boundary as Dirichlet boundary condition. They are often applied in Fluid Structure Interaction (FSI) problems where the fluid is described by Arbitrary Lagrangian Eulerian (ALE) methods. Here, the mesh motion of the structural boundary has to be transferred to the fluid grid. Mesh regularization methods based on elastic continuum models are limited to small mesh deformations because of large element distortions close to the Dirichlet boundary. On the other hand these methods show robust behavior at concave boundaries. Instead of modeling continua the discrete spring analogy formulates a net of discrete spring elements that connect the nodes. The springs are subjected to an initial strain and compensate boundary movements by new equilibrium states in the cable net. Usually the application of cable nets results in smaller mesh deformation at the boundaries compared to continuum models.

Another possible formulation of the discrete spring analogy is provided by the so called Force Density method [Sch74], [Lin99a], [Lin99b]. Such methods model the grid as cable net consisting of prestressed ropes. Scaling of the prestress with respect to a specified reference length results in mechanically motivated mesh regularization schemes that do not require a material formulation. In general, such methods allow for very large mesh deformations but they have problems at concave boundaries due to overlapping phenomena.

Potential Field Theory

The potential field theory is a common model to describe electric, gravitation, magnetic and aerodynamic fields, respectively. The governing equation of this theory is the Poisson equation including the Laplace operator. A basic property the modeled field is that the field lines show a very smooth and regular behavior. This motivates the application of potential field theory as mesh regularization method.

6.3.4 Minimal Surface Regularization

In this section the Minimal Surface Regularization (MSR) method is presented in detail. Basically, this method belongs to the class of mechanical mesh regularization methods. It is shown that this approach allows for large mesh deformations where the distortion of each single element is as small as possible. The theory of this method is related to the well known form finding problem ([OT62], [OS66]).

This class of problems can be investigated by experiments, by mathematics and by mechanics via the soap film analogy, the solution of the Plateau problem and by form finding of membrane structures ([BR99]), respectively. The goal of the latter approach is to find an equilibrium shape for given boundary and prestress in the domain by the governing principle of virtual work:

$$\delta w = \int_{\Omega} \boldsymbol{\sigma} : \frac{\partial(\delta \mathbf{u})}{\partial \mathbf{x}} d\Omega = t \int_a \boldsymbol{\sigma} : \delta \mathbf{u}_{,x} da = 0 \quad (6.10)$$

with the membrane thickness t which is assumed to be thin and constant, the prescribed Cauchy stress $\boldsymbol{\sigma} = \sigma^{\alpha\beta} \mathbf{g}_{\alpha} \otimes \mathbf{g}_{\beta}$ with the local directions α and β and the derivative of the virtual displacement with respect to the geometry of the actual surface $\mathbf{u}_{,x}$. The applied notation is introduced in chapter 2. Expressing $\mathbf{u}_{,x}$ by the deformation gradient

$$\delta \mathbf{u}_{,x} = \frac{\partial(\delta \mathbf{u})}{\partial \mathbf{x}} = \frac{\partial(\delta \mathbf{x})}{\partial \mathbf{X}} \cdot \frac{\partial \mathbf{X}}{\partial \mathbf{x}} = \delta \mathbf{F} \cdot \mathbf{F}^{-1} \quad (6.11)$$

permits the formulation of the form finding problem in the reference formulation

$$\delta w = t \int_A (\mathbf{F} \cdot \mathbf{S}) : \delta \mathbf{F} dA = 0 \quad (6.12)$$

where the second Piola Kirchhoff stress tensor is related to $\boldsymbol{\sigma}$ by

$$\mathbf{S} = \det \mathbf{F} \mathbf{F}^{-1} \cdot \boldsymbol{\sigma} \cdot \mathbf{F}^{-T} = \det \mathbf{F} \sigma^{\alpha\beta} \mathbf{G}_{\alpha} \otimes \mathbf{G}_{\beta} = S^{\alpha\beta} \mathbf{G}_{\alpha} \otimes \mathbf{G}_{\beta}. \quad (6.13)$$

Equations 6.10 and 6.12 are solved numerically by the Finite Element Method. Therefore, geometry and displacements are discretized by standard displacement elements by piecewise interpolation of nodal coordinates

$$\mathbf{X} = \sum_{k=1}^{nel} N^k(\theta^1, \theta^2) \bar{\mathbf{X}}_k, \quad \mathbf{x} = \sum_{k=1}^{nel} N^k(\theta^1, \theta^2) (\bar{\mathbf{X}}_k + \bar{\mathbf{u}}_k) \quad (6.14)$$

and nodal displacements

$$\mathbf{u} = \sum_{k=1}^{nel} N^k(\theta^1, \theta^2) \bar{\mathbf{u}}_k, \quad (6.15)$$

respectively. Here the upper bar denotes nodal values and N are standard C_0 continuous shape functions.

The nodal displacement components are defined as free discrete parameters of form finding. They are arranged in a column vector \mathbf{b} of dimension n which denotes the number of degrees of freedom in the system. Hence, variation of any entity means variation with respect to the free parameters. This yields to the following formulations for the variation of the deformation gradient

$$\delta \mathbf{F} = \frac{\partial \mathbf{F}}{\partial b_r} \delta b_r = \delta \mathbf{g}_\alpha \otimes \mathbf{G}^\alpha = \frac{\partial \mathbf{g}_\alpha}{\partial b_r} \delta b_r \otimes \mathbf{G}^\alpha \quad (6.16)$$

and the covariant basis vector

$$\delta \mathbf{g}_\alpha = \delta \mathbf{x}_{,\alpha} = \frac{\partial \mathbf{g}_\alpha}{\partial b_r} \delta b_r = \sum_{k=1}^{nel} N^k_{,\alpha} \frac{\partial \bar{\mathbf{u}}_k}{\partial b_r} \delta b_r, \quad (6.17)$$

respectively. In the above equations b_r is the r^{th} component of \mathbf{b} , i.e. the r^{th} degree of freedom of the discretized problem.

By discretization of (6.12) one obtains a nonlinear set of n equations:

$$\frac{\partial w}{\partial b_r} = t \int_A (\mathbf{F} \cdot \mathbf{S}) : \frac{\partial \mathbf{F}}{\partial b_r} dA = 0. \quad (6.18)$$

It is well known that linearization of the form finding problem defined by (6.18) results in a singular system matrix due to the undetermined tangential position of the nodes. This deficiency can be overcome by stabilization methods like geometrical constraints or methods of numerical continuation. In the latter approach the idea is to modify the original problem by a related one, which fades out in the vicinity of the solution. The Updated Reference Strategy (URS) ([BR99]) applies equation 6.12 and a homotopy parameter λ to stabilize the singular formulation in (6.18). Therefore, the modified stationary condition reads as

$$\delta w_\lambda = \lambda t \int_A \det \mathbf{F} (\boldsymbol{\sigma} \cdot \mathbf{F}^{-T}) : \delta \mathbf{F} dA + (1 - \lambda) t \int_A (\mathbf{F} \cdot \mathbf{S}) : \delta \mathbf{F} dA = 0. \quad (6.19)$$

The stabilization effect is based on the prescribed PK2 stresses \mathbf{S} that are related to a constant reference configuration during the solution process.

Since the reference configuration is updated during the iteration procedure the difference between actual and reference configuration fades out. The value of the homotopy factor λ can be chosen such that $0 \leq \lambda < 1$. For $\lambda = 1$ the stabilization term would not work and the system of equations would be singular. For decreasing values of lambda the solution process becomes more and more stable but the speed of convergence decreases. It is also possible to perform the whole computation only with the stabilization term ($\lambda = 0$ in (6.19)). This approach results in a linear system of equations and is the generalized version of the force density method [Sch74], [Lin99a], [Lin99b], [MM98]. The URS turns out to be an extremely stable and robust solution algorithm and provides the basis for the proposed MSR formulation.

So far the discrete system of equations (6.19) is nonlinear in the terms of the discretization parameters b_r . It is solved iteratively by consistent linearization using the Newton-Raphson method. Linearization of (6.19) with $\lambda = 0$ is formulated by

$$LIN \left(\frac{\partial w}{\partial b_r} \right) = t \int_A (\mathbf{F} \cdot \mathbf{S}) : \frac{\partial \mathbf{F}}{\partial b_r} dA + \Delta b_s t \int_A \frac{\partial}{\partial b_s} \left((\mathbf{F} \cdot \mathbf{S}) : \frac{\partial \mathbf{F}}{\partial b_r} \right) dA = 0. \quad (6.20)$$

with $r, s \in \{1, \dots, n\}$. Reformulation of (6.20) yields to the problem: Find the unknown geometry \mathbf{x} such that the vector of unbalanced forces \mathbf{f} is equal to zero.

$$\mathbf{K}(\mathbf{x})\mathbf{u} = \mathbf{f}(\mathbf{x}) \quad \text{with} \quad \begin{cases} \mathbf{K} = t \int_A (\mathbf{F}_{,s} \cdot \mathbf{S}) : \mathbf{F}_{,r} dA \\ \mathbf{f} = -t \int_A (\mathbf{F} \cdot \mathbf{S}) : \mathbf{F}_{,r} dA \end{cases} \quad (6.21)$$

The geometry of the actual configuration follows from the reference configuration \mathbf{X} and the incremental displacements \mathbf{u} by $\mathbf{x} = \mathbf{X} + \mathbf{u}$. Stiffness matrix \mathbf{K} and vector of unbalanced forces \mathbf{f} depend on membrane thickness t , second Piola Kirchhoff stress tensor \mathbf{S} , deformation gradient \mathbf{F} and derivatives of deformation gradient $\mathbf{F}_{,r}$ and $\mathbf{F}_{,s}$ where the subscripts r and s indicate the degrees of freedom of the model, e.g. the unknown nodal positions. It should be clearly indicated that the stiffness matrix \mathbf{K} and the vector of unbalanced forces \mathbf{f} are related to the mesh regularization problem only. The solution of the underlying structural problem is governed by a different set of equations. According to membrane theory the tangential prestress is defined as boundary condition of the governing PDE. Equation (6.21) is solved iteratively until the solution is converged ($|\Delta \mathbf{u}| < tol$) where the reference configuration is updated at each iteration step. When

the solution is convergent the reference configuration \mathbf{X} is nearly equal to the actual configuration \mathbf{x} .

The URS based form finding approach introduced so far was extended by adaptive prestress modification to prevent numerical problems for ill-posed formulations [WB05], [Wüc07] where equilibrium geometries for isotropic prestresses do not exist. These kind of problems often result in extreme element distortions which end up in numerical problems. The reason for this mesh distortions is the fact that the element prestress \mathbf{S} in (6.21) does not depend on the element geometry. In the following a method is presented that allows for an adaptive prestress update in each element. By this approach the stress update rule can be defined in a way that the size and the shape of the elements fulfills defined quality criteria as good as possible. This extension allows a generalization of the URS approach to a effective mesh regularization method applicable to all kind of finite elements.

Figure 6.13 defines the applied configurations for the derivation of the MSR algorithm. The covariant basis vectors for the initial and the actual configuration are specified as $\mathbf{G}_{0\alpha}$ and \mathbf{g}_α respectively. The maximum allowed element deformation is specified by the covariant basis vectors of the limit configuration $\mathbf{G}_{max\alpha}$. There exist several possibilities to specify the limit configuration:

- In several application it is sufficient to apply the best possible element shape as limit configuration. The best possible shapes for quadrilateral and triangles are the unit square and the unit triangle respectively. In this case all elements that are regularized try to reach the respective optimal shapes as close as possible.
- Whenever properties of the initial mesh should be preserved during the mesh regularization process the optimal element shapes are scaled with the initial volume of the respective element. In this case it is ensured that regions with specific mesh densities keep their element sizes during mesh regularization whereas the element shapes where improved.
- Instead of using auxiliary optimal elements as limit configuration the initial element geometries itself can be used. By this approach the regularized mesh shows only minimal differences to the initial grid.

The introduced basis systems can be transformed in principal directions indicated by a tilde. Transformations between initial and actual configuration

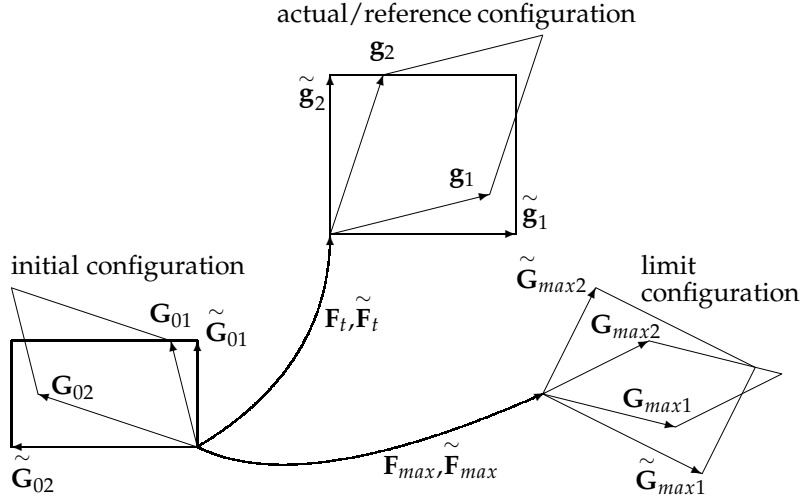


Figure 6.13: Configurations for MSR

and initial and limit configuration are indicated by \mathbf{F}_t and \mathbf{F}_{max} respectively.

Element shape control of the MSR method is based on the principal stretches of the elements in the reference configuration. The deformation at iteration step k is defined by the total deformation gradient \mathbf{F}_t^k :

$$\mathbf{F}_t^k = \mathbf{g}_\alpha^k \otimes \mathbf{G}_0^\alpha \quad (6.22)$$

The subscripts and superscripts $\alpha \in \{1,2\}$ indicate the plane co- and contravariant basis vectors, respectively. The total right Cauchy Green tensor \mathbf{C}_t follows from the deformation gradient by

$$\mathbf{C}_t = \mathbf{F}_t^T \mathbf{F}_t \quad (6.23)$$

where the iteration counter k is omitted for simplicity. The element distortion is measured by principal stretches which follow from the eigenvalues of the right Cauchy Green tensor by the equation

$$(\mathbf{C}_t - \lambda_i^2 \mathbf{I}) \tilde{\mathbf{N}}_i = \mathbf{0}. \quad (6.24)$$

The principal stretches are denoted by γ_{t_α} with $\alpha \in \{1,2\}$. These parameters are compared with predefined limit stretches γ_{max_α} and γ_{min_α} . If the principal stretches violate these bounds the element prestresses are modified by the factors β_α :

$$\beta_\alpha = \begin{cases} \frac{\gamma_{max_\alpha}}{\gamma_{t_\alpha}} & \text{if } \gamma_{t_\alpha} > \gamma_{max_\alpha} \\ \frac{\gamma_{min_\alpha}}{\gamma_{t_\alpha}} & \text{if } \gamma_{t_\alpha} < \gamma_{min_\alpha} \end{cases} \quad \text{with } \alpha \in \{1,2\} \quad (6.25)$$

The general stress update procedure can be formulated by a nested sequence of pull back and push forward operations:

1. apply prestress to limit configuration
2. perform pull back operation to initial configuration
3. compute push forward operation to actual configuration

$$\mathbf{S}_{mod} = \tilde{\mathbf{F}}_t \tilde{\mathbf{F}}_{max}^{-1} \mathbf{S} \tilde{\mathbf{F}}_{max}^{-T} \tilde{\mathbf{F}}_t^T \quad \text{with} \quad \begin{cases} \tilde{\mathbf{F}}_t = \begin{bmatrix} \gamma_{t1} & 0 \\ 0 & \gamma_{t2} \end{bmatrix} \\ \tilde{\mathbf{F}}_{max} = \begin{bmatrix} \gamma_{max1} & 0 \\ 0 & \gamma_{max2} \end{bmatrix} \end{cases} \quad (6.26)$$

The deformation gradients $\tilde{\mathbf{F}}_t$ and $\tilde{\mathbf{F}}_{max}$ (cf. Figure 6.13) define the transformation of the principal directions from the initial configuration to the actual configuration and the limit configuration, respectively. After substitution of (6.25) in (6.26) one obtains a simple equation for the modified prestress $S_{mod}^{\alpha\beta}$:

$$S_{mod}^{\alpha\beta} = \frac{S^{\alpha\beta}}{\beta_\alpha \beta_\beta} \quad \text{with} \quad \alpha, \beta \in \{1,2\}. \quad (6.27)$$

The modification of the prestress during the iterative solution procedure ensures that the principal deformation of all elements does not exceed the region defined by γ_{max} and γ_{min} . If an element becomes too large during the regularization process the prestress is increased. Otherwise if an element becomes too small the prestress is decreased. This results in a model where the necessary mesh deformation is distributed to all elements in the mesh.

The regularization method introduced so far computes the equilibrium shape for a given boundary and a given prestress with a limited element distortion. But in the context of shape optimization this approach is applied to a known geometry which should be preserved. Here the geometry is defined by nodal coordinates and respective directors. This constraint is fulfilled by application of the MSR approach to the set of tangential coordinates. In general there exist several possibilities to include such constraints in the formulation like Lagrangian multipliers or Penalty methods. In the proposed MSR method the normal degree of freedom at each node is eliminated by the Master Slave Method. Due to the reduced number of dofs the system of equations is smaller and the solution is more efficient. The transformation rules are formulated in a unsymmetric matrix \mathbf{T} . The number of rows and columns corresponds to the original number of dofs and

the reduced number of dofs respectively. By this matrix \mathbf{T} the constrained stiffness matrix \mathbf{K}^* and the constrained vector of unbalanced forces can be computed by

$$\mathbf{K}^* = \mathbf{T}^T \mathbf{K} \mathbf{T} \quad \text{and} \quad \mathbf{f}^* = \mathbf{T}^T \mathbf{f} \quad \text{respectively.} \quad (6.28)$$

The solution of the linearized system of equations $\mathbf{K}^* \mathbf{u}^* = \mathbf{f}^*$ gives the constrained vector of incremental displacements. The back transformation to a cartesian metric is computed by $\mathbf{u} = \mathbf{T} \mathbf{u}^*$.

Application of the MSR method for mesh stabilization during the FE-based shape optimization process yields to robust element aspect ratios without large local element distortions. Such meshes are the crucial prerequisite for accurate sensitivity responses. Thus, the MSR method and the sensitivity filter allow accurate sensitivity analysis during the whole optimization procedure.

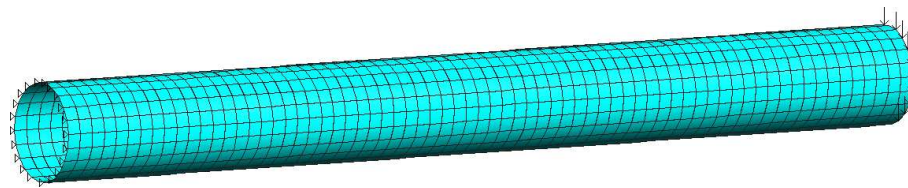
6.4 Model Problem V

The fifth model problem investigates the general effects of the proposed sensitivity filter and the mesh regularization methods. The mechanical model describes a cantilever made from a pipe of linear elastic material discretized by Reissner-Mindlin shell elements. One end of the pipe is Navier supported whereas the other end is subjected to constant nodal forces in vertical direction. The dimensions of the initial structure are: length = 20, diameter = 2 and thickness = 0.01, c.f. figure 6.14a.

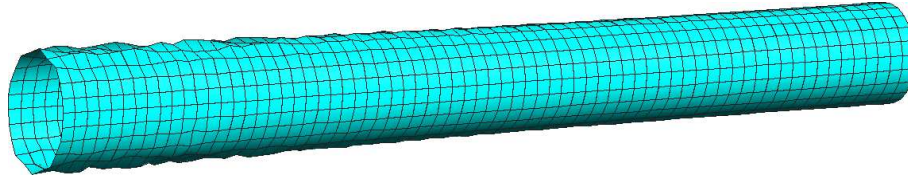
Optimization goal is minimization of linear compliance (3.32) with constant structural mass. The design variables are the normal coordinates at each node. At both ends of the structure the design update is restricted such that the length of the cantilever remains constant. The optimization problem is solved by the ALM optimizer presented in section 4.7.2.

It is obvious that the solution without any regularization (figure 6.14b) is completely useless. The only difference to the initial design is a high mesh distortion which results in an improved stiffness. However, this stiffness improvement is a pure numerical and erroneous effect. Additionally, the absence of the sensitivity filter results in highly mesh dependent results. A modified discretization would lead to a completely different design which is unacceptable.

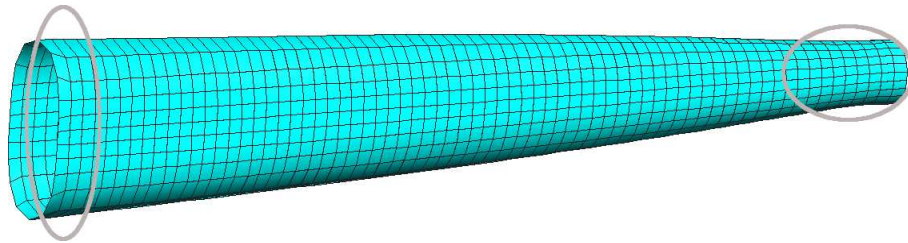
Application of the proposed sensitivity filter yields to a clearly improved and structural meaningful optimization result. The design depicted in fig-



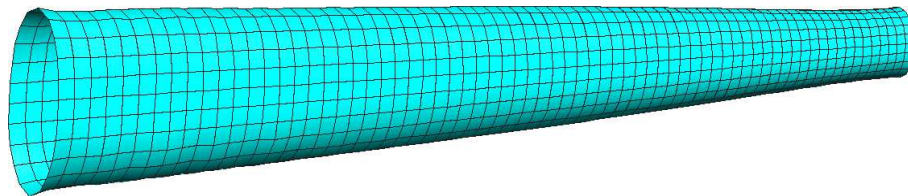
(a) Initial geometry



(b) Optimal geometry without any regularization



(c) Optimal geometry with sensitivity filter but without mesh regularization



(d) Optimal geometry with full regularization

Figure 6.14: Designs for Model Problem V

ure 6.14c shows a significant improved stiffness whereas the mass is equal to the initial design. A closer look to the mesh quality in the marked regions shows the necessity of tangential mesh regularization. Especially at both ends of the cantilever the elements are seriously distorted. As mentioned earlier such distortions result in a disturbed gradient field.

Figure 6.14d occupies that the discretization can be improved further. Here the proposed mesh regularization method is applied to ensure the best possible discretization for the optimal geometry. It is easy to verify that at the support region as well as at the loaded end of the beam the elements show nearly perfect aspect ratios. In this example the structural strain energy was decreased by a factor of 2.2 without increasing structural mass. At the

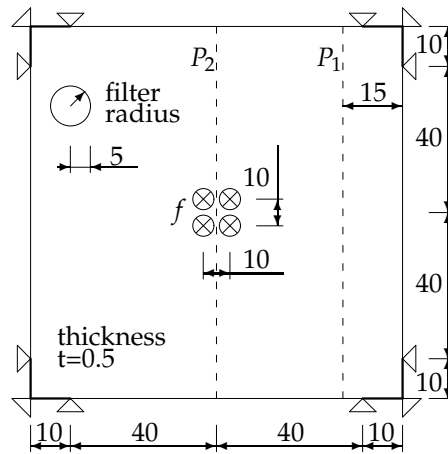


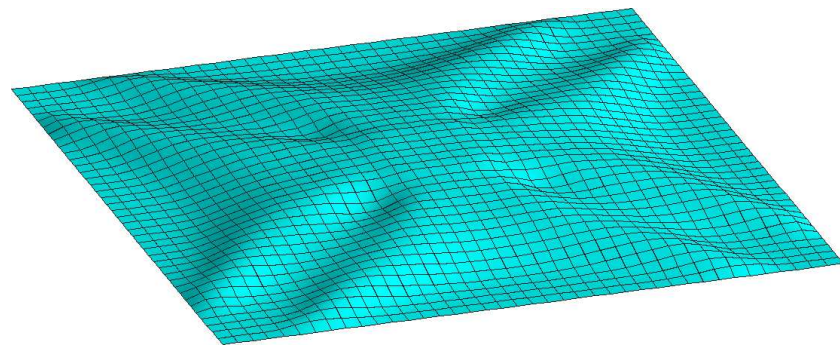
Figure 6.15: Geometry, support and loading of quadratic plate

same time the tip displacement is reduced by a factor of 2.1.

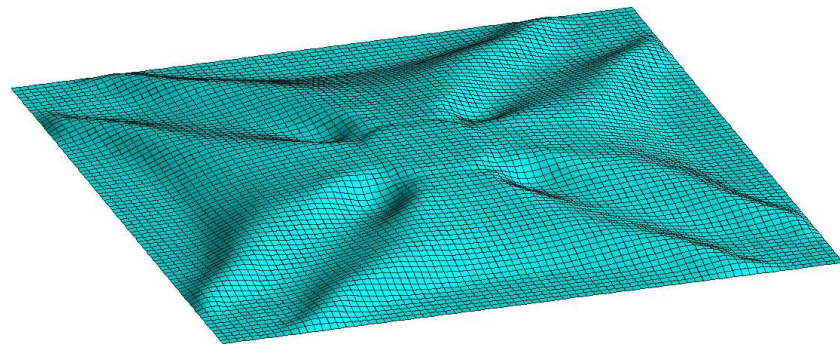
6.5 Model Problem VIa

The second model problem of this chapter intends to demonstrate the mesh independency of the optimal solutions. It shows a quadratic plate with corner support and central loading by four nodal forces f according to Figure 6.15. The specified geometry is discretized by 1600 (Mesh I), 6400 (Mesh II) and 14400 (Mesh III) elements, respectively. The goal of the optimization problem is to maximize the stiffness of the structure. The shape derivatives are regularized with the projection method introduced in section 6.2.2. For this example cubic filter functions (figure 6.4d) with a radius $r = 5$ are applied.

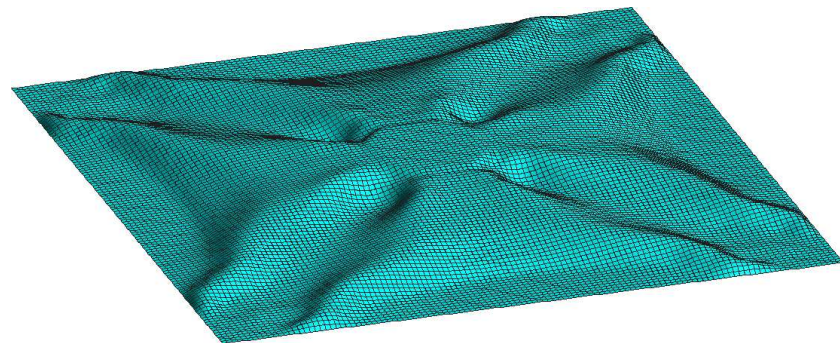
The optimal geometry specified by the different discretizations is presented in figure 6.16. It is characterized by a membrane dominated load carrying behavior utilizing eight bead like structures that transfer the load from the center to the supports near the corners. The mesh independency of the results is more clearly shown by the graphs in figure 6.17. Here, the cross sections along the paths P_1 and P_2 are compared for the three discretizations. It is easy to verify that the three different discretizations describe nearly the same geometry. Only along path P_1 some minor differences between Mesh I and the finer grids are visible. A possible reason is the small filter radius which controls the curvature of the geometry. In general, a suf-



(a) Mesh I



(b) Mesh II



(c) Mesh III

Figure 6.16: Optimal design for Model Problem VIa

efficient number of elements is required to ensure a robust approximation of highly curved geometry regions. Obviously, Mesh I is a little bit too coarse for this small filter radius. Along path P_2 the curvature is small enough so that the coarse grid of Mesh I allows for a good approximation too.

Figure 6.18a shows the convergence of the objective for the three discretizations where the function values are scaled with respect to the initial designs. Obviously, all optimizations converge to the same result. Even convergence

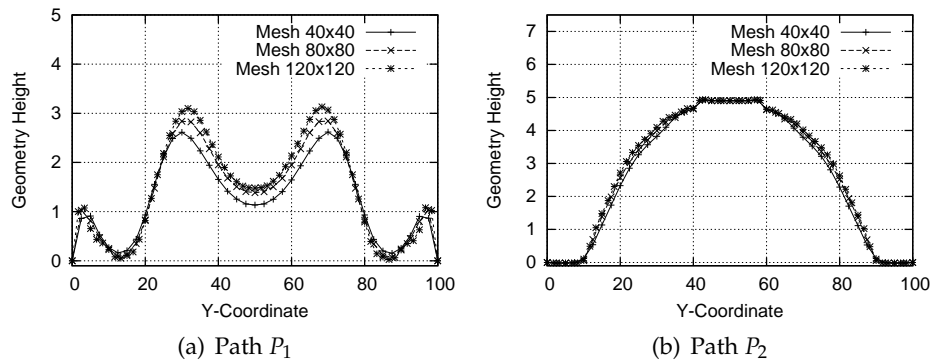


Figure 6.17: Path plots for Model Problem VIa

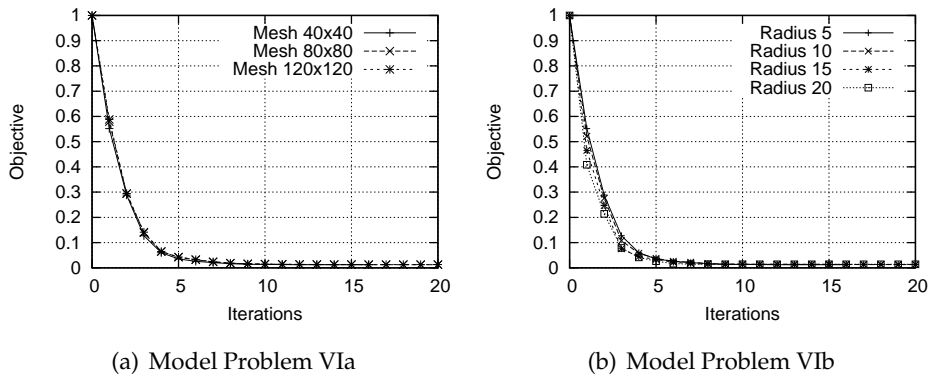


Figure 6.18: Convergence of objectives for Model Problems VIa and VIb

to the minimum does not show any difference.

6.6 Model Problem VIb

This model problem is related to the previous Model Problem VIa but here the influence of an increasing filter radius on the optimization result should be demonstrated. Again the quadratic plate problem depicted in figure 6.15 is investigated. Instead of varying the mesh density this example uses a fixed mesh with 40x40 elements (Mesh I). All other parameters of the mechanical problem and the optimization model are similar to Model Problem VIa. Filter radii of of size 5, 10, 15 and 20 are applied and their effects on the optimal geometries are visualized.

Figure 6.19 compares the optimal geometries along the paths P_1 and P_2 . Especially the optimal geometries along path P_1 are significantly influenced

by the size of the filter radius. It can be observed that the curvature of the optimal geometry decreases when the filter radius increases. Thus, application of a large filter radius yields to smooth geometries whereas a small filter radius allows for wavy geometries. Comparing figures 6.19a and 6.19b

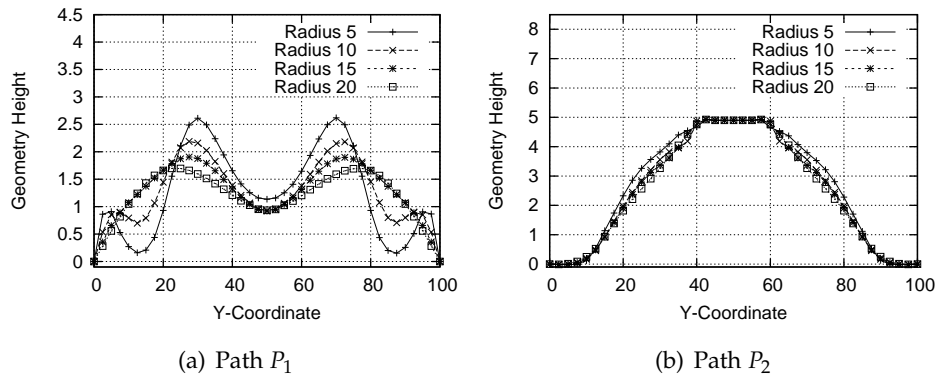


Figure 6.19: Path plots for Model Problem VIb

shows that a smaller filter radius does not automatically yield to wavy geometries. Along path P_2 the varying filter radius has only a small influence on the optimal geometries. The reason is that the optimal geometry along path P_2 is less wavy than the optimal geometry along path P_1 . Such a smooth optimal geometry would be only affected if the filter radius would be significantly increased.

The previously presented optimization results show that the radius of the filter function is an appropriate tool to control the curvature of the optimal result. But the more important question is if the size of the filter radius does also influence the quality of the optimum. The quality of an optimum is usually measured by the value of the applied objective function. Figure 6.18b clearly shows that all optimal geometries exhibit nearly the same objective value and convergence behavior. Thus, there exist many nearly equivalent solutions for the presented optimization problem. Obviously, this statement is problem dependent and not always true. Nevertheless, many shape optimization problems have a significant number of possible solutions with nearly equal mechanical properties. This offers the possibility to the designer to choose between several solutions which look different but act similar.

6.7 Summary

This chapter introduces a full stabilized formulation for FE-based shape optimization problems. The motivation, the detailed derivation and the application of normal and tangential regularization methods were presented. The basic properties of the proposed approach are summarized in the following statements.

- The sensitivity filter and the mesh regularization method are applicable to all kind of shape optimization problems, independent from type of objective, constraints or mechanical model.
- The introduced filter method is based on the well known mathematical theory of convolution integrals. The method offers a direct control of the smoothness of the optimal geometry. Model Problem VIa and VIb show that the proposed filter method guarantees mesh independent results and provides an upper limit to the maximum curvature of the optimal design.
- Exact numerical response of the mechanical model requires robust element aspect ratios. This is ensured by the proposed mechanically motivated mesh regularization algorithm. Here, the necessary mesh distortion is distributed equally over the whole mesh. Hence, the geometry of each single element is distorted as less as possible.

Chapter 7

Shape Optimization of Geometrically Nonlinear Problems

Nonlinear analysis methods allow for a very accurate modeling of structural behavior. This accuracy is enabled due to formulation of structural equilibrium in the deformed configuration, c.f. figure 2.1. The equilibrium has to be calculated by iterative procedures because the governing equations are nonlinear. There exist several types of nonlinearities e.g. material nonlinearities, contact, or geometrical nonlinearities. In this chapter only geometrically nonlinear problems are investigated but the derived methods are applicable to all kind of nonlinear problems that allow for analytic differentiation of response functions. Geometrical nonlinear problems show serious deformations which require their consideration in the equilibrium formulation. Such models permit an exact computation of the load-displacement behavior, the limit load and post-buckling properties. Additionally, the influence of imperfections on the structural characteristics can be analyzed. A basic property of nonlinear analysis are the time consuming solution algorithms. Usually they require the computation of several load steps where each step requires several equilibrium iterations. A more detailed introduction to nonlinear analysis and the basic solution strategies can be found in [ZTZ00], [BLM00] and [Bat95].

Structural optimization of geometrically nonlinear models incorporates the nonlinear behavior in the response functions and also in the sensitivity analysis. Such problems were often solved by SAND (Simultaneous Analysis and Design) formulations [AW05]. SAND formulations apply the state variables, such as displacements, as optimization variables in addition to the classical design variables. The governing equilibrium equations are

treated as equality constraints.

Smaoui and Schmit [SS88] propose an integrated approach for minimum weight design of geometrically nonlinear truss structures. They incorporate constraints with respect to displacements, stresses and buckling behavior. The structural equilibrium equations are treated as equality constraints. A generalized reduced gradient (GRG) method [Van84] was used to solve the constrained optimization problem.

Haftka and Kamat [HK89] compare simultaneous and nested approaches for geometrically nonlinear truss problems. The authors apply several optimization algorithms like penalty methods, projected Lagrangian methods and GRG methods to the constrained problems.

Ringertz also presents simultaneous approaches to solve geometrically nonlinear optimization problems [Rin89], [Rin92], [Rin95]. In the latter publications the author applies the methods to shell models whereas the predominant number of publications consider truss examples. However, only a few number of sizing design variables are applied in the examples. The constrained optimization problems are solved by an SQP method.

Another application related to nonlinear shell problems is presented by [SL05]. This publication investigates SIMP based topology optimization of layered shell structures modeled by Mindlin elements. The authors use a NAND approach with adjoint sensitivity analysis to compute first order gradients that are subjected to a MMA optimization algorithm. Several examples compare the geometrical nonlinear results with the linear results.

Shape optimization of shell problems with respect to the critical load is presented by R. Reitingner in [Rei94]. Here, the shape parametrization is realized by Bézier splines. Topology optimization of shells and solids with respect to nonlinear stiffness is investigated by R. Kemmler in [Kem04]. The following sections refer to both approaches more precisely.

7.1 General Optimization Goals

Similar to geometrically linear formulations the basic goal of geometrically nonlinear optimization is the improvement of structural properties. Important objectives of nonlinear structures are limit load and structural stiffness.

Usually, the critical load follows from a full analysis of the load-displacement path by path following methods. Another strategy is the semi-definite programming method which directly calculates critical loads from an equilibrium point close to the critical load. Formulation of the

critical load by this method allows for differentiation with respect to design variables. Thus, the critical load can be directly applied as response function, c.f. [Rei94]. Drawbacks of this approach are the high numerical effort of semi-definite programming methods, the complicated behavior at bifurcation points and the sensitive algorithms.

Another way to improve the critical load implicitly is the improvement of structural stiffness. Usually, stiffer structures show a more effective load carrying behavior with smaller deformations and therefore also an improved critical load. The basic advantage of this method is that structural stiffness can be formulated much easier and much more robust than the critical load. The disadvantage is that there is no guarantee that the critical load improves if structural stiffness is improved. Nevertheless, the latter approach has been applied successfully to topology optimization problems in [Kem04]. Therefore, the following investigations concentrate on stiffness optimization instead of direct optimizing the critical load.

7.2 Response Functions for Structural Stiffness

Common measures for structural stiffness are compliance and strain energy. In geometrically linear problems both measures yield to equal values because of the linear load-displacement relation. Therefore, both quantities are often not distinguished. In geometrically nonlinear problems the load displacement relation is in general nonlinear, c.f. figure 7.1 and strain energy and compliance describe different structural properties. Due to nonlinearity the exact evaluation of structural strain energy or compliance at a specified load level requires an accurate integration of the load-displacement relation. A possible numerical integration of the load-displacement curve utilizing four load levels and the trapezoidal rule is visualized in figure 7.1. It is obvious that such approaches require a sufficient number of sampling points. These number of sampling points has to be recomputed in each optimization step in order to evaluate the objective. Thus, direct evaluation of the internal energy is very time consuming and, therefore, not applicable to large structural optimization problems. More information about nonlinear stiffness formulations is presented in [Kem04]. In order to reduce the effort of strain energy computation approximation methods are frequently applied. A numerically very efficient approximation method is depicted in figure 7.2. This approach is based on a triangular

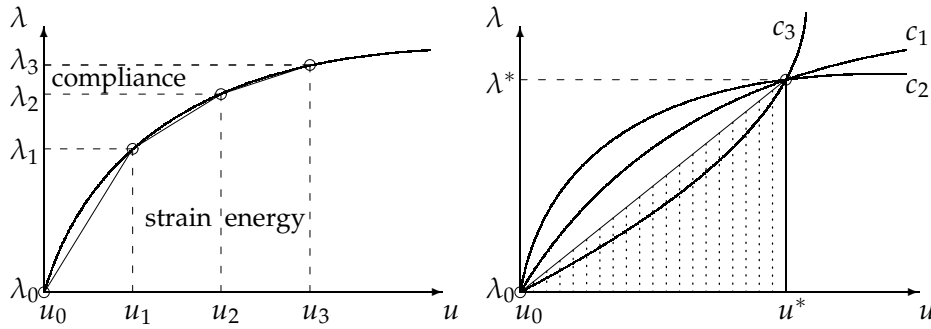


Figure 7.1: Nonlinear strain energy **Figure 7.2:** Approximated strain energy

approximation of strain energy and compliance which can be expressed by

$$f(\mathbf{u}, \mathbf{s}) = \frac{1}{2} (\mathbf{f}_{ext}^*)^T \mathbf{u}^* \quad (7.1)$$

where the external load \mathbf{f}_{ext}^* contains the specified load factor λ^* . In this method strain energy and compliance yield to the same value again. This is visualized by the graphs c_1 , c_2 and c_3 which characterize load-displacement curves of three different designs where all three designs show the same displacements for the specified load level λ^* . All designs yield to the same response value but the exact evaluation of strain energy and compliance results obviously in different values. A similar approximation is presented in [BPS00] and [Kem04] where the authors suggest the name 'End Compliance' for this formulation. It is obvious that this triangular approximation does not guarantee precise values for the strain energy. But the application as response function does not require a precise absolute value. In structural optimization the response function values are applied to measure the quality of design modifications. Therefore, relative quantities are used which may be also related to approximations. The basic advantages of a response function specified in (7.1) are efficient evaluation and differentiation. The differentiation is presented in detail in the next section whereas the formulation of an extended nonlinear path following method is introduced in section 7.5.

7.3 Sensitivity Analysis

Differentiation of equation 7.1 with respect to a design variable s_i is expressed by

$$\frac{df}{ds_i} = \frac{1}{2} \left(\frac{\partial \mathbf{f}_{ext}^*}{\partial s_i} \right)^T \mathbf{u}^* + \left(\frac{1}{2} \frac{\partial \mathbf{f}_{ext}^*}{\partial \mathbf{u}} \mathbf{u}^* + \frac{1}{2} \mathbf{f}_{ext}^* \right)^T \frac{\partial \mathbf{u}}{\partial s_i}. \quad (7.2)$$

Substitution of the nonlinear state derivative defined by equation 3.41 in the above formulation gives the direct derivative formulation

$$\frac{df}{ds_i} = \frac{1}{2} \left(\frac{\partial \mathbf{f}_{ext}^*}{\partial s_i} \right)^T \mathbf{u}^* + \left(\frac{1}{2} \frac{\partial \mathbf{f}_{ext}^*}{\partial \mathbf{u}} \mathbf{u}^* + \frac{1}{2} \mathbf{f}_{ext}^* \right)^T \mathbf{K}_t^{-1} \left(\frac{\partial \mathbf{f}_{ext}^*}{\partial s_i} - \frac{\partial \mathbf{f}_{int}^*}{\partial s_i} \right). \quad (7.3)$$

It is easy to verify that this formulation is numerically expensive if the matrix-vector products are solved from right to left and if many design variables have to be considered.

By the adjoint approach as introduced in equation 7.4 the effort is dramatically reduced.

$$\frac{df}{ds_i} = \frac{1}{2} \left(\frac{\partial \mathbf{f}_{ext}^*}{\partial s_i} \right)^T \mathbf{u}^* + \underbrace{\left[\mathbf{K}_t^{-1} \left(\frac{1}{2} \frac{\partial \mathbf{f}_{ext}^*}{\partial \mathbf{u}} \mathbf{u}^* + \frac{1}{2} \mathbf{f}_{ext}^* \right) \right]^T}_{\boldsymbol{\lambda}^T} \mathbf{f}_{nl}^* \quad (7.4)$$

Obviously the right hand side of the adjoint equation system does not depend on the design variables. Thus, the adjoint vector $\boldsymbol{\lambda}$ has to be computed only once per response function and can be used for the complete sensitivity analysis of this response function by element based operations.

7.4 Structural Imperfections

In reality, perfect structures do not exist but in many structural analysis problems perfect structures are assumed. In linear analysis problems the influence of small imperfections might be negligible but in nonlinear problems they are essential. In general, imperfections may be caused by manufacturing tolerances, varying boundary conditions (supports, loads) or varying material properties. Geometrically nonlinear structures acting in membrane action are sensitive to geometrical imperfections.

Usually, the exact shape of the imperfections is not known but the achievable tolerances are mostly known. Thus, a common procedure is to compute the imperfection form based on scaled eigenmodes of the initial struc-

ture. Structural eigenvalue analysis can be performed by a linear pre-buckling analysis defined by

$$(\mathbf{K} - \lambda \mathbf{K}_g) \boldsymbol{\phi} = \mathbf{0}. \quad (7.5)$$

More information about linear buckling analysis is presented in section 3.4.3. Another possibility is the solution of the eigenproblem

$$(\mathbf{K}_t - \lambda \mathbf{I}) \boldsymbol{\phi} = \mathbf{0}. \quad (7.6)$$

with the tangential stiffness \mathbf{K}_t and the identity matrix \mathbf{I} . It should be noted that the eigenvalues in equations 7.5 and 7.6 describe different quantities. Usually a scaled set of the n smallest eigenmodes is applied as imperfection. The scaling factors a_i are chosen according to the sign of the eigenmodes and the estimated tolerance tol . Finally the imperfection mode $\Delta \mathbf{X}_{imp}$ can be calculated by

$$\Delta \mathbf{X}_{imp} = \frac{tol}{\left| \sum_{i=1}^n a_i \boldsymbol{\phi}_i \right|_{L_1}} \sum_{i=1}^n a_i \boldsymbol{\phi}_i. \quad (7.7)$$

The nonlinear analysis is then performed with the imperfect geometry \mathbf{X}_{imp} computed by $\mathbf{X} + \Delta \mathbf{X}_{imp}$.

In general it is also possible to consider imperfections during structural optimization. The goal of such optimization problems is to derive structural designs with small imperfection sensitivity. This requires quantification and differentiation of imperfection sensitivity and imperfection modes, respectively. The differentiation of eigenmodes is presented in [HCK86], [BSS94] and [HG92]. Integration of imperfection sensitivity in structural optimization is investigated in [Kem04] and [Rei94].

7.5 Simultaneous Analysis and Optimization

In this section a solution algorithm for simultaneous nonlinear analysis and optimization is presented. This algorithm has the general goal to minimize the number of necessary system evaluations because they are mainly responsible for the effort of the whole optimization problem. The basic steps of this procedure are visualized by the load-displacement curves in figure 7.3 and by the flow chart in figure 7.4.

The optimization starts by following the load displacement path of the initial design \mathbf{X}^0 . If the defined load level λ^* is reached the load is kept constant for the following steps. In figure 7.3 this load level λ^* was reached

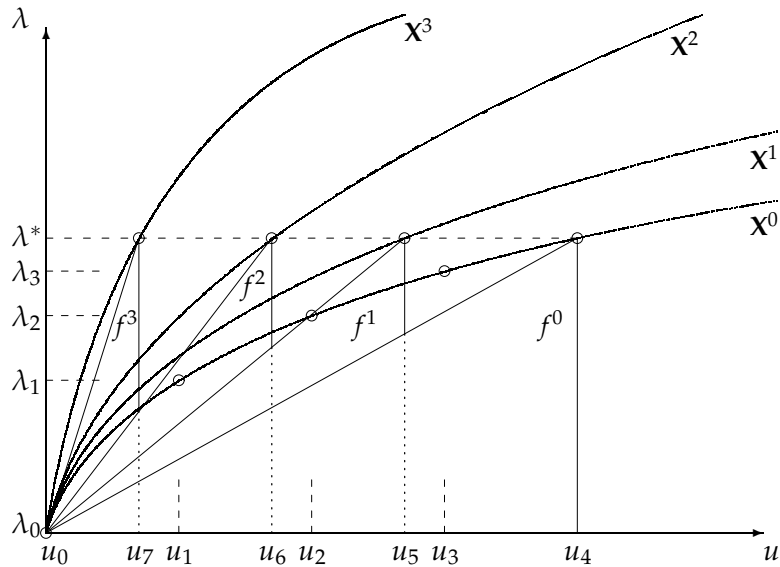


Figure 7.3: Geometrically nonlinear optimization procedure

after four load steps. After reaching the desired load level the first optimization step computes the objective value f^0 by equation 7.1 and the design update \mathbf{d}^0 to reach the improved design \mathbf{X}^1 by $\mathbf{X}^1 = \mathbf{X}^0 + \mathbf{d}^0$. During the line search procedure the new displacement field \mathbf{u}_5 is computed. This allows for computation of the new objective f^1 and for the new design update \mathbf{d}^1 . The described procedure is repeated until the optimization problem is converged.

For each new design \mathbf{X}^i an eigenvalue analysis according to (7.6) has to be performed. If the smallest eigenvalues are positive it is ensured that there exist no critical point below the actual load level. Due to the design modifications it cannot be precluded that such critical points appear during optimization. In this seldom case the optimization has to be repeated with a different start design or different regularization parameters.

After convergence of the optimization procedure the influence of structural imperfections has to be investigated. Therefore the optimal structure is disturbed by an imperfection mode according to section 7.4. A final analysis of the full load-displacement curves of perfect and imperfect optimal structures show the critical loads as well as the influence of the imperfection on the optimal design. Usually optimized structures are more sensitive to imperfections than their initial design. This is caused by the more efficient and

more sensitive load carrying behavior by membrane forces and the higher loads that an optimal structure is able to carry.

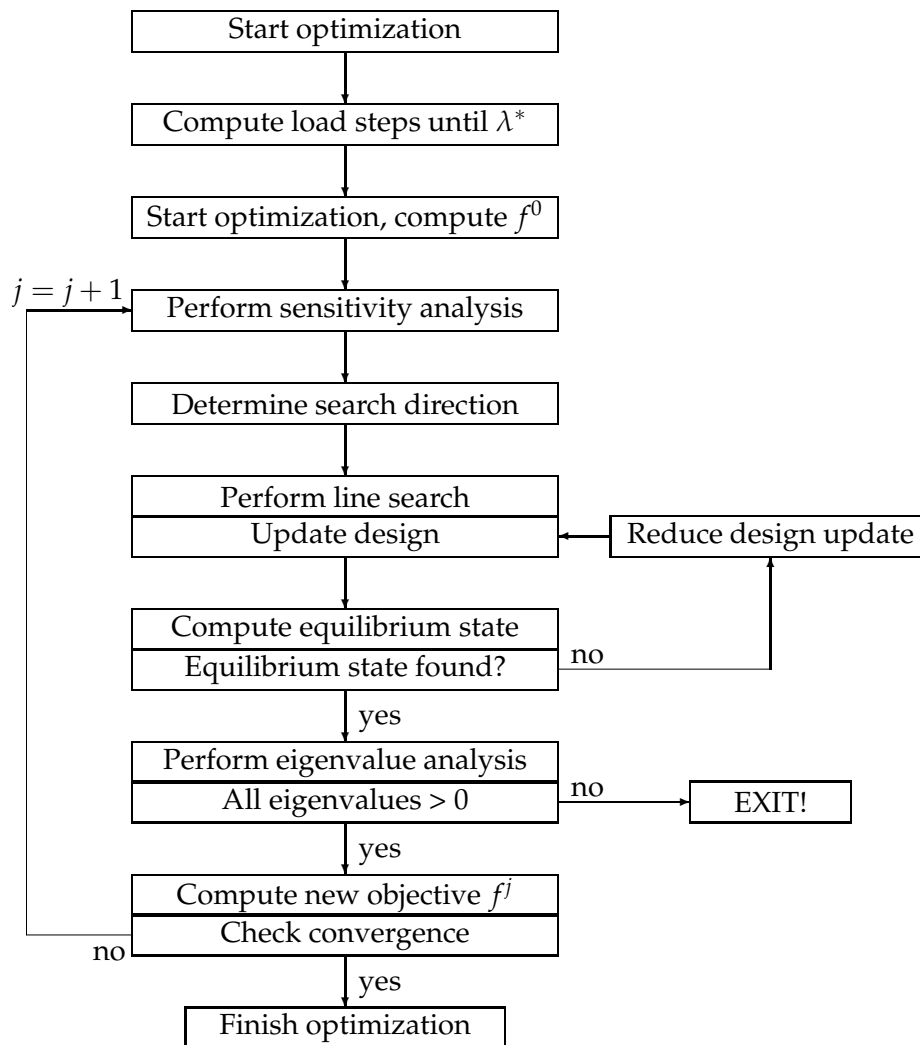


Figure 7.4: Simultaneous analysis and optimization procedure

7.6 Model Problem VII

The example presented in figure 7.5 was chosen to demonstrate the basic properties of the proposed geometrically nonlinear optimization procedure.

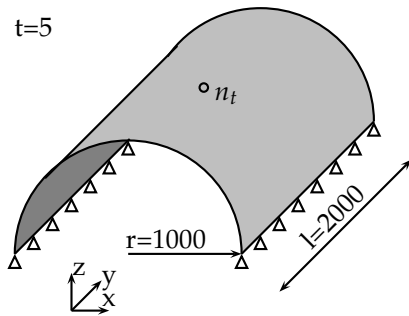


Figure 7.5: Tunnel shell

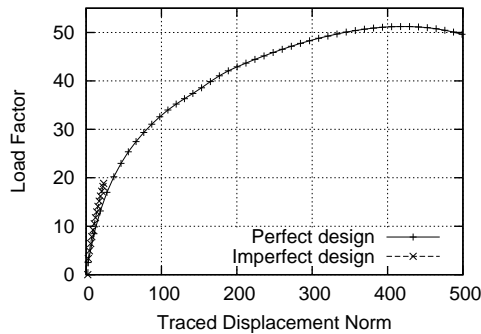


Figure 7.6: Load displacement curve

It describes a cylindrical tunnel shell with radius equals 1000mm and length equals 2000mm. The shell is discretized by 1500 Reissner-Mindlin shell elements with 5mm thickness. The material is described by St.Venant-Kirchhoff material with Young's modulus equal to $210000N/mm^2$ and Poisson's ratio equals 0.3. The structure is subjected to dead load in negative z -direction and supported along the straight edges as shown in figure 7.5.

It is well known that there exists a critical load level where the structure snaps through. The load-displacement curve of the tunnel shell under dead load is depicted in figure 7.6. Here the load factor is plotted against the absolute z -displacement of node n_t depicted in figure 7.5. One observes the critical load factor of the perfect design close to 51. Unfortunately this load level results in huge displacements of more than 400mm.

The imperfection sensitivity of this geometry is investigated by another nonlinear analysis where the perfect cylindrical structure is disturbed by the sum of eigenmodes presented in figure 7.7. The resulting imperfection mode is calculated by equation 7.7 with an imperfection tolerance $tol=1.0mm$ and $a_1, \dots, a_4=1.0$. Thus, the imperfection size corresponds to 0.1% of the cylinder radius. The nonlinear analysis of the imperfect design results in the load-displacement curve also depicted in figure 7.6. It is easy to verify that the imperfect design reacts slightly stiffer compared to the perfect design. But the more interesting difference between both geometries is the critical load. The critical load factor of the imperfect design is

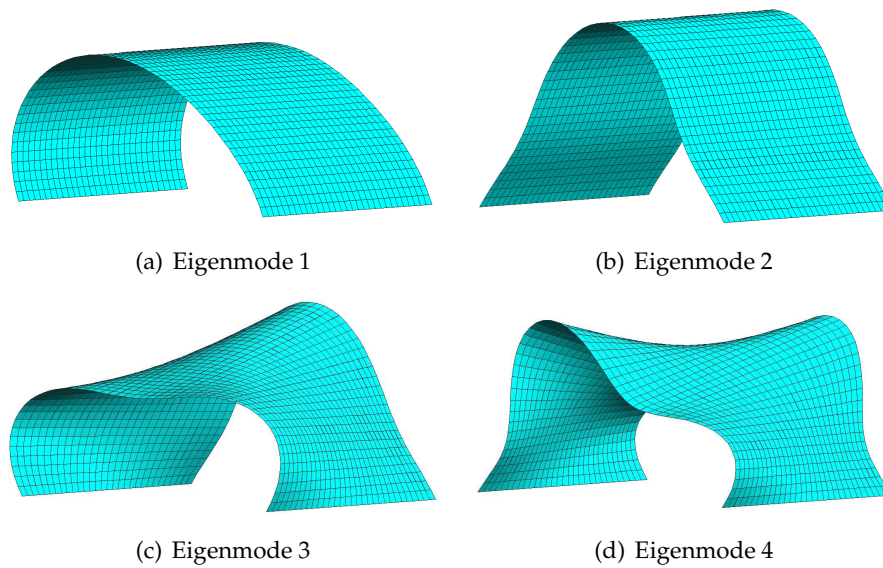


Figure 7.7: Eigenmodes of cylindrical tunnel shell

close to 19 and therefore 2.7 times smaller than the critical load factor of the perfect design. This example shows that the cylindrical tunnel shell is highly sensitive to geometrical imperfections.

In the following a shape optimization is performed in order to improve stiffness and critical load of the tunnel, c.f. section 7.2. The coordinates in direction of surface normals of all unsupported nodes are chosen as design variables which gives a set of 1519 optimization variables. The optimization of the perfect tunnel geometry was performed with a load factor λ^* equals to 15 which corresponds to 30% of the critical load of the circular tunnel. A further increased load level results in convergence problems during the line search procedure. The computed gradients are smoothed by the proposed filter method (c.f. section 6.2) where cubic filter functions with a radius equal to 500mm are applied. The optimization was performed by a CG-optimizer, c.f. section 4.6.2. Suitable step lengths follow from a quadratic line search procedure with initial step length $\alpha_0 = 10\text{mm}$, c.f. section 4.8.

The optimal design of the defined optimization problem is presented in figure 7.8. It is obtained after 30 optimization steps. Especially in the center region it shows serious differences compared to the initial design. Here, the arch geometry changed from a circular to a catenary curve which could be expected. The arches at both ends of the tunnel do not change their shape seriously. The arch geometries at the center of the tunnel and at one end are

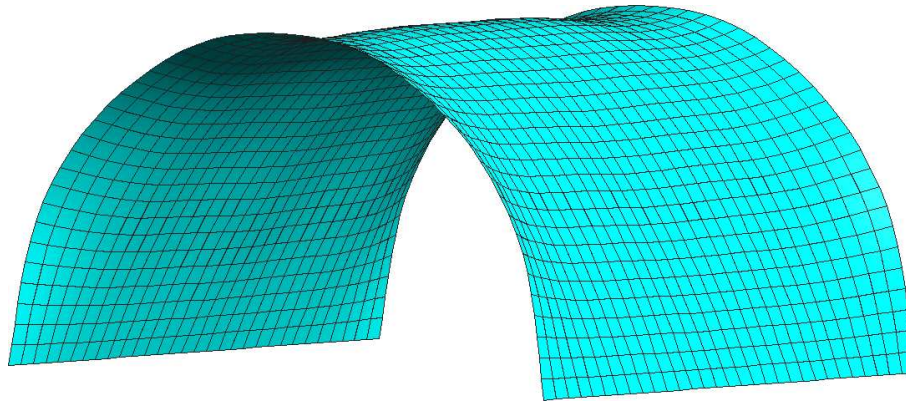


Figure 7.8: Optimal tunnel geometry

compared to their initial shape in figure 7.9a. These path plots show that the height of initial and optimal structures are nearly equal but the shape of the tunnel cross section changes seriously. The catenary curve at the center of the tunnel corresponds to the optimal shape of an arch under dead load which can be verified analytically and by experiments. The shape at both ends of the tunnel differs from the catenary curve. This is caused by the Poisson effect which governs the structural response at the tunnel ends. The improved objective function is depicted in figure 7.9b. It shows that the

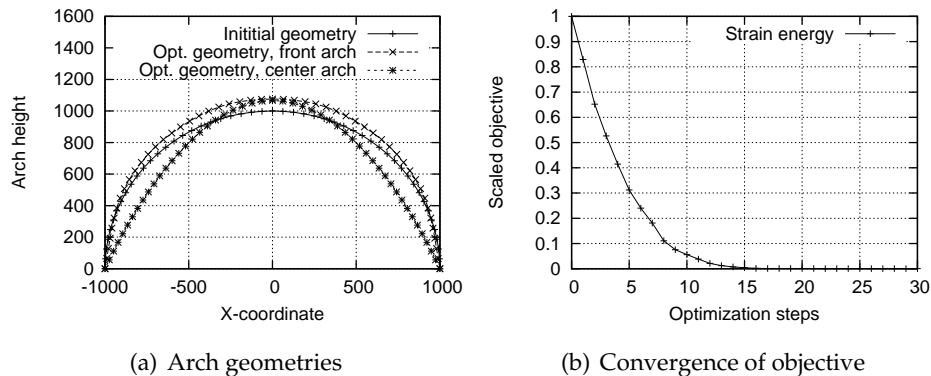


Figure 7.9: Optimal design of Model Problem VII

structural strain energy formulated by equation 7.1 is reduced significantly during the optimization procedure. After 30 optimization steps the optimal structure contains only 0.07% of the initial strain energy.

In the following the critical load and the imperfection sensitivity of the optimal structure should be investigated. The load-displacement curves of

the perfect and imperfect optimal design are computed until failure occurs. The imperfection mode is computed by summation of the four smallest eigenmodes of the optimal tunnel geometry. The shape of these modes is similar to eigenmodes of the initial design shown in figure 7.7. Also for this imperfection mode the absolute tolerance is specified by 1.0mm. The resulting load-displacement curves are presented in figure 7.10. It is easy

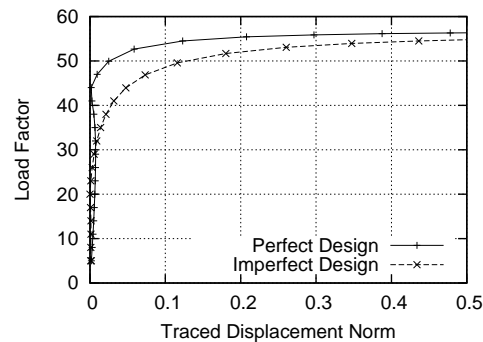


Figure 7.10: Load displacement curve

to verify that the critical loads of the optimized geometries are significantly higher compared to the imperfect initial design (figure 7.6). Much more important is the tremendous improvement of stiffness which results in a significant reduction of displacements. After reaching the respective critical loads also the optimized structures fail by buckling mode 1, c.f. figure 7.7.

The analysis of the optimal design subjected to the imperfection mode shows a slightly decreased critical load and a smoother transition in the failure mode. Comparing figures 7.6 and 7.10 one can verify that the reduction of the critical load due to imperfections of the optimal design is much smaller than for the initial design. Hence, in this model problem the optimal design is less imperfection sensitive than the initial design.

7.7 Summary

This chapter presents an efficient and robust method to combine nonlinear path following strategies with gradient based shape optimization. The derivations and the example show that consideration of nonlinear kinematics in the sensitivity analysis results in highly efficient designs. It has to be stated that the solution of geometrically nonlinear shape optimization problems is numerically much more expensive compared to geometrically

linear problems. This is caused by the more complicated system evaluation which requires several iterations until convergence. Additionally, the size of the maximum step length in the line search procedure is in general smaller. Figure 7.3 shows the iteration procedure for a fixed load level λ^* . Especially for weak initial designs and large load levels there might be a significant difference between the displacements of the current and the updated design. Whenever these differences are too large the nonlinear analysis does not converge. This problem can be solved by smaller step lengths which yield at the same time to more iteration steps and therefore to an increased numerical effort.

Chapter 8

Examples

The examples discussed in this chapter illustrate performance and application fields of the presented optimization algorithms, the parametrization technique, the sensitivity analysis, the sensitivity filter and the mesh regularization methods. The optimization tasks are motivated by real life problems from civil engineering and automotive industry.

8.1 L-shaped Cowling

This shape optimization example was originally proposed by D. Emmrich in his PhD thesis [Emm05]. It describes the stiffening of a bending dominated cowling structure by beads. The geometry, the material data and the supports are equal to the model proposed in [Emm05].

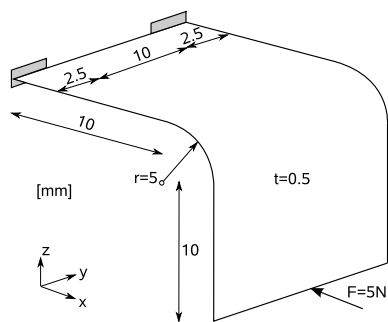


Figure 8.1: Cowling geometry

The cowling structure is clamped near both sides of the upper blank. The length of each clamping is equal to 2.5mm. In contrast to the problem proposed by Emmrich the loading acts perpendicular to the lower flat part of the cowling. In [Emm05] the loading acts as a tension force in z-direction. Thus, the lower flat part of the cowling transfers the loads via membrane loading. For the optimization example shown here

the loading acts in x-direction. This results in a bending load of the whole structure. It should be noted that the chosen thickness and geometry result in a very thick shell with an radius to thickness ratio of 10.

The goal of this optimization problem is minimization of linear compliance (3.32) with geometric constraints. These constraints limit the height of the

resulting beads to 2.5mm. Furthermore it is enforced that the dimensions (width and height) of the cowling remain constant. The optimization variables are defined as the directors of the FE-nodes. The optimization starts with the initial design depicted in figure 8.1.

This relatively simple shape optimization problem should be used to visualize

- the effect of a varying filter radius and
- the mesh and parametrization independency of the proposed methods.

Therefore, the results of three different filter radii ($r=1\text{mm}$, $r=2\text{mm}$ and $r=3\text{mm}$) are compared. The parametrization independency is investigated by FE-models with 1650, 3735 and 6600 shell elements.

8.1.1 Filter Radius as Design Tool

The influence of the filter radius is shown on the finest discretization with 6600 finite elements and 6771 design variables. Figure 8.2 compares the optimal geometries after 30 iteration steps. The dependency on the filter radius is clearly visible. The bead structure obtained for $r=1\text{mm}$ shows local beads at both sides of the cowling and a relatively flat inner part. This results in an explicit bead structure that is well suited to transfer the load to the supports. Increasing the filter radius (c.f. figure 8.2b and 8.2c) gives an increased bead width. The resulting geometries show reduced curvatures and a smoother shape. But the crucial question is how much does the increased filter radius affect the mechanical properties of the structure? In this example the mechanical properties are measured by the compliance

design	$ d $	scaled $ d $	compliance	scaled compliance
initial	0.742	1.0	1.666	1.0
$r=1\text{mm}$	0.047	0.063	0.113	0.068
$r=2\text{mm}$	0.033	0.044	0.079	0.047
$r=3\text{mm}$	0.045	0.061	0.109	0.065

Table 8.1: Displacements and compliance of cowling designs

and the displacements at the loaded node. The convergence plot depicted in figure 8.2d shows that all the three optimizations reach nearly the same

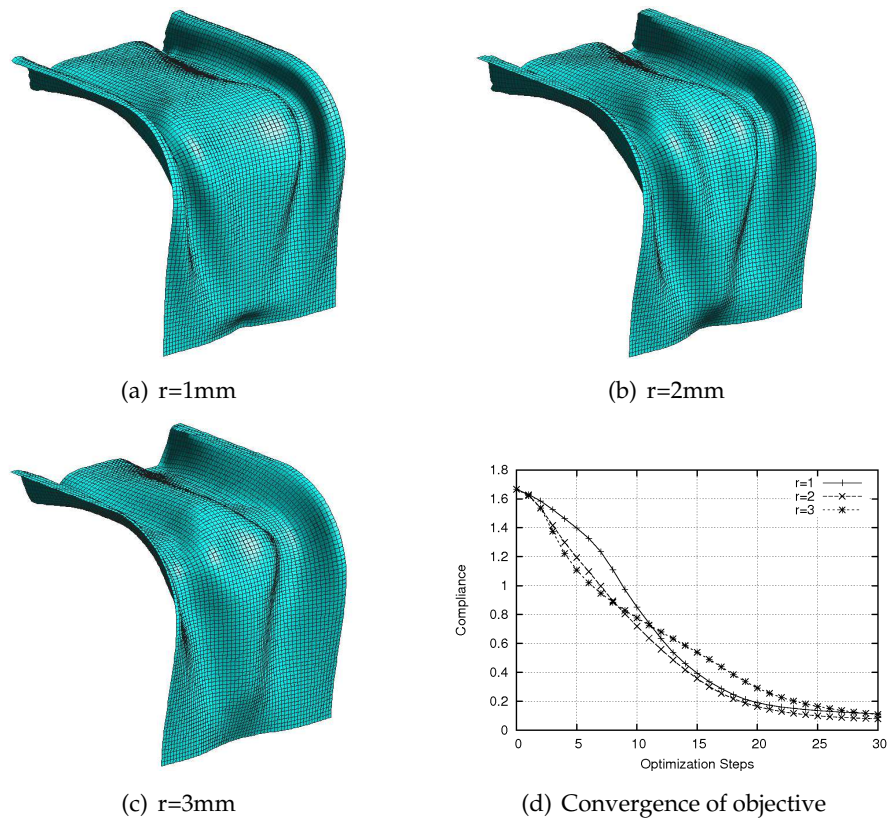


Figure 8.2: Optimal cowling geometries

objective value after 30 iteration steps. The specific values are listed in columns 4 and 5 of table 8.1. They differ only slightly compared to the initial compliance value. A similar behavior is observed by comparing the displacement norms of the loaded node. These displacements show that all three designs are efficient improvements of the initial design but the displacements of the optimized designs are nearly equal.

Comparing compliance and displacements substantiates that a variation of the filter radius yields to different designs with similar mechanical properties. Thus, the filter radius can be used as a design tool to explore the space of optimal solutions. All the resulting designs are efficient improvements of the initial model with similar performance. Finally, the designer can choose between different optimal designs according to his own subjective measures.

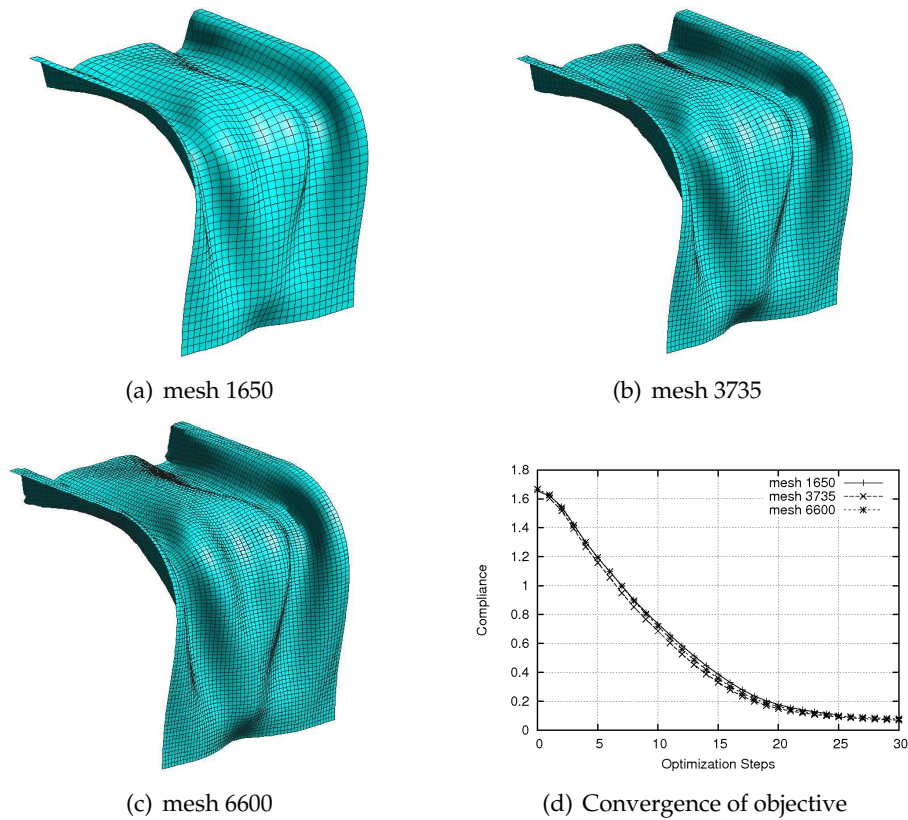


Figure 8.3: Mesh independent optimal geometry

8.1.2 Mesh and Parametrization Independency

In order to show the parametrization independency of the proposed optimization method a fixed filter radius of 2mm is chosen. The cowl geometry is discretized by three grids with 1650, 3735 and 6600 shell elements. The parametrizations defined by these three grids contain 1736, 3864 and 6771 optimization variables, respectively. The optimization results are visualized in figure 8.3. Obviously, all three optimization problems give the same result. The only difference is the parametrization that is applied to represent the optimal geometry. This is also shown by the convergence graphs depicted in figure 8.3d. The three optimization problems show a similar convergence behavior and reach the same optimum with a compliance value of approximately 0.07.

It should be stated that the parametrization independency is only obtained if the optimal geometry can be represented with sufficient accuracy. It is well known that a sufficient mesh density of finite element analysis de-

depends on the geometry, the boundary conditions, the applied finite elements, etc. In structural optimization also the applied response functions, the constraints and the filter radius have to be considered before choosing a parametrization. Thus, establishing general guidelines for a sufficient mesh density is not possible.

Nevertheless, many optimization problems result in parametrization independent solutions if the edge length of the finite elements l_{ele} and the filter radius r fulfill the relation

$$\frac{r}{l_{ele}} > 4. \quad (8.1)$$

Thus, the whole filter function spans at least over 8 elements. This usually ensures a relatively smooth approximation of the optimal geometry.

The property of parametrization independency is very important for shape optimization methods. It ensures that the optimal design is not restricted by the chosen design space. Parametrization independency can only be obtained if regularization methods like the proposed sensitivity filter are applied. Common parametrization techniques like CAGD, Morphing or shape basis vectors do not contain such approaches. Thus, the optimal results obtained by these methods strongly depend on the chosen parametrization.

8.2 Kresge Auditorium

The Kresge Auditorium is situated on the campus of the Massachusetts Institute of Technology. The reinforced concrete structure was finished in 1955 based on the design of the famous architect Eero Saarinen.



Figure 8.4: Kresge Auditorium (wikipedia.org)

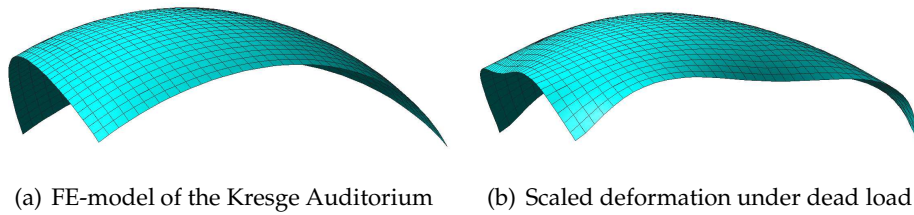


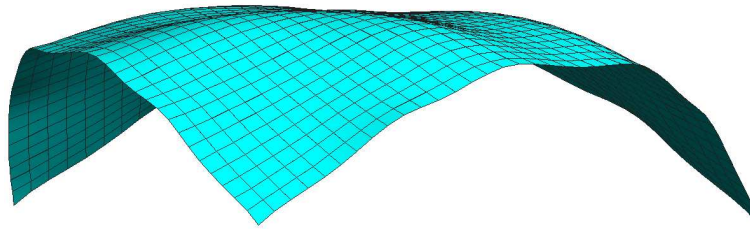
Figure 8.5: Analysis of original Kresge Auditorium

The shape of the structure is one-eighth of a sphere rising to a height of approx. 14m with a span of approx. 50m. One basic property of this shell structure is the small thickness which increases from 8.5cm at the center to 14cm at the supports. As presented in figure 8.4 massive edge beams with a height of nearly 100cm are necessary to stabilize the structure at the free edges.

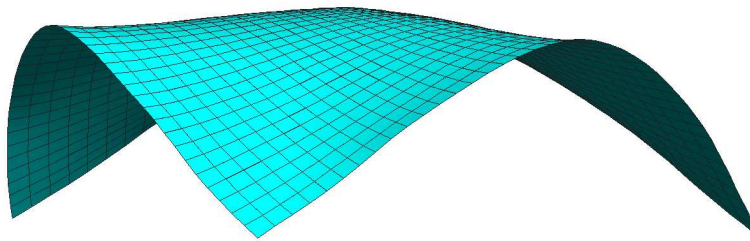
The structural behavior of the original Kresge Auditorium under dead load is investigated by the following analysis. To show the basic deficiencies of the shape the edge beams are omitted. The shell thickness is assumed to be constant with a value of 5cm. 1200 bilinear Reissner-Mindlin shell elements with a linear elastic material formulation are applied for discretization. The values for Young's modulus, Poisson's ratio and density are chosen according to usual concrete parameters with $30E09N/m^2$, 0.2 and $2400kg/m^3$ respectively. For the subsequent computations the Assumed Natural Strain (ANS) method is used to prevent locking problems. Single point constraints on displacement degrees of freedom are defined on the three boundary nodes at the corners of the structure.

Figures 8.5a and 8.5b show the original spherical geometry as well as a scaled displacement plot. It is easy to see that the distribution of structural stiffness is very inhomogeneous. The center region shows nearly no deformation whereas the boundary arches and the corner regions are deformed seriously. In the original structure these deformations are prevented by variation of shell thickness and massive edge beams. Based on the depicted structural displacements it can be stated that the chosen shape is not optimal. Especially the boundary arches and the support regions offer serious potential to optimization.

In the following, FE-based shape optimization is used to improve the load carrying behavior of the structure. The strain energy is an appropriate measure to describe the efficiency of load carrying behavior. In this example the linear (equation 3.32) and nonlinear (equation 7.1) strain energy formula-



(a) Linear strain energy



(b) Nonlinear strain energy

Figure 8.6: Optimal shapes for Kresge Auditorium

tions are applied as objective functions in order to discuss the respective results. The design space is described by the normal directions of the inner shell nodes and the vertical directions of the nodes situated on the boundary arches. This ensures that the area below the cupola remains unchanged. Gradients of linear and nonlinear strain energy are filtered by cubic filter functions with a radius of 10m which corresponds to 20% of the span. Mesh quality is controlled by the regularization method introduced in section 6.3. The optimal shapes shown in figure 8.6 are serious improvements of the original geometry. Both designs carry most of the loads by membrane action whereas the load carrying of the Kresge Auditorium is dominated by bending, especially near the corners. A detailed investigation of the depicted designs shows significant differences. Minimization of linear compliance (figure 8.6a) gives an inhomogeneous design with serious local curvature. This is caused by the fact that during optimization the designs are dominated by bending. In the geometrically linear optimization the bending stiffness is increased by increasing local curvature. Due to the non-convexity of the response function these curvatures prevent a convergence to the analytical reference solution. The wave length of the linear optimiza-

tion result is related to the filter radius. Modifications of the filter function would result in different wave designs.

The geometrically nonlinear analysis is formulated in the deformed configuration where additional membrane stiffness is activated. This additional membrane stiffness influences the gradients and also the design updates. All intermediate designs and also the final design show less curvature and work nearly completely in membrane action compared to geometrically linear designs. The nonlinear result is closely related to the analytical result of a hanging form [BWDC05]. It shows the typical anticlastic shape which is known from form finding of membrane structures. In the nonlinear optimization the filter radius has only a small influence because the gradients are already relatively smooth.

In order to compare the efficiency of the different designs (figures 8.5a, 8.6a and 8.6b) three geometrically nonlinear analysis are performed to evaluate the structural behavior. The resulting load displacement curves are presented in figure 8.7. They show the vertical displacement of the center point for an increasing load factor. It is easy to verify that the original geometry of the Kresge Auditorium reacts very soft. Due to the displacements depicted in figure 8.5b the structure is not able to transfer higher loads to the supports.

The design obtained by geometrically linear optimization shows a much better load carrying behavior at least for small load factors. Increasing the load factor results in a serious weakening of the structure and to increased displacements. Here a load factor of 0.76 results in a vertical displacement of 0.1m. The displacements close to the support region are even larger.

The best load displacement behavior is obtained by the analysis of the nonlinearly optimized design (figure 8.6b). This structure reacts extremely stiff and shows a sudden failure for a load factor of 0.85. The most important property are the small displacements of only 1.3cm at the failure load. This proves the efficiency of the shape optimization based on nonlinear kinematics. The resulting designs show superior structural properties and aesthetic qualities compared to linear results.

A crucial question of highly optimized thin shell structures is their sensitivity to geometrical imperfections. In general, stiffer structures (figures 8.6a and 8.6b) are more sensitive than weaker structures (figure 8.5a). In the following the imperfection sensitivity of each design is determined by a nonlinear analysis of a perturbed design. The respective imperfection mode is computed by a combination of the four smallest eigenmodes, c.f. equation

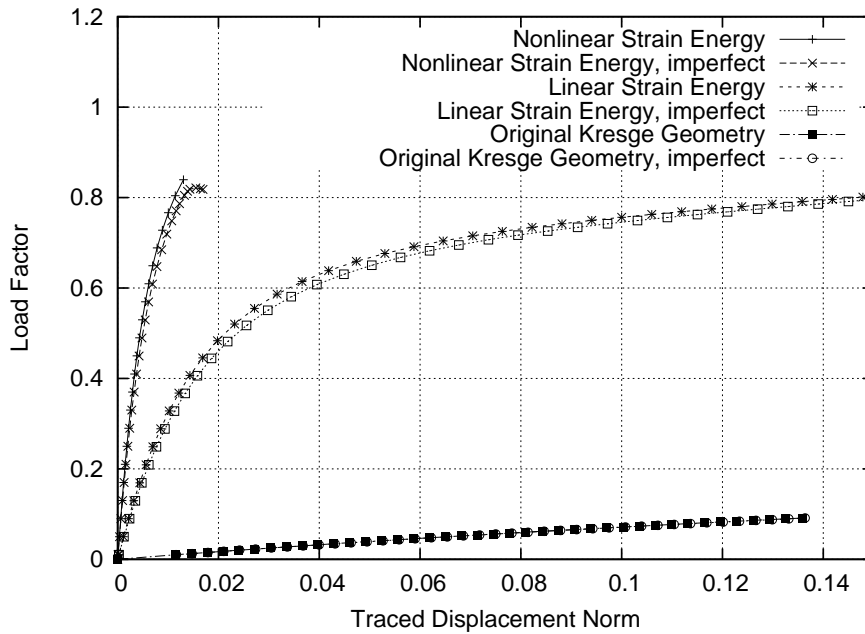


Figure 8.7: Load displacement behavior

7.7. The imperfection tolerance is defined by 2.5cm which corresponds to one half of the shell thickness. The resulting load displacement curves are also plotted in figure 8.7. It is easy to verify that the imperfect optimal designs react slightly weaker than the perfect designs. The critical load of the nonlinear optimization result decreases from 0.85 to 0.82 whereas the linear optimized design shows an even smaller imperfection sensitivity.

It can be summarized that the final design of the shape optimization procedure considering nonlinear kinematics is characterized by optimal structural properties, small imperfection sensitivity and high aesthetic quality. A slightly enlarged shell thickness near the corners would result in an extremely efficient long span structure which is able to resist dead, snow and wind load with a minimal weight. FE-based structural optimization utilizing nonlinear kinematics is the best suited tool to develop such powerful structures.

8.3 Car Hat Shelf

Structural optimization is a very important issue in automotive industry. The large number of different components, the decreasing design cycles and the mass production provide a broad application field for topology,

shape and sizing optimization. In general, optimization goals in automotive industry are related to weight minimization, reduction of CO₂ emission, cost minimization, improved crash safety, improved stiffness, etc. The optimization of crash behavior is a very important and also a very challenging objective. Unfortunately it is mostly impossible to derive a direct relation between crash parameters like intrusions or accelerations and the design variables like blank thicknesses or shape parameters of the car body. Hence, the crash optimization is mostly based on response surface models which are constructed by design of experiments (DOE) methods. Other objectives like improved stiffness of car components or optimization of frequency behavior are well suited for gradient based optimization strategies. Thus, the presented examples show the performance of FE-based shape optimization of thin metal structures which are typically applied to form the car body. The mechanical properties of these structures are predominantly defined by their shape. It is shown that an optimal shape guarantees highly efficient load carrying and frequency behavior. This ensures structural efficiency and minimal weight which yield to minimal CO₂ emissions.

There exist several implementations of bead optimization strategies in commercial optimization software. The company "FE-Design GmbH" uses a method based on trajectory lines of bending moments [Emm05] in their software "TOSCA Structure". According to these trajectories the geometry is modified by predefined bead shapes. The basic drawback of this approach is that it does not incorporate the modified load carrying behavior during design changes.

The software package "OptiStruct" developed by the company "Altair Engineering, Inc." uses the so called topography optimization (c.f. section 4.2.4) to determine bead patterns. In this method a set of radial shape functions is applied to the mesh. The final bead structure is derived as a combination of shape deformations based on these functions.

The optimization software "Genesis" developed by "Vanderplaats Research and Development, Inc." applies a set of shape basis vectors [Lei10] to describe shape modifications. The resulting geometries are comparable to the results of topography optimization. They are less reliable due to mesh dependency and large element distortions. These results provide only a very abstract suggestion of a bead pattern and need serious interpretation by experienced designers.

The following example the FE-based parametrization technique is applied to frequency optimization of a hat shelf structure. The author thanks the Adam Opel GmbH for providing geometry and reference results. Figure

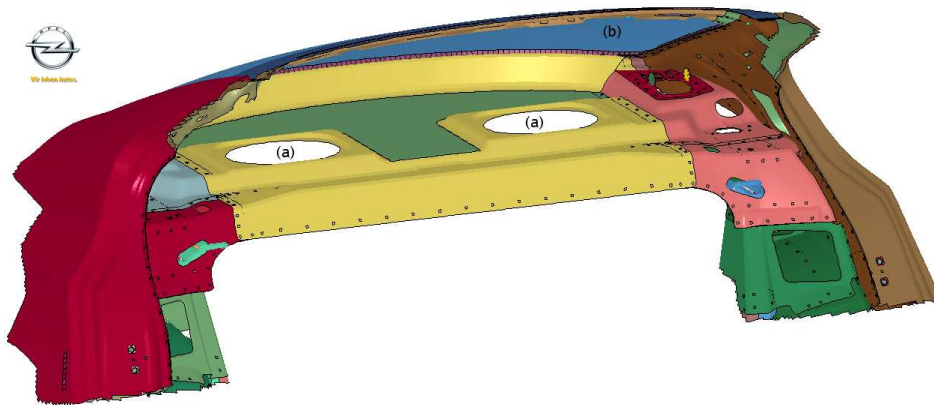


Figure 8.8: Car hat shelf and surrounding components

8.8 shows the hat shelf with some surrounding components. The holes for the loudspeakers (a) and the back window (b) are clearly visible. The frequency behavior of the inner car body is mainly responsible for the sound level inside the car. Structures that show resonance behavior with external excitations are very displeasing.

Before starting the shape optimization the frequency behavior of the hat shelf is analyzed. Therefore the hat shelf is extracted from the car body where single point constraints are applied at the positions of the spot welds in order to model structural supports. The geometry is discretized by Reissner-Mindlin shell elements with a thickness of 1mm and linear elastic material with Young's modulus equal to $210000N/mm^2$ and Poisson's ratio equals 0.3. The modal analysis is performed by solution of the eigenvalue problem (equation 3.27) for the five smallest eigenvalues. Figure 8.9 shows the initial geometry as well as the respective eigenmodes. One can clearly see that the modes are mainly restricted to the flat inner part of the hat shelf. The front and back parts of the structure as well as the region around the loudspeakers have a significantly higher stiffness because of their curved shape. The flat inner part has only a very small stiffness which yields to the depicted modes.

The mode distribution also provides a good estimation for a well suited design space in the following shape optimization. The main goal of the optimization is to improve the eigenfrequencies of the structure. Thus, the normal coordinates of all FE-nodes in the flat inner part are defined as design variables whereas the rest of the structure remains unchanged. This ensures an effective stiffening of weaker structural parts and allows for a

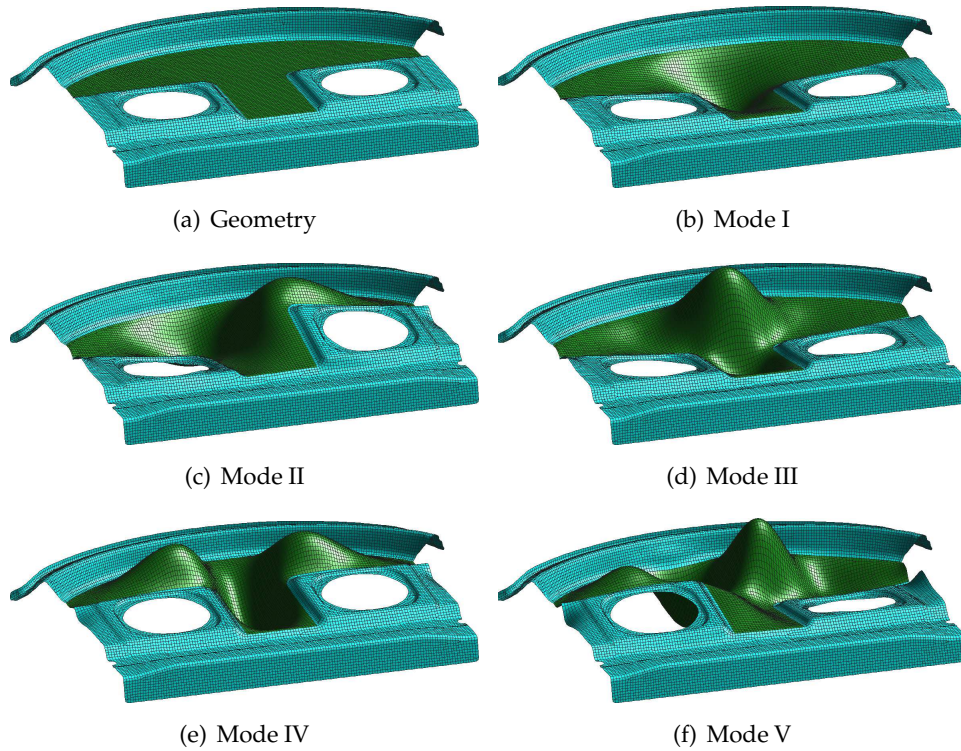


Figure 8.9: Modal analysis of hat shelf structure

considerably improved frequency behavior.

Many car body components are manufactured by deep drawing processes which motivates the improvement of the structure by draw beads. Such beads are mainly characterized by their height and their width. During shape optimization the allowable bead height of 8mm is enforced by proper variable bounds whereas the bead width is controlled by the filter radius of 40mm. The optimization goal of eigenfrequency maximization is formulated by the minimization of the function

$$f(\mathbf{s}) = - \sum_{j=1}^5 w_j F_j \quad (8.2)$$

with the eigenfrequencies F_j specified by equation 3.28 and a set of weighting factors $w_j = 1.0$. The derivative of (8.2) follows to

$$\frac{df}{ds_i} = - \sum_{j=1}^5 w_j \frac{dF_j}{ds_i} \quad (8.3)$$

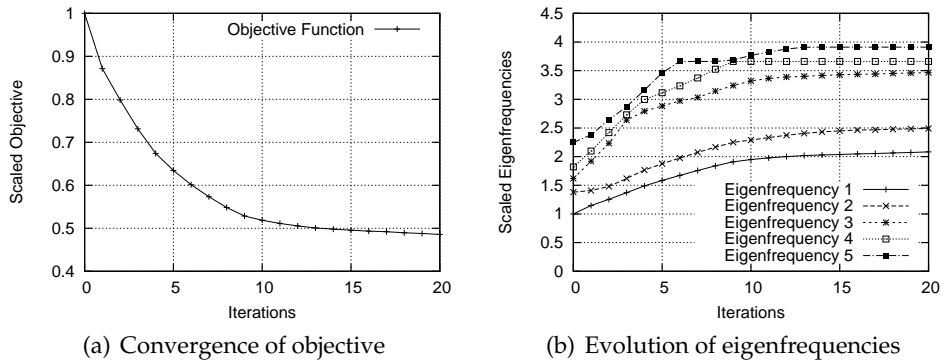


Figure 8.10: Frequency optimization of hat shelf

and provides the basis for the search direction computed by the conjugate gradient method, c.f. section 4.6.2.

The convergence of the objective function and the development of the considered eigenfrequencies is shown in figures 8.10a and 8.10b, respectively. Both figures verify the effective improvement of the frequency behavior. The smallest eigenfrequency is increased by a factor of 2.1 which is a serious improvement for this type of structures. Figure 8.10b additionally shows that there occurs no mode switching during the optimization process. This phenomenon has to be avoided because of its negative effects on stability and convergence of the optimization process. The resulting bead

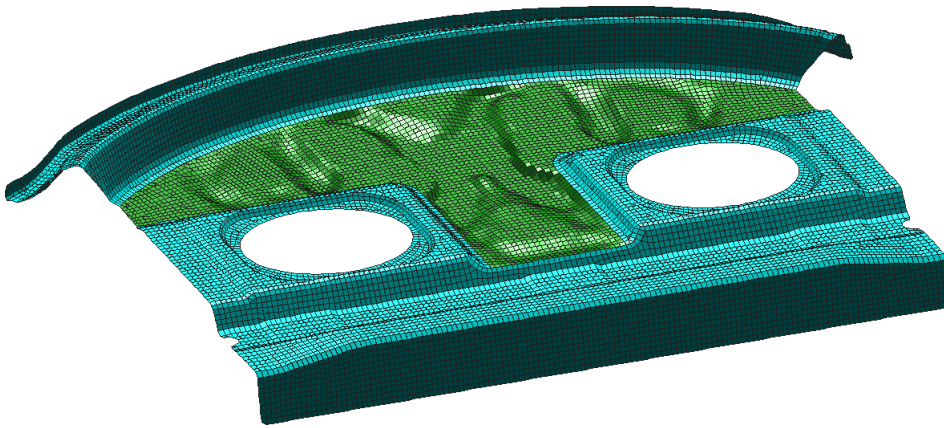


Figure 8.11: Optimized Bead Structure

structure is depicted in figure 8.11. It shows an efficient stiffening of the weak structural parts by connecting these areas with stiffer regions. These connections are realized by beads that allow for easy identification and in-

terpretation. Size and height of the beads additionally permit a quantification of their importance. The central X-shaped bead structure is the most important because it effectively reduces all 5 considered eigenmodes, c.f. figure 8.9b-f. Near the boundary of the structure the beads are relatively small. They mainly decrease the higher modes IV and V. During translation of the computed optimal geometry into a specific bead design they could be even neglected without serious degradation of structural frequency behavior.

The presented example shows that the concept of shape optimization with FE-based parametrization is ideally suited to solve eigenfrequency optimization problems with a minimum amount of modeling effort. The resulting bead structures improve the frequency behavior significantly such that no resonance behavior with external excitations occurs anymore. Figure 8.11 proves that the optimal bead design is mesh independent and reliable. Due to the high mesh quality these structures ensure exact numerical results and easy interpretability.

8.4 Luggage Trunk Ground Plate

The second bead optimization example is also provided by the Adam Opel GmbH. It shows the stiffness optimization of the luggage trunk ground plate by draw beads. This structure carries the luggage load and addition-

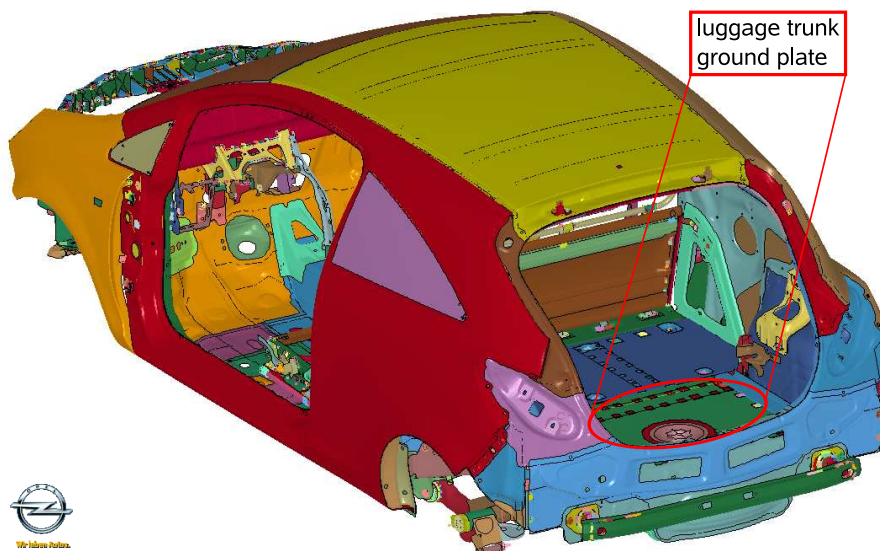


Figure 8.12: Back view of car body

ally serves as cover for the spare wheel. Figure 8.12 shows a back view into the respective car body. The luggage trunk, its surroundings and the fastener for the screw above the spare wheel are easy to identify. This trunk plate is usually made of a thin metal sheet which is stiffened by some beads. Unfortunately there exists a huge variety of possible bead structures which improve the mechanical properties of the design. Usually the design engineer creates a proper bead structure based on experience and former designs. But in general, the bead design created by a numerical shape optimization scheme is significantly better.

Before starting the bead optimization procedure the mechanical model has to be analyzed. Therefore the ground plate is subjected to a vertical surface load. The displacements at the points where the ground plate is connected to the surrounding car body are constrained by single point constraints, c.f. figure 8.13. The structure is discretized by Reissner-Mindlin shell elements with a thickness of 1.0mm and linear elastic material with Young's modulus equal to $210000N/mm^2$ and Poisson's ratio equals 0.3. Figure 8.13 shows a contour plot of the displacements for the applied surface load. It

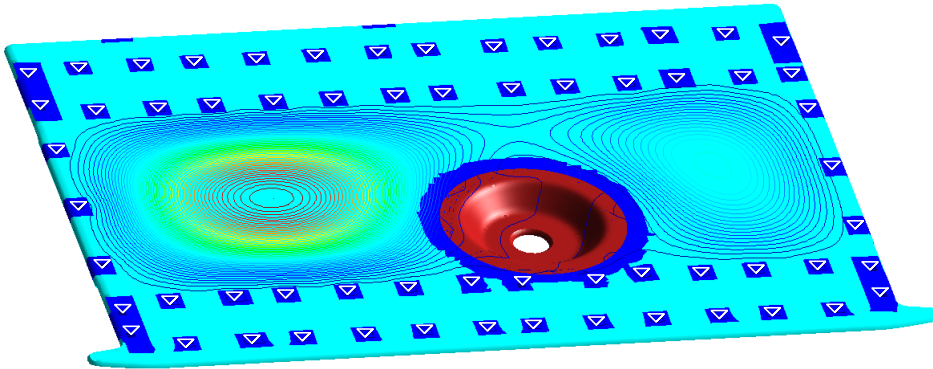


Figure 8.13: Displacements of luggage trunk ground plate

is easy to observe that the displacements concentrate on the flat inner parts of the structure whereas the displacements on the left are larger than the displacements on the right. This is caused by the non-symmetric fastener of the spare wheel screw which acts as a local stiffener. In general the load carrying of this design is dominated by bending which results in relatively large displacements and stresses.

The main goal of the shape optimization process is to decrease the displacements by improving structural stiffness. This aim is conveniently formulated by the linear strain energy, c.f. equation 3.32. For this component the

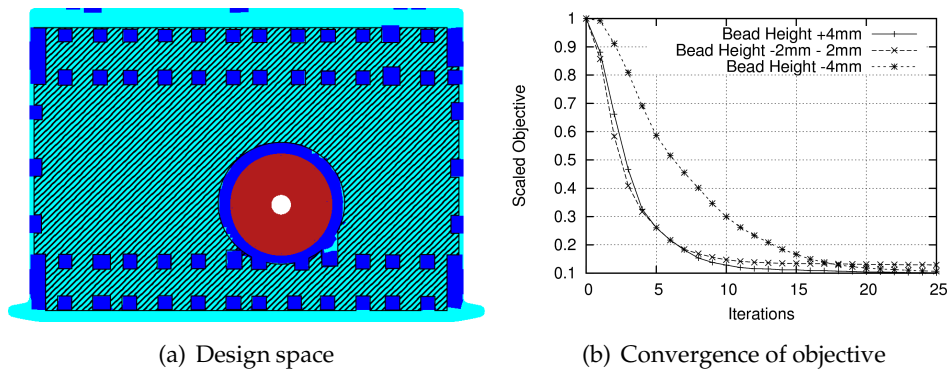


Figure 8.14: Optimization of luggage trunk ground plate

bead height is limited to 4mm in order to guarantee a maximum loading capacity. Higher beads would increase the structural stiffness but they also would decrease the volume of the luggage trunk. The filter radius which controls the bead width is chosen with 30mm. Figure 8.14a shows the design space of this optimization problem by the hatched domain. All inner FE-nodes except of the support nodes and the region around the fastener of the spare wheel screw are design nodes. The design space is formulated by the vertical coordinates of the design nodes. Beside bead height and bead width the orientation of the beads serves as additional design parameter. Figure 8.15 visualizes three possible bead geometries for the bead height of 4.0mm. The influence of the bead orientation on the objective and on

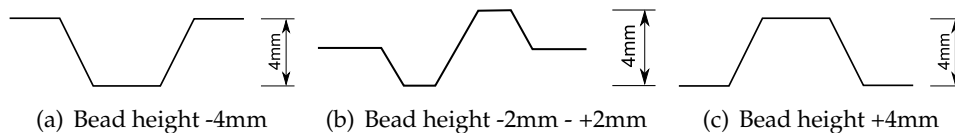
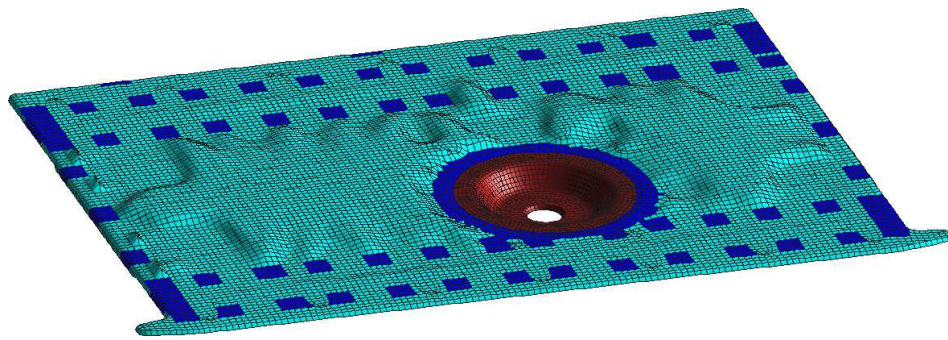
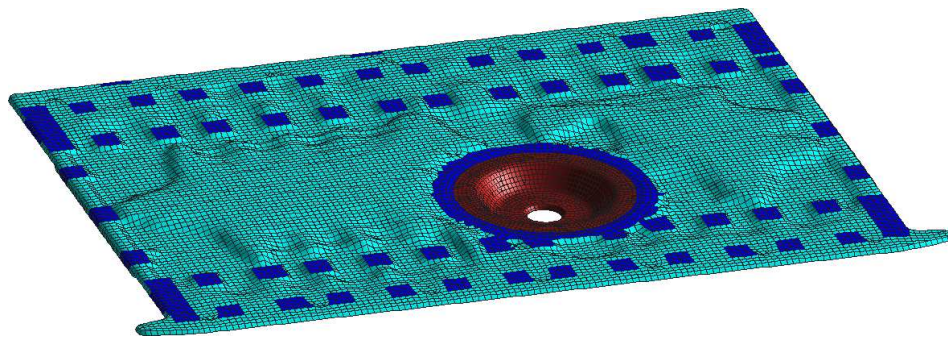


Figure 8.15: Bead orientations

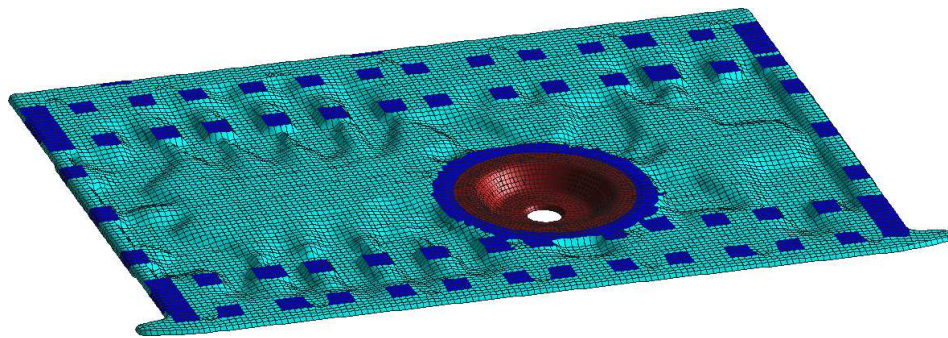
the resulting bead structure is investigated by the following three results. Figure 8.14b proves that all 3 optimizations yield to a similar results but the convergence speed shows significant differences. Especially the optimization run with the bead height -4mm needs more iteration steps to reach an adequate minimum. This is caused by the fact that the unconstrained search direction predominantly points in positive z-direction and therefore directly towards the constraints. During the optimization procedure the search direction changes its direction to the negative z-direction and the geometry updates start to develop. Finally, the quality of the optimum is



(a) Bead height +4mm



(b) Bead height -2mm - +2mm



(c) Bead height -4mm

Figure 8.16: Bead structures for luggage trunk ground plate

nearly as good as the optimum of the optimization run with bead height +4mm. Figure 8.16 compares the bead structures that result from the different bead orientations. It can be easily observed that all bead structures are characterized by high quality, easy interpretability and mesh independency. Although the geometry of the bead designs look slightly different all three results ensure an effective improvement of the mechanical properties of the structure.

This is another example that shows the non-convexity of general shape optimization problems. Many of these problems have several minima with very similar structural properties. Beside the classical objectives and constraints the optimization algorithm has to be formulated such that the final results additionally fulfill constraints with respect to aesthetic quality, manufacturability and mesh independency. If such an optimum is found it is usually a tremendous improvement of the initial design and therefore an satisfactory solution of the optimization problem.

Chapter 9

Summary

The methods presented in this thesis are an important contribution to shape optimization with FE-based parametrization. It was shown that optimization problems formulated on a large design space supplemented by additional regularization operators result in general, robust and very efficient optimization results. The proposed methods require only a minimum modeling effort and can be applied to many different optimization problems. The investigated examples show an application to problems from civil engineering and automotive industry. In general, each FE-based simulation can provide a basis for FE-based optimization as soon as direct relations between optimization goals and design parameters can be derived. Utilizing this relation the adjoint sensitivity analysis allows for a very efficient computation of gradient information. With this data the most powerful optimization strategies can be applied in order to compute highly efficient designs. These designs show the large potential which is usually hidden in non-optimized structures. It is a basic objective of each engineer to develop designs that are as efficient as possible. Shape optimization methods applying FE-based parametrization and regularization are very powerful tools to achieve this goal.

9.1 Modeling Effort

In the past, the large modeling effort for parametrization of shape optimization problems, e.g. by CAGD, Morphing or Shape Basis Vectors, was a serious drawback that prevents a broad application of these methods. It was shown that FE-based parametrization is a general and easy parametrization technique for many types of optimization problems. This method requires only a minimal effort, does not need time consuming reparametrization steps and can be easily integrated in automated processes. Additionally

the optimization problem is defined on a large design space which does not restrict the optimal shape of the investigated structure. Also the proposed regularization methods require just a minimum amount of modeling effort. They provide effective control mechanisms for the geometry and the discretization which is a prerequisite for successful application of FE-based parametrization techniques.

9.2 Numerical Effort

The solution of optimization problems is in general more expensive than a simple analysis of the respective mechanical problem. The most time consuming components of gradient based optimization strategies are sensitivity analysis and system evaluations. The relation of these components with respect to numerical effort is mainly governed by the number of response functions, the number of design variables and the number of degrees of freedom in the mechanical problem. By application of FE-based parametrization the latter two quantities are usually characterized by the same magnitude. It can be stated that the numerical effort of the adjoint sensitivity analysis (c.f. section 4.3.4) for a few number of response functions becomes negligible for large mechanical problems with more than 10^6 degrees of freedom under the prerequisite that the adjoint variables can be computed by simple backsubstitution. Usually, the numerical effort for the solution of a system of equations increases quadratically with the size of the equation system, at least for direct solvers. But the effort for the adjoint sensitivity analysis increases just linearly with the number of design variables and the number of response functions. Thus, the numerical effort of large optimization problems is usually dominated by the number of system evaluations. The required number of these evaluations is mainly governed by the line search procedure, c.f. section 4.8. Usually, line search methods based on approximation techniques provide the best compromise between accuracy and efficiency.

9.3 Parallelization

Gradient based optimization strategies based on FE-based parametrization and adjoint sensitivity analysis are ideally suited for application to massive parallel computer environments. Such architectures are formed by many separate computers called nodes which are connected by powerful

network systems. These computers require a spatial decomposition of the optimization problem and the mechanical problem. Then the full problem can be solved by the parallel computer where the communication between the processes can be realized by the Message Passing Interface (MPI). All of the presented optimization strategies including system evaluation, sensitivity analysis and regularization were implemented in a fully parallelized way to ensure optimal scalings. Thus, the solution time of shape optimization problems can be reduced by adding more nodes. In the same way restrictions with respect to main memory can be circumvented by a fine grained domain decomposition. The parallel implementation of shape optimization algorithms permits the solution of very large problems with 10^6 or even more design variables in an adequate time.

9.4 Applicability to Industrial Problems

The examples presented in chapter 8 show the applicability of the proposed methods to industrial shape optimization problems. The computed results are robust, mesh independent and highly qualitative. In the past, the complicated and time consuming parametrization derogates a broad application of shape optimization techniques in industry. Topology optimization problems are always formulated by FE-based parametrization which results in wide spread application fields in many disciplines. By utilization of the proposed regularization techniques FE-based shape optimization requires nearly no modeling effort which allows for many new application fields in the future. Due to parallel implementation of the algorithms huge optimization problems formulated on highly complicated mechanical scenarios can be solved in proper time.

A very important part of industrial optimization problems is the back transformation of the optimized geometry into CAD formats. This can be done either by experienced designers or by automatic tools which transfer mesh data to tensor product formulations like NURBS.

9.5 Outlook

The proposed optimization framework is generally applicable to many optimization problems. The type of optimization is mainly characterized by the objective and the optimization variables. Several response functions and their derivatives are presented in section 3.4. Following the presented

ideas with respect to adjoint differentiation many other functions can be formulated and derived. Thus, a broad spectrum of different optimization problems can be solved.

The proposed algorithms and examples are related to shape optimization problems using geometrical parameters as design variables. Nearly all of the presented methods are also applicable to sizing and material optimization. Usually, these optimization problems and especially the sensitivity analysis are less complex than optimization with respect to geometrical parameters. Especially the presented sensitivity filter applies in the same way to thickness optimization problems of shells preventing the well known checkerboard modes.

An important and yet unsolved problem is presented in section 4.5. It describes the size effects that result from the chosen parametrization in the discrete sensitivity analysis, c.f. section 4.3.2. In FE-based shape optimization problems this effect becomes visible for unstructured grids in combination with large size differences of the finite elements. Efficient methods to reduce these negative effects are presented in section 4.5. Nevertheless this effect has to be investigated by future research.

List of Figures

1.1	Hanging forms	2
1.2	Membrane design by soap film analogy	3
2.1	Geometry and kinematics of curved 2-d bodies	7
3.1	Graphical interpretation of KKT conditions at the optimum	16
3.2	Fiber angles and stacking sequence of composite material	24
3.3	Cross section designs of a truss beam structure	25
3.4	Shape designs of a truss beam structure	26
3.5	Topologies of a truss beam structure	27
3.6	Initial Scherk surface	30
3.7	Final Scherk surface	30
3.8	Initial catenoid surface	30
3.9	Final catenoid surface	30
3.10	Buckling modes of quadratic plate	33
3.11	Buckling optimized geometry of quadratic plate problem	34
3.12	Stiffness optimized geometry of linear quadratic plate problem	36
3.13	Nonlinear load displacement curve	37
3.14	Stiffness optimized geometry of nonlinear quadratic plate problem	38
4.1	Convex function	43
4.2	Non-convex function	43
4.3	Design variables for shape derivatives	47
4.4	Methods for sensitivity analysis	48

4.5	Constrained design update	55
4.6	Initial catenoid design	55
4.7	Constrained catenoid	55
4.8	2-d Domain	56
4.9	2-d Truss model	56
4.10	Wall model	58
4.11	Discretizations of 2-d Domain	59
4.12	Mass gradients	60
4.13	Strain energy gradients	60
4.14	CG / SD optimization algorithm	63
4.15	Method of Feasible Direction	64
4.16	MFD optimization algorithm	67
4.17	ALM optimization algorithm	70
4.18	Quadratic line search	72
5.1	Dofs of beam elements	76
5.2	Length perturbation by ΔL	76
5.3	Cantilever with tip moment	79
5.4	$d\mathbf{u}_b/dL$ and $d\mathbf{u}_t/dL$ for MP I	80
5.5	$d\mathbf{u}_b/dL$ and $d\mathbf{u}_t/dL$ for MP II	81
5.6	Modified sensitivities for Model Problems I and II	83
5.7	Orthogonalization of ϕ_r^2	85
5.8	Interpolated director	86
5.9	Nodal DOF of a 6 parameter Reissner-Mindlin shell	87
5.10	Model Problem III	89
5.11	Scaled sensitivities for Model Problem III	90
5.12	Model Problem IV	90
5.13	Scaled sensitivities for Model Problem IV	92
6.1	Objective with noise	98
6.2	Filter functions	99
6.3	Smoothed sensitivities	100

6.4	2-d Filter functions with radius $r=3$	101
6.5	Enlarged support due to smoothing operator	102
6.6	2-d Quadratic example function	103
6.7	Error propagation of Example III	103
6.8	Max. mean curvature	104
6.9	Smoothing results	105
6.11	"Optimal" Solutions	106
6.10	Initial configuration	106
6.12	Mesh regularization by Laplace smoother	108
6.13	Configurations for MSR	114
6.14	Designs for Model Problem V	117
6.15	Geometry, support and loading of quadratic plate	118
6.16	Optimal design for Model Problem VIa	119
6.17	Path plots for Model Problem VIa	120
6.18	Convergence of objectives for Model Problems VIa and VIb .	120
6.19	Path plots for Model Problem VIb	121
7.1	Nonlinear strain energy	126
7.2	Approximated strain energy	126
7.3	Geometrically nonlinear optimization procedure	129
7.4	Simultaneous analysis and optimization procedure	130
7.5	Tunnel shell	131
7.6	Load displacement curve	131
7.7	Eigenmodes of cylindrical tunnel shell	132
7.8	Optimal tunnel geometry	133
7.9	Optimal design of Model Problem VII	133
7.10	Load displacement curve	134
8.1	Cowling geometry	136
8.2	Optimal cowling geometries	138
8.3	Mesh independent optimal geometry	139
8.4	Kresge Auditorium (wikipedia.org)	140

8.5	Analysis of original Kresge Auditorium	141
8.6	Optimal shapes for Kresge Auditorium	142
8.7	Load displacement behavior	144
8.8	Car hat shelf and surrounding components	146
8.9	Modal analysis of hat shelf structure	147
8.10	Frequency optimization of hat shelf	148
8.11	Optimized Bead Structure	148
8.12	Back view of car body	149
8.13	Displacements of luggage trunk ground plate	150
8.14	Optimization of luggage trunk ground plate	151
8.15	Bead orientations	151
8.16	Bead structures for luggage trunk ground plate	152

List of Tables

3.1	Summary of first order methods	21
3.2	Summary of second order methods	23
3.3	Buckling load factors	34
5.1	Perturbation parameters for MP III	89
5.2	Tip load $f(n)$	91
5.3	Perturbation for MP IV	91
8.1	Displacements and compliance of cowling designs	137

Bibliography

- [AHU58] K. Arrow, L. Hurwicz, and H. Uzawa. *Studies in Nonlinear Programming*. Stanford University Press, Stanford, CA, 1958.
- [AK07] H. Azegami and S. Kaizu. Smoothing gradient method for non-parametric shape and topology optimization problems. In *Proceedings of the 7th World Congress of Structural and Multidisciplinary Optimization, COEX Seoul, Korea*, pages 1752–1761, 2007.
- [AN07] M. Alexa and A. Nealen. Mesh editing based on discrete laplace and poisson models. In *Advances in Computer Graphics and Computer Vision*, volume 1, pages 3–28, 2007.
- [Aro04] J.S. Arora. *Introduction to Optimum Design*. Elsevier Academic Press, 2004.
- [AW05] J.S. Arora and Q. Wang. Review of formulations for structural and mechanical system optimization. In *Structural and Multidisciplinary Optimization*, volume 30, pages 251–272, 2005.
- [Bat95] K.-J. Bathe. *Finite Element Procedures*. Prentice Hall, edition 2, 1995.
- [Ben89] M. P. Bendsøe. Optimal shape design as a material distribution problem. In *Structural Optimization*, volume 1, pages 193–202, 1989.
- [BFLW08] K.U. Bletzinger, M. Firl, J. Linhard, and R. Wüchner. Optimal shapes of mechanically motivated surfaces. In *Computer Methods in Applied Mechanics and Engineering*, page in press, 2008.
- [BGH⁺94] M. P. Bendsøe, J. M. Guedes, R. B. Haber, P. Pedersen, and J. E. Taylor. An analytical model to predict optimal material properties in the context of optimal structural design. In *Journal of Applied Mechanics*, volume 61, pages 930–937, 1994.

- [BH88] B. Barthelemy and R.T. Haftka. Accuracy analysis of the semi-analytical method for shape sensitivity calculation. In *Mechanics of Structures and Machines*, volume 18, pages 407–432, 1988.
- [Bis99] M. Bischoff. *Theorie und Numerik einer dreidimensionalen Schalenformulierung*. PhD thesis, Institut für Baustatik, Uni Stuttgart, Report Nr. 30, 1999.
- [Ble90] K.U. Bletzinger. *Formoptimierung von Flächentragwerken*. PhD thesis, Institut für Baustatik, Uni Stuttgart, Bericht Nr. 11, 1990.
- [Ble93] K.U. Bletzinger. Extended method of moving asymptotes based on second order information. In *Structural and Multidisciplinary Optimization*, volume 5, pages 175–183, 1993.
- [BLM00] T. Belytschko, W. K. Liu, and B. Moran. *Nonlinear Finite Element Analysis for Continua and Structures*. John Wiley and Sons, 2000.
- [BPS00] T. Buhl, C.B.W. Pedersen, and O. Sigmund. Stiffness design of geometrically non-linear structures using topology optimization. In *Structural Optimization*, volume 19, pages 93–104, 2000.
- [BR99] K.U. Bletzinger and E. Ramm. A general finite element approach to the form finding of tensile structures by the updated reference strategy. In *Int. Journal of Space Structures*, volume 14, pages 131–146, 1999.
- [BS94] S.C. Brenner and L.R. Scott. *The Mathematical Theory of Finite Element Methods*. Springer Verlag, 1994.
- [BS03] M. Bendsøe and O. Sigmund. *Topology Optimization*. Springer Verlag, 2003.
- [BSS94] H. Baier, C. Seeßelberg, and B. Specht. *Optimierung in der Strukturmechanik*. Vieweg Verlag, 1994.
- [BW08] J. Bonet and R. D. Wood. *Nonlinear Continuum Mechanics for Finite Element Analysis*. Cambridge University Press, 2008.
- [BWDC05] K.U. Bletzinger, R. Wüchner, F. Daoud, and N. Camprubi. Computational methods for form finding and optimization of shells and membranes. In *Computer Methods in Applied Mechanics and Engineering*, volume 194, pages 3438–3452, 2005.

- [Cam04] N. Camprubi. *Design and Analysis in Shape Optimization of Shells*. PhD thesis, Chair of Structural Analysis, TU Munich, Report Nr. 2, 2004.
- [Car76] M.P. Do Carmo. *Differential geometry of curves and surfaces*. Prentice Hall, Englewood Cliffs, 1976.
- [CGW91] G. Cheng, Y. Gu, and X. Wang. Improvement of semi-analytic sensitivity analysis and mcads. In N. Olhoff H.A. Eschenhauer, C. Mattheck, editor, *Engineering Optimization in Design Processes*, pages 211–223. Springer Verlag Berlin, 1991.
- [CGZ89] G. Cheng, Y. Gu, and Y. Zhou. Accuracy of semi-analytic sensitivity analysis. In *Finite Elements in Analysis and Design*, volume 6, pages 113–128, 1989.
- [CO93] G. Cheng and N. Olhoff. New method of error analysis and detection in semi-analytical sensitivity analysis. In G.I.N. Rozvany, editor, *Optimization of Large Structural Systems*, volume 1, pages 361–383, 1993.
- [Dao05] F. Daoud. *Formoptimierung von Freiformschalen, Mathematische Algorithmen und Filtertechniken*. PhD thesis, Chair of Structural Analysis, TU Munich, Report Nr. 4, 2005.
- [dBvKV02] H. de Boer, F. van Keulen, and K. Vervenne. Refined second order semi-analytical design sensitivities. In *International Journal for Numerical Methods in Engineering*, volume 55, pages 1033 – 1051, 2002.
- [EKO90] H. Eschenhauer, J. Koski, and A. Osyczka. *Multicriteria Design Optimization, Procedures and Application*. Springer-Verlag Berlin, Heidelberg, 1990.
- [Emm05] D. Emmrich. *Entwicklung einer FEM-basierten Methode zur Gestaltung von Sicken für biegebeanspruchte Leitstützkonstruktionen im Konstruktionsprozess*. PhD thesis, Institut für Produktentwicklung, Universität Karlsruhe, Bericht Nr. 13, 2005.
- [GLS09] S. Gaile, G. Leugering, and M. Stingl. Free material optimization for plates and shells. In *System Modeling and Optimization 23rd IFIP TC 7 Conference, Cracow, Poland*, pages 239–250, 2009.

- [HA89] R.T. Haftka and H.M. Adelman. Recent developments in structural sensitivity analysis. In *Structural Optimization*, volume 1, pages 137–151, 1989.
- [Har08] L. Harzheim. *Strukturoptimierung, Grundlagen und Anwendungen*. Verlag Harri Deutsch, 2008.
- [Hau02] P. Haupt. *Continuum Mechanics and Theory of Materials*. Springer Verlag, 2002.
- [HCK86] E.J. Haug, K.K. Choi, and V. Komkov. *Design Sensitivity Analysis of Structural Systems*. Academic Press, Inc., 1986.
- [HG92] R. T. Haftka and Z. Gürdal. *Elements of Structural Optimization*. Kluwer Academic Publishers, 1992.
- [HK89] R.T. Haftka and M.P. Kamat. Simultaneous nonlinear structural analysis and design. In *Computational Mechanics*, volume 4, pages 409–416, 1989.
- [Hol00] G.H. Holzapfel. *Nonlinear Solid Mechanics*. John Wiley & Sons, Chichester, 2000.
- [Hsi81] C.C. Hsiung. *A first course in differential geometry*. John Wiley & Sons, Chichester, 1981.
- [JM98] A. Jameson and L. Martinelli. Optimum aerodynamic design using the navier stokes equations. In *Theoretical and Computational Fluid Dynamics*, volume 10, pages 213–237, 1998.
- [Jur07] F. Jurecka. *Robust Design Optimization Based on Metamodeling Techniques*. PhD thesis, Chair of Structural Analysis, TU Munich, Report Nr. 6, 2007.
- [KC00] M.M. Kostreva and X. Chen. A superlinearly convergent method of feasible directions. In *Applied Mathematics and Computation*, volume 116, pages 231–244, 2000.
- [Kem04] R. Kemmler. *Stabilität und große Verschiebungen in der Topologie und Formoptimierung*. PhD thesis, Institut für Baustatik, Uni Stuttgart, Bericht Nr. 41, 2004.
- [Kim90] S. Kimmich. *Strukturoptimierung und Sensibilitätsanalyse mit finiten Elementen*. PhD thesis, Institut für Baustatik, Uni Stuttgart, Bericht Nr. 12, 1990.

- [Kir92] U. Kirsch. *Structural Optimization*. Kluwer Academic Publishers, 1992.
- [Kos04] F. Koschnick. *Geometrische Lockingeffekte bei finiten Elementen und ein allgemeines Konzept zu ihrer Vermeidung*. PhD thesis, Chair of Structural Analysis, TU Munich, Report Nr. 1, 2004.
- [KS79] G. Kreisselmeier and R. Steinhauser. Systematic control design by optimizing a vector performance index. In *Proceedings of IFAC Symposium on Computer Aided Design of Control Systems, Zurich, Switzerland*, pages 113–117, 1979.
- [Lei10] J. P. Leiva. Freeform optimization: A new capability to perform grid by grid shape optimization of structures. In *Proceedings of 6th China-Japan-Korea Joint Symposium on Optimization of Structural and Mechanical Systems, Kyoto, Japan*, 2010.
- [Lin99a] K. Linkwitz. About form finding of double-curved structures. In *Engineering Structures*, volume 21, pages 709–718, 1999.
- [Lin99b] K. Linkwitz. Formfinding by the 'direct approach' and pertinent strategies for the design of prestressed and hanging structures. In *International Journal of Space Structures*, volume 14, pages 73–87, 1999.
- [Lin09] J. Linhard. *Numerisch-mechanische Betrachtung des Entwurfsprozesses von Membrantragwerken*. PhD thesis, Chair of Structural Analysis, TU Munich, Report Nr. 9, 2009.
- [LO93] E. Lund and N. Olhoff. Reliable and efficient finite element based design sensitivity analysis of eigenvalues. In J. Herskovitz, editor, *Proc. Structural Optimization '93 (World Congress)*, volume 2, pages 197–204, 1993.
- [LO94] E. Lund and N. Olhoff. Shape design sensitivity analysis of eigenvalues using "exact" numerical differentiation of fe matrices. In *Structural Optimization*, volume 8, 1994.
- [Lun94] E. Lund. *FE based Design Sensitivity Analysis and Optimization*. PhD thesis, Institute of Mechanical Engineering, Aalborg University, Special Report Nr. 23, 1994.
- [Mat90] C. Mattheck. Design and growth rule for biological structures and their application in engineering. In *Fatigue Fract Eng Mater Struct* 13, volume 5, pages 535–550, 1990.

- [MB08] D. Materna and F.-J. Barthold. On variational sensitivity analysis and configurational mechanics. In *Computational Mechanics*, volume 41, pages 661–681, 2008.
- [Mic04] A. G. M. Michell. The limit of economy of material in frame structures. In *Philosophical Magazine*, volume 8, pages 589–597, 1904.
- [Mle92] H.P. Mlejnek. Accuracy of semi-analytical sensitivities and its improvement by the "natural method". In *Structural Optimization*, volume 4, pages 128–131, 1992.
- [MM98] B. Maurin and R. Motro. The surface stress density method as a form-finding tool for tensile membranes. In *Engineering Structures*, volume 20, pages 712–719, 1998.
- [Moh97] B. Mohammadi. A new shape design procedure for inviscid and viscous turbulent flows. In *International Journal for Numerical Methods in Fluids*, volume 25, pages 183–203, 1997.
- [MP05] B. Mohammadi and O. Pironneau. *Applied Shape Optimization for Fluids*. Oxford University Press, 2005.
- [ORL92] N. Olhoff, J. Rasmussen, and E. Lund. A method of exact numerical differentiation for error elimination in finite element based semi-analytical shape sensitivity analysis. In *Mechanics of Structures and Machines*, volume 21, pages 1–66, 1992.
- [OS66] F. Otto and F. K. Schleyer. *Zugbeanspruchte Konstruktionen (Volume 2)*. Ullstein Verlag, Frankfurt, Berlin, 1966.
- [OT62] F. Otto and R. Trostel. *Zugbeanspruchte Konstruktionen (Volume 1)*. Ullstein Verlag, Frankfurt, Berlin, 1962.
- [PT97] L. Piegl and W. Tiller. *The NURBS Book*. Springer-Verlag Berlin Heidelberg New York, 1997.
- [PTM77] E. Polak, R. Trahan, and D.Q. Mayne. Combined phase i-phase ii methods of feasible directions. In *Mathematical Programming*, volume 17, pages 61–73, 1977.
- [Rei94] R. Reitinger. *Stabilität und Optimierung imperfektionsempfindlicher Tragwerke*. PhD thesis, Institut für Baustatik, Uni Stuttgart, Bericht Nr. 17, 1994.

- [Rin89] U.T. Ringertz. Optimization of structures with nonlinear response. In *Engineering Optimization*, volume 14, pages 179–188, 1989.
- [Rin92] U.T. Ringertz. Numerical methods for optimization of nonlinear shell structures. In *Structural Optimization*, volume 4, pages 193–198, 1992.
- [Rin95] U.T. Ringertz. An algorithm for optimization of nonlinear shell structures. In *International Journal of Numerical Methods in Engineering*, volume 38, pages 299–314, 1995.
- [SB03] J. Schlaich and R. Bergermann. *Leicht Weit - light structures*. Prestel, 2003.
- [Sch74] H.-J. Scheck. The force density method for form finding and computation of general networks. In *Computer Methods in Applied Mechanics and Engineering*, volume 3, pages 115–134, 1974.
- [Sch95] H.P. Schwefel. *Evolution and Optimum Seeking*. John Wiley and Sons, Inc., 1995.
- [Sch05] A. Schumacher. *Optimierung mechanischer Strukturen, Grundlagen und industrielle Anwendungen*. Springer-Verlag Berlin Heidelberg, 2005.
- [SL05] J. Stegmann and E. Lund. Nonlinear topology optimization of layered shell structures. In *Structural and Multidisciplinary Optimization*, volume 29, pages 349–360, 2005.
- [SS88] H. Smaoui and L.A. Schmit. An integrated approach to synthesis of geometrically nonlinear structures. In *International Journal of Numerical Methods in Engineering*, volume 26, pages 555–570, 1988.
- [SS93] N. Stander and J.A. Snyman. A new first-order interior feasible direction method for structural optimization. In *Int. Journal for Numerical Methods in Engineering*, volume 36, pages 3937–4113, 1993.
- [Sva87] K. Svanberg. The method of moving asymptotes - a new method for structural optimization. In *International Journal for Numerical Methods in Engineering*, volume 24, pages 359–373, 1987.

- [Sva02] K. Svanberg. A class of globally convergent optimization methods based on conservative convex separable approximations. In *SIAM Journal of Optimization*, volume 12, pages 555–573, 2002.
- [Van84] G. N. Vanderplaats. *Numerical Optimization Techniques for Engineering Design*. McGraw Hill, 1984.
- [vKdB98] F. van Keulen and H. de Boer. Rigorous improvement of semi-analytical design sensitivities by exact differentiation of rigid body motions. In *International Journal for Numerical Methods in Engineering*, volume 42, pages 71–91, 1998.
- [vKHK05] F. van Keulen, R.T. Haftka, and N.H. Kim. Review of options for structural design sensitivity analysis. part 1: Linear systems. In *Computer methods in applied mechanics and engineering*, volume 194, pages 3213–3243, 2005.
- [WB05] R. Wüchner and K.U. Bletzinger. Stress-adapted numerical form-finding of prestressed surfaces by the updated reference strategy. In *Int. Journal for Numerical Methods in Engineering*, volume 64, pages 143–166, 2005.
- [Wer01] H. Werkle. *Finite Elemente in der Baustatik*. Vieweg Verlag, 2001.
- [Wüc07] R. Wüchner. *Mechanik und Numerik der Formfindung und Fluid-Struktur-Interaktion von Membrantragwerken*. PhD thesis, Chair of Structural Analysis, TU Munich, Report Nr. 7, 2007.
- [Yos80] K. Yosida. *Functional Analysis*. Springer Verlag, 1980.
- [Zou60] G. Zoutendijk. *Methods of Feasible Directions*. Elsevier, Amsterdam, 1960.
- [ZTZ00] O.C. Zienkiewicz, R.L. Taylor, and J.Z. Zhu. *The Finite Element Method, its Basis and Fundamentals*. Elsevier Butterworth-Heinemann, volume 2, edition 5, 2000.

Curriculum Vitae

Name:	Matthias Firl
Birthday:	30.05.1978
Place of birth:	Lauchhammer
Nationality:	German
Parents:	Wolfgang Firl and Heidrun Firl
08/1984 - 07/1992	"Geschwister Scholl" Elementary School in Ruhland
08/1992 - 05/1997 05/1997	"Emil Fischer" High School in Schwarzheide University-entrance diploma
11/1997 - 08/1998	Military service
09/1998 - 08/2002 08/2002	Study of civil engineering at the University of applied Sciences in Cottbus Diploma as Dipl.Ing. (FH)
09/2002 - 06/2004 06/2004	COMMAS master program at the Universität Stuttgart Master of Science, M.Sc.
12/2004 - 12/2010	Coworker of Prof. Bletzinger at the Chair of Struc- tural Analysis, Technische Universität München